2018

Experimental investigations on the aerodynamic and aeroacoustic characteristics of small UAS propellers

Zhe Ning
Iowa State University

Experimental investigations on the aerodynamic and aeroacoustic characteristics of small UAS propellers

by

Zhe Ning

A dissertation submitted to the graduate faculty

in partial fulfillment of the requirements for the degree of

DOCTOR OF PHILOSOPHY

Major: Aerospace Engineering

Program of Study Committee:
Hui Hu, Major Professor
Anupam Sharma
Peng Wei
Chris Rehmann
Baskar Ganapathysubramanian

The student author, whose presentation of the scholarship herein was approved by the program of study committee, is solely responsible for the content of this dissertation. The Graduate College will ensure this dissertation is globally accessible and will not permit alterations after a degree is conferred.

Iowa State University

Ames, Iowa

2018

TABLE OF CONTENTS

NOMENCLATURE

A	=	Propeller disc area
A_c	=	Ice accumulation parameter
b	=	Relative heat factor
BPL	=	Blade passing frequency
c	=	Chord length of the propeller
C_p	=	Specific heat of air
$C_{p,water}$	=	Specific heat of water
c_r	=	Chord length at corresponding radius of the propeller
c_{tip}	=	Chord length at the tip of the propeller
C_T	=	Thrust Coefficient
d	=	Double of the leading edge radius of airfoil
D	=	Diameter of the propeller
D_v	=	Diffusivity of water vapor
f	=	Frequency of the thrust spectrum
f	=	Frequency of the noise spectrum
h	=	Half of the serration height
h_c	=	Convective heat transfer coefficient
h_G	=	Gas-phase mass transfer coefficient

k_a = Thermal conductivity of air

K = Inertia parameter

K_0 = Modified inertia parameter

L = Separation distance

LWC = Liquid water content

MVD = Median volumetric diameter

n = Freezing fraction

N.TKE = Non-dimensional turbulent kinetic energy

N.ip TKE = Non-dimensional in plane turbulent kinetic energy

N_u = Nusselt number

p = Sound pressure

P_r = Prandtl number

p_{ref} = Sound pressure reference

p_{st} = Static pressure

p_{tot} = Total pressure

p_{ws} = Water vapor pressure at ice surface

p_{wa} = Water vapor pressure in atmosphere

r = Recovery factor

r = Non-dimensional radial distance

R = Radius of the propeller

R_{e_c} = Reynolds number at corresponding chord length

Re_{δ} = Reynolds number of water droplet

S_c = Schmidt number

SPL = Sound pressure level

St = Strouhal Number

t_f = Surface temperature

t_{st} = Environmental temperature

T = Thrust

T_{st} = Static absolute temperature

T_{tot} = Total absolute temperature

U_p = Induced velocity at different cross section

U_T = Propeller rotational speed

U_{Total} = Relative velocity

v_i = Induced velocity

V_{tip} = Tip speed

V_{∞} = Relative velocity

x = Axial coordinate

X = Axial coordinate

y = Vertical coordinate

Y = Vertical coordinate

z = Transverse coordinate

ρ = Density of air

ρ_{ice} = Density of ice

ρ_w = Density of water

Φ = Inflow angle

ϕ = Water energy transfer parameter

Θ = Twist angle at different cross section

Θ = Phase angle

θ = Air energy transfer parameter

α = Optimal angle of attack at different cross section

λ = Width of the serration

λ_h = Induced inflow ratio

δ^* = Boundary layer displacement thickness

Ω = Rotational speed of the propeller

β = Azimuthal angle

β_0 = Collection efficiency

τ = Duration of the ice accumulation process

μ = Air viscosity

Δ = Non-dimensional leading edge ice thickness

Λ_f = Latent heat of freezing water

Λ_v = Latent heat of evaporation of water

$\lambda\lambda/\lambda_{stokes}$ = Water droplet range ratio

ACKNOWLEDGMENTS

I would like to take the chance to thank my major professor, Dr. Hui Hu. Without his generous guidance, expertise, patience and funding support, I cannot finish this dissertation within three and half years. I would also like to say thank you to all my committee members, Dr. Anupam Sharma, Dr. Peng Wei, Dr. Chris Rehmann and Dr. Baskar Ganapathysubramanian for their support, comments and suggestions to my research work.

In addition, I would like to extend my appreciation to all of the members in the Advanced Flow Diagnostics and Experimental Aerodynamics Lab. It is my pleasure to work in this wonderful research group and I am very proud to be part of it. Thanks very much for the help and suggestions from Dr. Rye Waldman, Dr. Kai Zhang, Dr. Zhenyu Wang, Dr. Wenwu Zhou, Dr. Yang Liu, Dr. Morteza Khostavi, Dr. Haixing Li, Mr. Pavithra Premaratne, Mr. Linkai Li, Mr. Liqun Ma, Mr. Cem Kolbakir, Ms. Linyue Gao, Mr. Zichen Zhang, Mr. A Lusi, Mr. Haiyang Hu, Mr. Avinash Saikia, Mr. Ramsankar Veerakumar during my PhD period. My appreciation will also give to the staffs of Aerospace Engineering department, James Benson, Andrew Jordan, Christine Nelson, Carolyn Riedel, James Wellman, Jacqueline Kester and Sara Goplin

Before the end, I would like to show my grateful to my family, especially my parents, Jin Xu and Xuedian Ning. Their selfless love and encouragement support me through my life, and help me overcome all of the difficulties. I love my wife, Kuo Gai, and my daughter, Yuechen Ning (Luna). They are the most important treasures of my life. I really appreciate their love and support, and enjoy the great time we spent together.

ABSTRACT

Unmanned aerial system (UAS) is a hot topic in both industry and academia fields. As a popular planform, the rotary-wing system gains more attentions. The small UAS propeller is the most important component in this system, which transfers electric energy into kinetic energy to accomplish fly missions.

In the present work, several experimental studies have been performed to investigate the aerodynamic and aeroacoustic characteristics of small UAS propellers. First of all, by conducting force and flow filed measurements, the unsteady dynamic thrust and the wake structure of the propeller have been studied to explore the fundamental physics to help researchers and engineers to obtain a better understanding. Secondly, two kinds of bio-inspired the propellers have been designed and manufactured. Through a set of force, sound, and flow filed measurements, the aerodynamic and aeroacoustic performance of these propellers has been compared to the baseline propeller to evaluate the effects of aerodynamic efficiency and noise attenuation. It was found that the serrated trailing edge propeller could reduce the turbulent trailing edge noise up to 2 dB, and the maple seed inspired propeller could reduce the noise up to 4 dB with no effect on the aerodynamic performance. In addition, since the rotary-wing system consists more than one propeller, the rotor to rotor interaction on the aerodynamic and aeroacoustic performance also has been studied. By enlarging the separation distance between two propellers, the thrust fluctuation and noise generation could be restricted. Not only the design of the device itself has effect on the flying performance, the extreme weather also would affect it. Therefore, an icing research study on the small UAS propeller has been conducted to illustrate how does the ice formed on the propeller and how does the icing influence the aerodynamics performance and power consumption.

During these experimental studies, the force measurements were achieved by a high sensitive force and moment transducer (JR3 load cell), which had a precision of ±0.1N (± 0.25% of the full range). The sound measurements were conducted inside of the anechoic chamber located in the aerospace engineering department at Iowa State University. This chamber has a physical dimensions of 12×12×9 feet with a cut-off frequency of 100 Hz. The detailed flow structure downstream of the propeller was measured by a high-resolution digital PIV system. The PIV system was used to elucidate the streamwise flow structure downstream of the propeller. Both “free-run” and “phase-locked” PIV measurements were conducted to achieve the ensemble-average flow structure and detailed flow structure at certain phase angles.

CHAPTER 1

GENERAL INTRODUCTION

1.1 Background and motivation

Nowadays, the unmanned aerial system (UAS), also known as drone, becomes a hot topic in both industry and academia fields due to the low-cost and the development of the small electronics, such processors, sensors, and batteries[1]. According to BI intelligence in 2016, the total shipments of the small UAS will reach to 29 millions in 2021[2]. The rapid development speed is mainly due to the advantages of the small UAS. First of all, these types of systems do not require pilot to control them on board. Thus, the size of the UAS can be designed very small. The smaller size will allow them to fly into narrow region and enter environments that are dangerous to human life. Secondly, the small UAS could accomplish fly missions under the control from ground control stations (GCS) or autonomous flight. Normally, the small UAS can be classified into three categories: rotary-wing aerial system, flapping wing aerial vehicle, and fixed wing aircraft. Among these three configurations, because of the good hovering ability and vertical take-off and landing motion, the rotary-wing system gained more attentions from researchers and engineers. Also, due to the unique flight strategies, many companies, like DJI, 3DR, Amazon, and Alibaba Group were involved into this business, which broaden the application of the rotary-wing serial system to many civilian fields. DJI win the video taking market due to their stabilized camera, which could compensate the vibration generated from the small UAS propeller and frame. Therefore, the video obtained from their devices are very smooth and stable. Amazon and Alibaba Group paid attention to

the small UAS delivery function. On December 7th, 2016, amazon prime air started its first publicly delivery at Cambridge, England. On October 31st, 2017, Alibaba Group used a group of UAS achieve cross-sea delivery. The UAS took about 10 minutes to cross 5km sea under around 12m/s wind. At TU Delft, Alec Momont designed and manufactured an ambulance drone, which had an Automated Defibrillator (AED) embed in it. With this UAS, the survival rate of cardiac arrest could be effectively increased. More than these, small UAS has also been used to monitor the crops[3,4], as well as building constructions. Lindsey used teams of quadcopters to construct building[5]. Mirjan used a group of quadcopters to build a bridge[6].

Commonly, the rotary-wing aerial system consists even number of propellers (e.g., 4, 6, 8, or even more) and designed into two sets in either clockwise or counter-clockwise rotation. With such configuration, the aerodynamic torque and angular acceleration about yaw axis are zero. The pitch, roll, and yaw motions of the rotary-wing system are controlled by varying rotational speed of propeller at different position. The first manned rotary-wing system with four propellers was built in 1907, called Cornu helicopter[7]. However, due to the poor engine and control method, Cornu helicopter cannot leave ground. Recently, the rapid development speed of the control theory extremely benefits the development of the small unmanned aerial system with rotary-wing. By studying and applying different control methods, such as, PID, back-stepping, LQR, and nonlinear controllers to the small UAS, researchers could make the small UAS fly stably, such as, hover at a stabilized location, response to the command in a short and stable way, and follow the path in an accurate fly motion[8–11]. In addition to stabilize control, other

researchers focus their eyes on the trajectory tracking control to allow the small UAS fly autonomous[12,13].

Although the rotary-wing aerial system could fly stably to accomplish many tasks, it still faces problems, such as short duration time, noise emission and extreme weather impact. Normally, the duration time of this type system is about half an hour, which is not enough for many applications. For example, image taking, delivery, and inspection. In order to extend the flight time of the small UAS, researchers and engineers need to improve the aerodynamic performance. This requires a deep understanding about the flying dynamics and detailed flow field structure around the device. The noise generated from the small UAS is another essential problem associated with this system. For instant, the DJI Phantom series drone could generate noise up to 80 dB by itself, which almost touches the boundary of the hearing safety limitation (85dB). After the noise reach this limitation, surrounding people need to wear earphone to protect their hearing. As we all known, the small UAS always fly around the human and sometimes several devices will fly together to finish a task. Thus, the noise generated from small UAS will impact human directly. Not only human, wild animals will also be affected by the noise emitted from the small UAS. Ditmer conducted a study to explore how does the noise generated from the small UAS affect the behaviors of bears[14]. Through this work, author found that the noise generated from the UAS will raise the heart rates which means the noise will make bears stressful. At the same time, because of the noise of the drone will affect the nesting bird (peregrine falcon), Puget Sound Energy restrict the use of the small UAS in the Snoqualmie Falls Hydroelectric Project and Park. Therefore, the noise reduction is another essential challenge for the small UAS designer and researcher. The third problem

that the small UAS faces is the extreme weather impact, such as, icing, rain, and wind. The small UAS operated outside is a well-known working condition, different weather will have significant effect on the flight performance from cut down the aerodynamic efficiency to damage the system. A good understanding of the weather impact will help people solve this problem and achieve safe operation.

Previously, Hoffmann studied the flight dynamics and the control of a quadcopter through theoretical and experimental methods. By adding the consideration of the flight dynamics (total thrust, blade flapping and airflow disruption) into the control method (PID control), the effect and issues related to the aerodynamic effects on the flight performance has been explored. The author addressed the importance of the accurate models of the complex aerodynamics on the development of the control theory[15]. Huang also mentioned the importance of the aerodynamics on the aggressive maneuvering control[12]. In addition to the aerodynamics effect on the control, several computational studies had been found in literature to explore the potential of CFD on the small UAS aerodynamic analysis. Lopez used Spalart-Allmaras and k-ω turbulence models to simulate the flow around the propeller at hover motion. Although both models could predict the wake and the thrust and moment coefficients, the accuracy was not very good. The predicted thrust and moment coefficients was about 20% larger than the real measurements[16]. Similar results were also reported by Liu in the CFD study, in which, the flow field simulation and the aerodynamic performance prediction were obtained from the unsteady Reynolds averaged Navier-Stokes equation (URANS). By using URANS, the prediction at high Reynolds number ($\sim 10^6$) matched with the experimental results very well. However, that Re is not the typical value for small UAS. The small

UAS always operates at Re around 10^5. At this Re range, they also over predicted the thrust and moment coefficient[17]. That means the CFD simulation had limitation to accurate predict the mean thrust and moment coefficient. Therefore, a deeply understanding of the flow field downstream of the propeller through experimental method is necessary, which will help CFD researchers to modify their methods and increase the accuracy. In addition to the computational scheme studies on the thrust and moment coefficient prediction, a slipstream model with the consideration of the diffusion effect has also been studied to explore the wake structure of the propeller[18]. Meanwhile, Yoon from NASA use the Reynolds-averaged Navier-stokes (RANS) equation to studied the flow interaction between the rotors. They found that with the reduced separation distance between rotors the thrust coefficient will decreases[19]. Although the CFD tools could help us understand the problems, additional experimental studies are needed to validate the CFD results and dig into the fundamental of the physics of the flow around the small UAS propeller.

Intaratep conducted experiment to study the effect of the multi-rotor on the thrust and noise generation. He found that, as the propeller number increase from 1 to 4, the thrust generated from the propeller is not scale up by a factor of propeller number, which indicate a flow interaction effect on the aerodynamic performance when several propeller works together. Also, the noise level increase as the propeller number increase was also observed[20]. The noise generated from the small UAS consist of the mechanical noise and aerodynamics noise, or known as aeroacoustics. Compared with aerodynamic noise the mechanical noise due to the vibration can be neglected. The aerodynamics noise consists of inflow turbulence noise and airfoil self-noise. Between these two sources the airfoil

self-noise dominant the total noise level for small UAS propeller, which can be classified into five categories: turbulent boundary layer trailing edge noise, separation/stall noise, trailing edge bluntness-vortex shedding noise, laminar boundary layer vortex shedding noise and tip vortex formation noise[21]. [Kurtz] The noise reduction from propeller, helicopter rotor, aircraft wing, even for wind turbine blade has been well studies before. Several noise reduction method has been investigated. For example, owl wing inspired saw-tooth serrated trailing edge could effectively reduce the turbulent boundary layer trailing edge noise as well as vortex shedding noise, which has been studied theoretically and experimentally at large Reynold number ($>10^5$)[22–26]. The modification of the tip (tip sweep) could reduce the noise, which has been widely used in helicopter blade. The tip speed of the helicopter is very fast, closed to the sound speed. The thickness noise generated at there is proportional to the velocity normal to the edge, which can be reduced by sweep the tip[21]. In addition, the blade planform modification is another method to reduce the noise. By add a leading edge boundary layer trip, Leslie could reduce the broadband noise by eliminate the laminar separation bubble[27].

Besides the aerodynamics and aeroacoustics of the small UAS itself, the weather also has impact on the aerodynamic performance. The extreme weather, such as, icing, rain and wind will affect the flight performance by reducing the operating time even cause safety issue. Those are the issues that drone companies and FAA cares about. A study on the weather impact will broaden the understand and provide suggestions to manufacture to guide them design efficient and stable small UAS. Also, the weather impact study could benefit the flight regulation development.

With a clear idea about the problems associated with the small UAS and considering the propeller as the main component generated aerodynamic thrust and aerodynamic noise, we focus our study on the small UAS propellers to explore the deep understanding and improve the aerodynamics and aeroacoustic performance. A series experimental investigations had been conducted from wake structure measurement, novel bio-inspired propeller design to rotor to rotor interaction, even for icing impact on small UAS propeller.

1.2 Outline of thesis

This dissertation contains 7 chapters. Chapter 1 is the general introduction, which provided background information related to the development of the small UAS, and detailed address the three major issues associated with it and the literature review. Chapter 7 is the overall summary and conclusion for this dissertation. From Chapter 2 to 6, 5 topics related to the small UAS propeller were investigated experimentally from force measurement, sound measurement, to flow flied measurement. Chapter 2 studied the unsteady thrust and wake characteristic of the small UAS propeller at hover motion. The means thrust and thrust perturbation were analyzed, the detailed flow structure was also obtained from PIV measurements. Chapter 3 and Chapter 4 investigated two types of bio-inspired propellers with a focus on the noise reduction. The saw-tooth serrated trailing edge propellers (SSTP) was studied in Chapter 3, the thrust, noise level and flow structure of SSTP with different width height ratio were compared to baseline propeller. Chapter 4 studied the maple seed inspired propeller. By modifying the planform, the novel designed propeller could reduce the noise with no effect on the aerodynamic

performance compared to the baseline propeller. The rotor to rotor interaction was illustrated in Chapter 5. The effect on the thrust generation, noise emission, and flow structure due to the difference in the separation distance between two counter-rotating has been detailed addressed. In Chapter 6, I studied the weather impact on the small UAS propeller with a focus on the icing impact. The ice formation process at different temperature and liquid water content (LWC), and the icing effect on the lift generation and power consumption were experimentally explored.

CHAPTER 2

AN EXPERIMENTAL STUDY ON THE AERODYNAMIC THRUST AND WAKE CHARACTERISTICS OF SMALL UAS PROPELLER

Zhe Ning and Hui Hu

Department of Aerospace Engineering, Iowa State University, Ames, Iowa, 50011

Abstract

The unsteady aerodynamic thrust and wake flow characteristics were studied experimentally. The mean thrust and thrust fluctuation of the propeller were investigated by accurate force measurements using a high-sensitive force transducer. The FFT analysis of the time series thrust results revealed that the thrust perturbation increases as the gain of the rotational speed is mainly associated with the two-blade configuration. The ensemble-average flow quantities such as mean velocity and vorticity were determined from "free-run" PIV measurements. Furthermore, the evolution of the tip vortices and vortex sheet structure at different downstream location were explored by "phase-locked" PIV measurements. By tracking the location of these vortices, the travelling speed and slipstream flow boundary can be obtained. Finally, the dynamics process of the evolution of the tip vortices interaction were elucidated based on the detailed flow structure measurements.

2.1 Introduction

The rapid development speed of the small Unmanned Aerial System (UAS) was benefited from the low-cost electronic devices[1]. Specifically, because of the good hovering ability and vertical take-off and landing (VTOL) motion, the rotary-wing system became a popular configuration and gained more attention from industry, academia and government agencies. With the unique strategies, the rotary-wing UAS has been used to accomplished tasks from image taking, package delivery, building construction, to rescue operation, disease control and crop monitoring.

Normally, the rotary-wing UAS contains even number propellers, such quadcopters, hexacopters, and octocopters. In order to let the small UAS fly stably, previous researchers and engineers paid more attention to the control aspect. By studying and applying different control methods, such as, PID, back-stepping, LQR, and nonlinear controllers to the small UAS, researchers could make them fly stably and also achieve aggressive maneuver and attitude changes[2–5]. The importance of the aerodynamics on control of the rotary-wing UAS has been study by Hoffmann and Huang[6,7]. By considering the total thrust, blade flapping and airflow disruption into their dynamic model, the quadcopter could fly stably and achieve aggressive maneuver. So far, although the rotary-wing UAS could fly stably to accomplish many tasks under well-developed control theories, how to make them fly efficiently is still an essential challenge to this society. Currently, the duration time of these systems is around half an hour, which is not enough for many applications such as delivery and monitoring.

A sound understanding of the unsteady dynamic loading on the propeller and the wake flow characteristics would greatly help the optimization of the small UAS. Recently, several researchers started to look into the propeller performance, however, the available

sources and experimental data of small UAS propeller were less. Brandt and Merchant conducted wind tunnel and static test to collect mean force data, such as, thrust and moment coefficients and propeller efficiency[8,9]. With the purpose of generating high-quality data set to validate the software tools, Russel et al. collected force measurement data from 5 different commercial small UASs available in market to study the propeller performance[10]. Besides the mean thrust, large thrust fluctuation has been reported by Russel at one rotational speed. More detailed thrust fluctuation results and analysis at different rotational speed was needed to understand the unsteady loading on the propeller, thereby benefit the elimination of undesired vibration. In addition to the propeller performance measurements on force and moment, computational method was used to study the wake of the small UAS to predict the aerodynamic performance. Perez G studied the flow around the quadcopter using multiple reference frame method with Spalart-Allmaras and k-ω turbulence models[11]. The predict results showed a good trend with the experimental data, however, the magnitude is about 20% overestimated. Liu used the unsteady Reynolds averaged Navier-Stokes equation to predict the thrust and power coefficient[12]. The thrust and power coefficient agreed well with the experimental results at the chord Reynolds number over 1 million, but the over predict appeared at low Reynolds number (30,000~50,000). However, the chord Reynolds number range from 30,000 to 50,000 are typical values for the many existing small UASs (e.g., DJI Phantom series). This indicates the CFD simulation had limitation to accurate predict the mean thrust and moment coefficient. Therefore, a deeply understanding of the flow field downstream of the propeller through experimental method is necessary, which will help researchers to modify and validate their CFD methods. From experimental perspective, Ning conducted force, sound and PIV measurements during the comparison studies between novel

bio-inspired propeller and baseline propeller[13,14]. Several flow features downstream of the propeller was explored. However, detailed flow structure and thrust analysis were missed. Furthermore, Zhou also conducted experimental study to explore the effect on the aerodynamic and aeroacoustics performance of small UAS propeller due to the rotor to rotor interaction with different separation distances[15]. The flow filed information obtained in this research work was used to explain the rotor to rotor interaction effect. Many detailed flow phenomena were not emphasized.

In the current study, an experimental investigation was conducted to explore the unsteady thrust and wake flow characteristics of a small UAS propeller at hover motion. The experiments were conducted at Advanced Flow Diagnostics and Experimental Aerodynamics Laboratory at Iowa State University. The aerodynamic thrust was measured by a high-sensitive force and moment transducer. In addition, the high resolution PIV system was used to conduct "free-run" and "phase-locked" measurements to obtain the ensemble average and phase average results of the wake structure. The analysis of the thrust results and detailed flow structure information would explore the underlying physics and quantify the unsteady vortex flow behavior in the propeller wake. As a result, this research work would benefit the optimization of the propeller design, and provide detailed aerodynamic force and flow filed information for the CFD validation.

2.2 Propeller models design and experimental setup

2.2.1 Propeller design

In the current study, an E63 airfoil (low Reynolds number airfoil) was used to design the propeller in order to generate 3N designed thrust[16]. Due to the strength concerns the

thickness of the airfoil was doubled along the camber line. The propeller had a diameter of 240mm and tip chord of 11mm. The chord lengths along the propeller radius from tip to 30% radius were calculated by the optimal chord length equation $C_r = \frac{c_{tip}}{r}$, where C_r is the chord length at the corresponding radius location, and r represents a non-dimensional radial distance, which is 0 at the rotating center and 1 at the tip[17]. This kind of design will keep the solidity to be 0.12, which is widely used for the propeller of a small unmanned aerial system. As shown in Fig. 1, the twist angle at each cross section is designed to be the sum of inflow angle φ and the optimal angle of attack α. The propeller twists 11.6° at the tip and 26.3° at the 30% radius from the center. The propeller was manufactured by a high-accuracy 3-D printing machine with a layer by layer resolution of 20 microns. The materials of the propellers were hard plastic (VeroWhite).

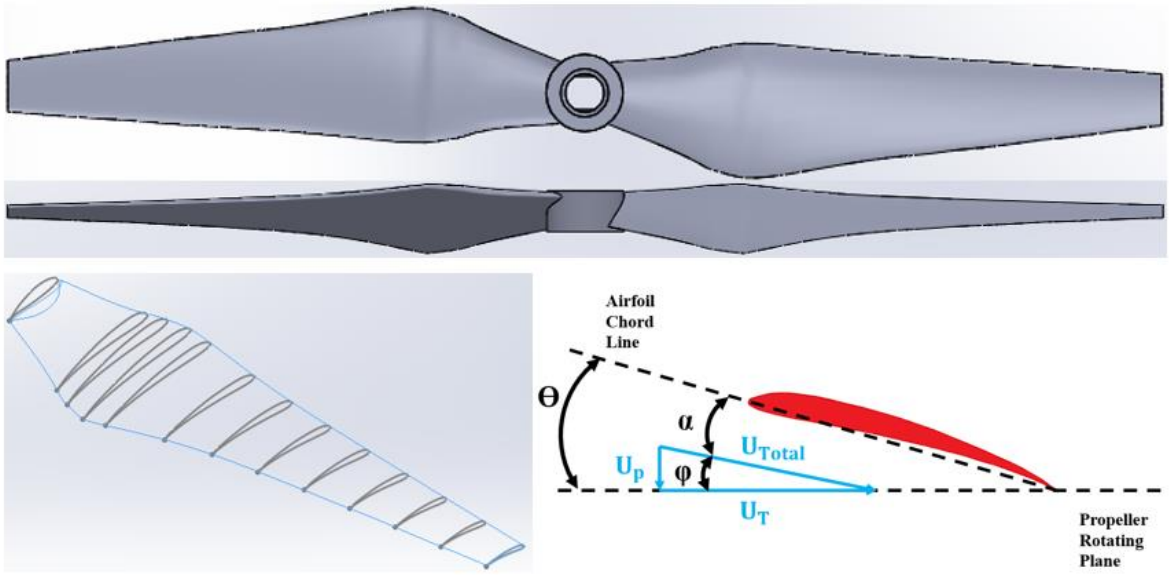

Fig.1 Design of the propeller

2.2.2 Experimental setup for the measurements

The experiment was conducted in the Advanced Flow Diagnostic and Experimental Aerodynamic Laboratory at Iowa State University. The propeller was driven by a brushless motor (i.e., dji 2212) with the power from a direct current power supply. The voltage of the power supply was kept at 11.1 V for all the measurements. The rotational speeds of the propellers ranged from 0 to 100 RPS, which was controlled by the signal from a function generator via an electronic speed controller. During the measurement, a tachometer was used to detect the pre-marked blade to quantify the rotational speed. Meanwhile, a pulse signal was generated, which was used to control the laser system and the camera to achieve the "phase-locked" PIV measurement. It should be mentioned that a 0.2D clearance gap was maintained to reduce the flow interaction between the support rod and propeller. This value is a typical separation distance between propeller and frame for small UASs. Fig. 2 represents the experimental setup, which was used to measure the aerodynamic thrust and the detailed flow structure in the downstream of the propeller. The aerodynamic thrust was measured by a high-sensitivity force-moment sensor (JR3 load cell), which had a precision of ±0.1N (± 0.25% of the full range). The detailed flow structure downstream of the propeller was measured by a high-resolution digital PIV system. Both "free-run" and "phase-locked" PIV measurements were conducted to achieve the ensemble-average flow structure and detailed flow structure at certain phase angles. For the "free-run" measurement, 1000 frames of instantaneous PIV measurement results were used to generate the ensemble-average results. The "phase-locked" PIV measurements were conducted at 12 different phase angles ranging from 0° to 330° with 30° increments. Each of the phase-average result was calculated from 255 frames of instantaneous measurements. During the PIV measurement, about 1μm

water-based droplets were generated by the fog machine (i.e., ROSCO 1900), which seeded the whole flow field as the tracer particles. The field illumination was provided by a double-pulsed Nd:YAG laser generator (Quantel Evergreen 200) with the maximum power of 200mJ per pulse at a wavelength of 532nm. Through a set of optics, the laser beam was formed into a thin laser sheet with an approximate thickness of 1mm at the test section. For the PIV measurement, the laser sheet was perpendicular to the propeller rotating plane, and cut through the mid-section of the rotor disc. A high-resolution (2048×2048 pixels) charge-coupled device (CCD) camera with an axis perpendicular to the laser sheet was used to capture the raw images of the local flow. In order to cooperate the laser illumination and the image taking, the camera and the laser generator were connected to a computer via a digital delay generator to control the timing. A second digital delay generator was used to add a delay time to the signal, generated from the tachometer, to acquire "phase-locked" PIV measurements at different phase angles.

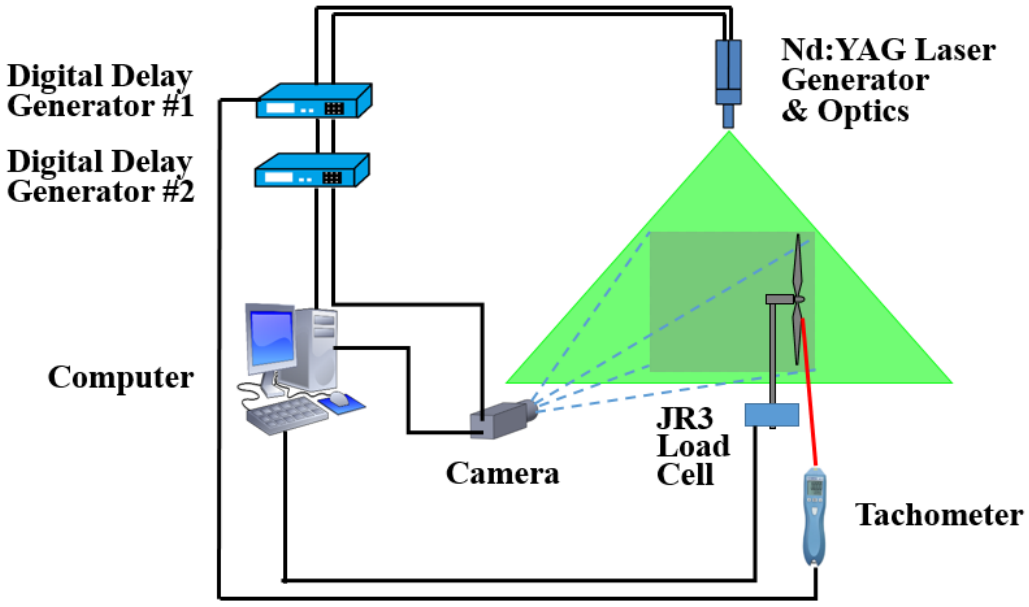

Fig. 2 Experimental setup for thrust and PIV measurements

2.3 Measurement results and discussions

2.3.1 Aerodynamics thrust measurement results

The propeller thrust was measured at different rotational speed ranging from 0 to 100 RPS. Fig. 3 (a) illustrates the mean aerodynamic thrust and thrust coefficient as a function of propeller rotating speed. In the plot, the mean aerodynamic thrust represented by the square symbol and the triangular symbol denotes the thrust coefficient. Each symbol represents a 30 seconds measurement with 1000 samples per second. It could be easily revealed that, with the increase of the rotational speed, the aerodynamics thrust generated from the propeller show a quadratic trend. According to the momentum theory, the thrust generated from a propeller is proportional to the square of the induced velocity. In eq.1, the thrust denoted by T, and the v_i represents the induced velocity. As shown in eq.2, the induced velocity has a linear relationship with the tip speed of the propeller, where λ_h is known as the induced inflow ratio in hover. Therefore, the quadratic trend in the means thrust plot should be expected.

$$T = (\rho A v_i)2v_i \quad \textbf{(1)}$$

$$v_i = \lambda_h V_{tip} \quad \textbf{(2)}$$

The thrust coefficient was calculated by the eq.3. It can be found that, the mean thrust coefficient raised as the rotational speed gain from 20 to 50 RPS. When the rotational speed keep increasing, the mean thrust coefficient varied slightly, almost stayed at a constant value. The similar trends were also reported by Russell from NASA[10].

$$C_T = \frac{T}{\rho A V_{tip}^2} \quad \textbf{(3)}$$

Beside the mean thrust, the time series thrust results also have been studied. Fig. 3 (b) illustrated the time series thrust measurement results at three different rotational speeds (56.4, 74.7, and 90.1 RPS). The dashed lines indicate the mean thrust for different cases. As the rotational speed increases, the rise of the mean thrust can be easily identified. Meanwhile, the thrust fluctuation became more serious when the rotational speed raised up. As shown in Fig. 3 (c), the standard deviation of the thrust increased from about 0.2 to 0.36 while the rotational speed gained from 50 to 90 RPS. This kind of thrust fluctuation is mainly due to the propeller configuration. First of all, although the difference is very small, the two blades cannot not be exact same due to manufacture consideration. As a result, the unbalance on both sides of the propeller would lead to large perturbation when propeller rotates fast. Secondly, since most of propellers for small UAS were manufacture by bard plastic, where the stiffness was low, the propeller deformed when force applied on it. Considering the force distribution on the propeller along the blade, large portion of thrust was generated at the tip part of the blade. Therefore, the blade tip will bend to positive thrust direction. With this geometry variation, the propeller suffered large force perturbation when the rotational speed increase because the flexibility of the propeller played an important role on determine the aerodynamic performance[18].

In addition to the mean thrust and thrust fluctuation, a spectrum analysis has also been applied to the measurement data at rotational speed of 56.4, 74.7, and 90.1 RPS by using Fast Fourier Transform (FFT). The data used to perform the spectrum analysis are the time serious thrust results after subtracting the mean thrust. Therefore, the large amplitude was not located at 0 Hz. In Fig. 4 (a), a clear peak signal (f) can be easily distinguished from other signals, which corresponds to the propeller rotational speed. This kind of spectrum

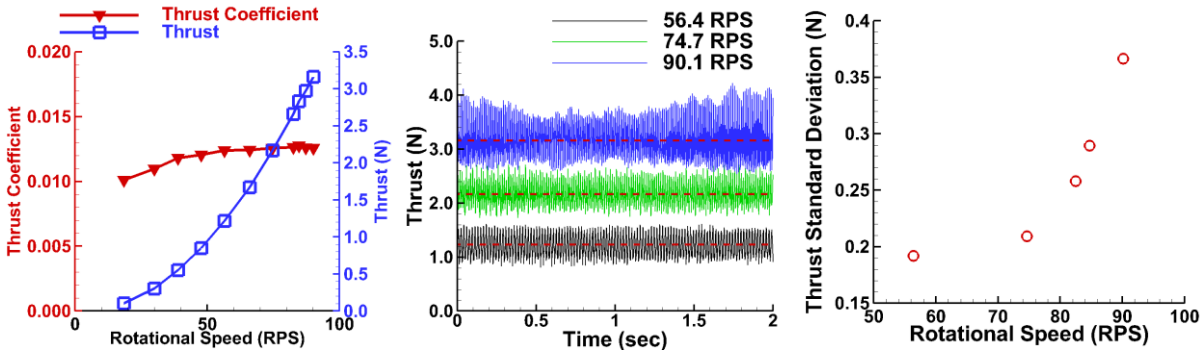

(a) mean thurst and Thrust coefficient (b) Time series thrust (c) thrust standard deviation

Fig. 3 Time series thrust and thrust standard deviation

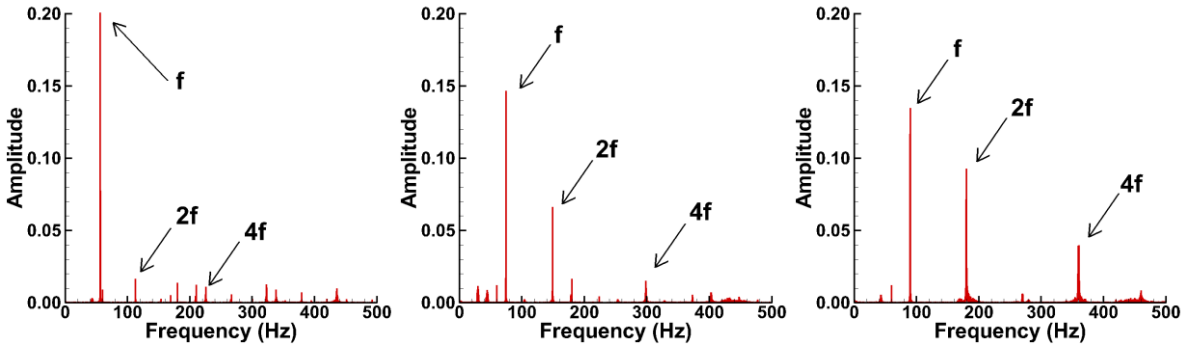

(a) Ω = 56.4RPS (b) Ω = 74.7RPS (c) Ω = 90.1RPS

Fig. 4 Spectrum of measured thrust at different rotational speeds

results have been reported by Yang and Verbeke [19,20]. When the rotational speed increase to 74.7RPS, the second harmonic signal (2f) became obvious, shown in Fig. 4 (b), where the frequency is the blade passing frequency (BPF). It means the thrust fluctuation at BPF become significant. At the same time, the amplitude of the signal (f) reduced. As the rotational speed keep increase to 90.1RPS, the fourth harmonic signal (4f) became distinguishable, which can be found in Fig. 4 (c). Meanwhile, the amplitude of the signal (f) reduced slightly, and the amplitude of the signal (2f) increase dramatically. These two signals (2f and 4f) are the first and second harmonics of the BPF. This trend means that the thrust perturbation at BPF and its harmonic frequency become serious as the rotational speed

increase. This is another evidence to prove that the increased thrust fluctuation at high rotational speed is associated with the two blades configuration of the propeller.

2.3.2 Flow field measurement results at hover motion

As mentioned before, a high-resolution PIV system was used to investigate the detailed flow structure in the downstream of the propeller at hover flight condition. The typical “free-run” PIV measurement results of the propeller wake was shown in Fig.5. The term “free-run” indicates that the image taking frequency is not the harmonic of the propeller rotational frequency. Fig. 5 (a) shows the instantaneous vorticity result of the flow around and downstream of the propeller. The tip vortex structures (dark blue circle) could be clearly revealed in the downstream of the propeller in a queue. A large positive vorticity region was found around the motor, which is mainly due to the flow passing the blunt body. In addition, the vorticity fluctuations in the downstream of the propeller has also been explored. The ensemble-average velocity result was represented in Fig. 5 (b), where three typical flow regions can be identified. The region above the propeller known as the inflow region. Due to the propeller rotation, the flow was sucked into the rotating plane and pushed downward. The large blue region denoted the quiescent flow region, where the magnitude of the flow velocity was small (<2m/s). The region below the propeller was called the induced flow region. In this region, the flow velocity was higher than the other two regions. Because of the low pressure at the high velocity region, the flow shrunk inward in the downstream. Fig. 5 (c) represents the ensemble-averaged vorticity results. Instead of clear tip vortex structures, the tip vortices region and the vortices after the motor are very obvious. The dissapation rate of these two types of vortices were high. Due to the dissipation, the size increase in the tip vortices region can be clearly obseved.

The induced velocity components perpendicular to the rotating plane at several downstream cross sections were revealed in Fig. 6 (a) and the magnitude of velocities were shown in Fig. 6 (b). The main stream flowed from top to bottom. The high velocity magnitude region was found in the induced flow region. The velocity difference between the upper side and lower side of the propeller indicates the pressure difference, which is the reason for the thrust generation. Close to the tip of the blade, there is a revese flow region (blue color region), which is because of the tip vortex formation. It could be found that as the induced flow traveled downstrem, the nominal slipstream boundary will shrunk inward first due to the acceleration of the induced flow, and expand due to the diffusion. In addtion, the highest velocity magnitude appeared close to the tip at beginning, and moved inward as the flow traveled downstream. The highest velocity magnitude increased from about 8m/s at 0.1 R to about 11m/s at 1.6 R downstream, as shown in Fig. 6 (b). Due to the blunt body effect of the motor, the velocity was about 0 after motor and increased as the flow travel downward.

In addtion to the “free-run” PIV measurements, “phase-locked” PIV measurements were also conducted at hover flight condition to obtain the detailed flow structure in the downstream in order to gain better understand about the propeller wake characteristics. In the current study, the wake structure downstream of the propeller was measured at 12 different phase angles range from 0° to 330° with 30° increments. Fig. 7 represents the velocity distributions of the propeller from phase angle 0° to 300° with 60° increments. The 0° phase angle means the rotating propeller is cutting through the measurement plane. Same as the “free-run” PIV measurement results, three typical flow regions were also obseved in the “phase-locked” PIV measurment results. One phenomenon was not captured by the “free-run” PIV measurement was the periodic velocity deficit located at the slipstrem boundary

between the induced flow region and quiescent region. This is mainly because of the blade tip cutting the flow, which results in the formation of the tip vortex. Within the induced flow region, there were several “strip shape” low speed regions, denoted by the pink color circle in Fig. 7 (a). This is mainly because of the the propeller blade cut into the measurement plane, which leads to this periodic velocity change. Between two low speed regions, the induced velocity magnitude increased first and reached to a maximum value then reduced along the streamwise. These two kinds of flow features could be also revealed in other phase angles. With the phase angle increase, these two flow structures moved downstream.

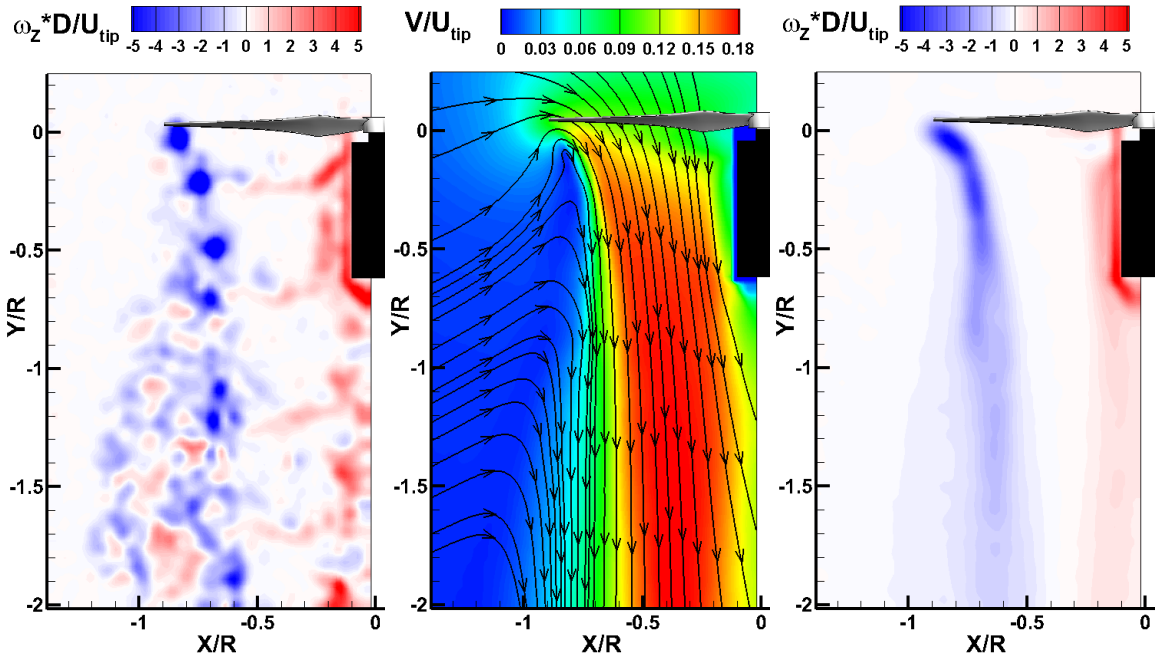

(a) Instantaneous vorticity (b) averaged velocity (c) averaged vorticity

Fig. 5 “Free-run” PIV measurement results of the propeller at hover motion

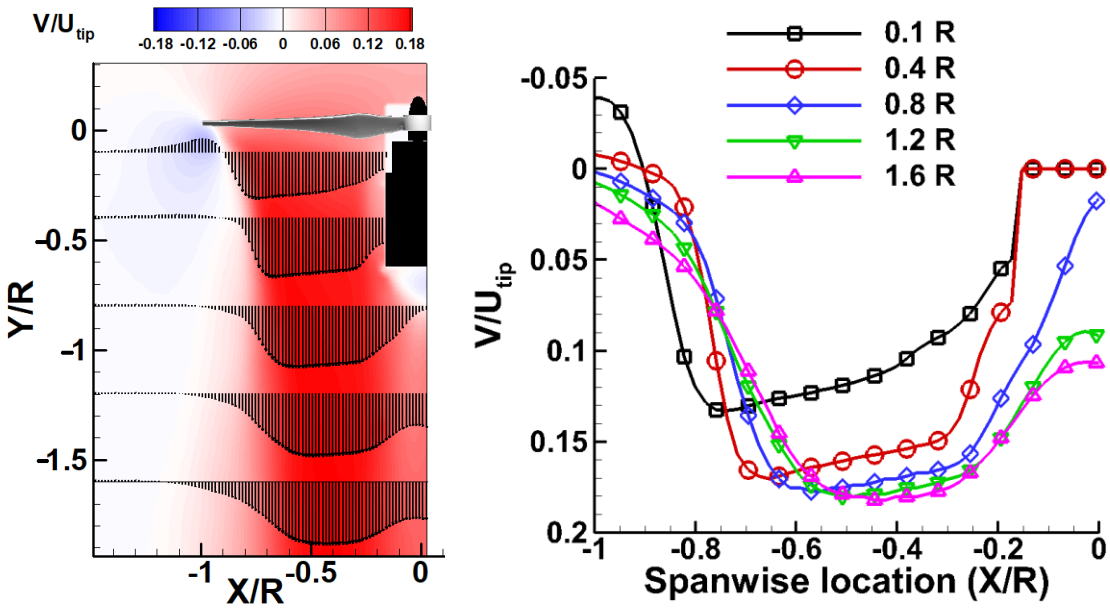

(a) Velocity component (b) Velocity distribution

Fig. 6 Velocity component perpendicular to the rotating plane and the velocity distributions at different down stream locations

The vorticity distribution results of the "Phase-locked" PIV measurement were explored in Fig. 8. The tip vortex, a typical flow structure in the wake of finite wing, was generated at the tip of the propeller due to the pressure difference between pressure side and suction side. As the phase angle increased from 0° to 300°, the tip vortex structure traveled downstream and shrunk inwards. This is due to the induced velocity, which was low at the tip and high in the middle. This velocity difference resulted in a low-pressure region in the middle section. Besides the tip vortices, both positive and negative vorticity regions, also known as vortex sheet, generated by the flow passing the trailing edge of the propeller can be viewed in all plots. The vortex sheet was associated with the "strip shape" low speed region mentioned in the velocity results section. The strength of these vortices was smaller compared to the tip vortices. Because of the velocity gradient was small going from the tip to the center, this pair of vortices were almost parallel to the rotating plane. In order to better understand the flow

structures, the indexes were used to illustrate the sequence. The red color and black color indexes denotes the tip vortex and the vortex sheet, respectively. The indexes “A” and “B” indicates the vortices generated from the blade-1 (shown in Fig. 8 (a), (b), and (c)) and blade-2 (shown in Fig 8 (d), (e), and (f)), respectively. The index “1” means the vortices generated from current cycle, and indexes “2” and “3” means the vortices generated from previous cycles. Since the tip vortex and vortex sheet of the same blade at the same cycle were generated at the same time, the vortex sheet traveled faster than the tip vortex can be explore from plot because it located at further downstream than the tip vortex at the same wake age. For example, in fig. 8 (c), the vortex sheet A-1 traveled to 0.3R downstream and the tip vortex A-1 only moved about 0.1R. Fig. 9 (a) shows the location of these two types of vortices as a function of wake age. This was obtained by the tracking the center location of the tip vortex and location of the vortex sheet from blade-1. It can be found that the traveling speed of the vortex sheet was more than doubled compared to the tip vortex. By tracking the center location of the tip vortex, the slipstream boundary of the propeller wake could be determined, as shown in Fig. 9 (b). The threshold plane was located at about 0.7R downstream of the propeller, which was the boundary of the near-field region and far-field region. At the near filed region, the acceleration dominated the flow more than diffusion. At the threshold plane the propeller wake had the smallest diameter about 0.7R, which agree with the momentum theory, that the induced flow velocity at threshold plane was doubled of the one at rotating plane since the mass flow rate was almost constant[17].

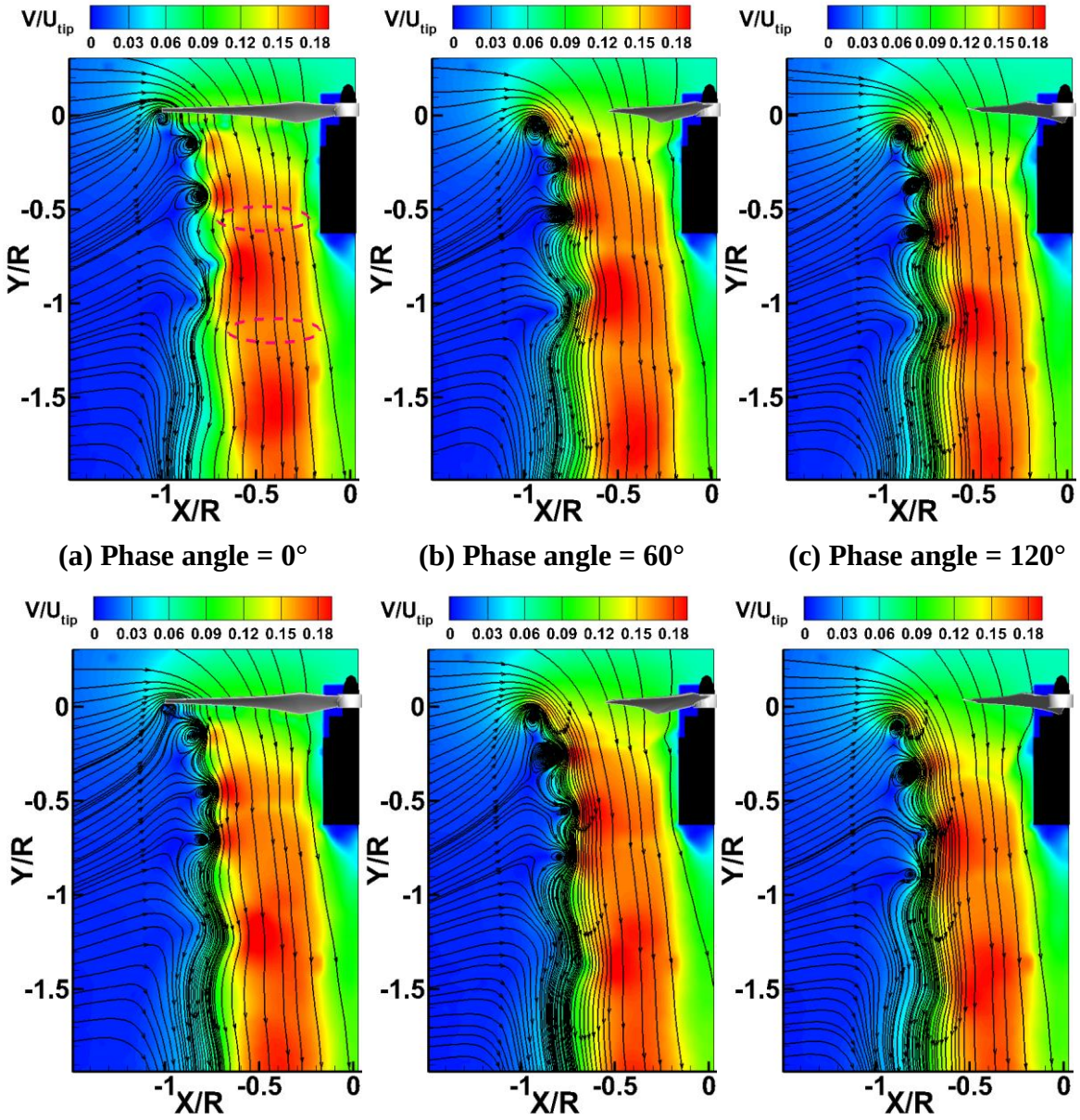

(a) Phase angle = 0° **(b) Phase angle = 60°** **(c) Phase angle = 120°**

(d) Phase angle = 180° **(e) Phase angle = 240°** **(f) Phase angle = 300°**

Fig. 7 Velocity distributions of the "Phase-locked" PIV measurement results at different phase angle

Another interesting phenomenon observed was the tip vortices interaction. As shown in Fig. 8, the tip vortex and vortex sheet travelled downstream with different speed. As a result, the vortex sheet will interact with the tip vortex generated from another blade at the previous cycles. For example, in Fig. 8 (b), the vortex sheet A-1 started to interact with tip

vortex B-2. This flow phenomenon was also reported by Leishman through digitizing the displacement of the vortex sheet from flow visualization[17]. However, he did not mention the roll-up motion of the tip vortices interaction since he only showed the results from phase angle 0° to 160° in the near-filed region. Within this wake-age period, the strength of the tip vortex was strong, the separation distance between the cores of the two tip vortices was relatively large. The influence of the tip vortices on each other was wake. We continuously measured the wake structure from 180° to 300° at the far-field region, the roll-up motion of the tip vortices interaction was obtained. After the threshold plane, the upcoming tip vortex started to interact with the previous one due to the velocity changes caused by diffusion and the interaction between the vortex sheet and tip vortex. Fig. 10 clearly reveals the evolution of the tip vortices interaction, which was obtained by tracking the vortex pair A-3 and B-3 from Fig. 8. As mentioned in velocity section, the vortex sheet region has low velocity and the velocity magnitude is high between two vortex sheets. These flow structure resulted of the periodic varies in the pressure within the induced flow region. Due to the travelling speed difference between induced flow and slipstream flow boundary, the periodic pressure variation caused the X-direction velocity component at the flow boundary to change directions. Therefore, in Fig. 10 (a), the velocity vector had positive X-direction component at location of tip vortex B-3, and negative X-direction component at location of tip vortex A-3. This caused the clock-wise roll-up motion start. As the phase angle increased to 60°, shown in Fig. 10 (b), the vortex B-3 moved towards the main stream, and the vortex A-3 moved outward of the main stream. Due to the Y-direction velocity of vortex B-3 is higher than the one of vortex A-3, the Y-direction distance between this vortex pair became short.

Because of the X-direction velocity component still kept negative sign, the roll-up angle kept increasing. At the phase angle equal to 120°, the vortex pair kept rolling due to the velocity

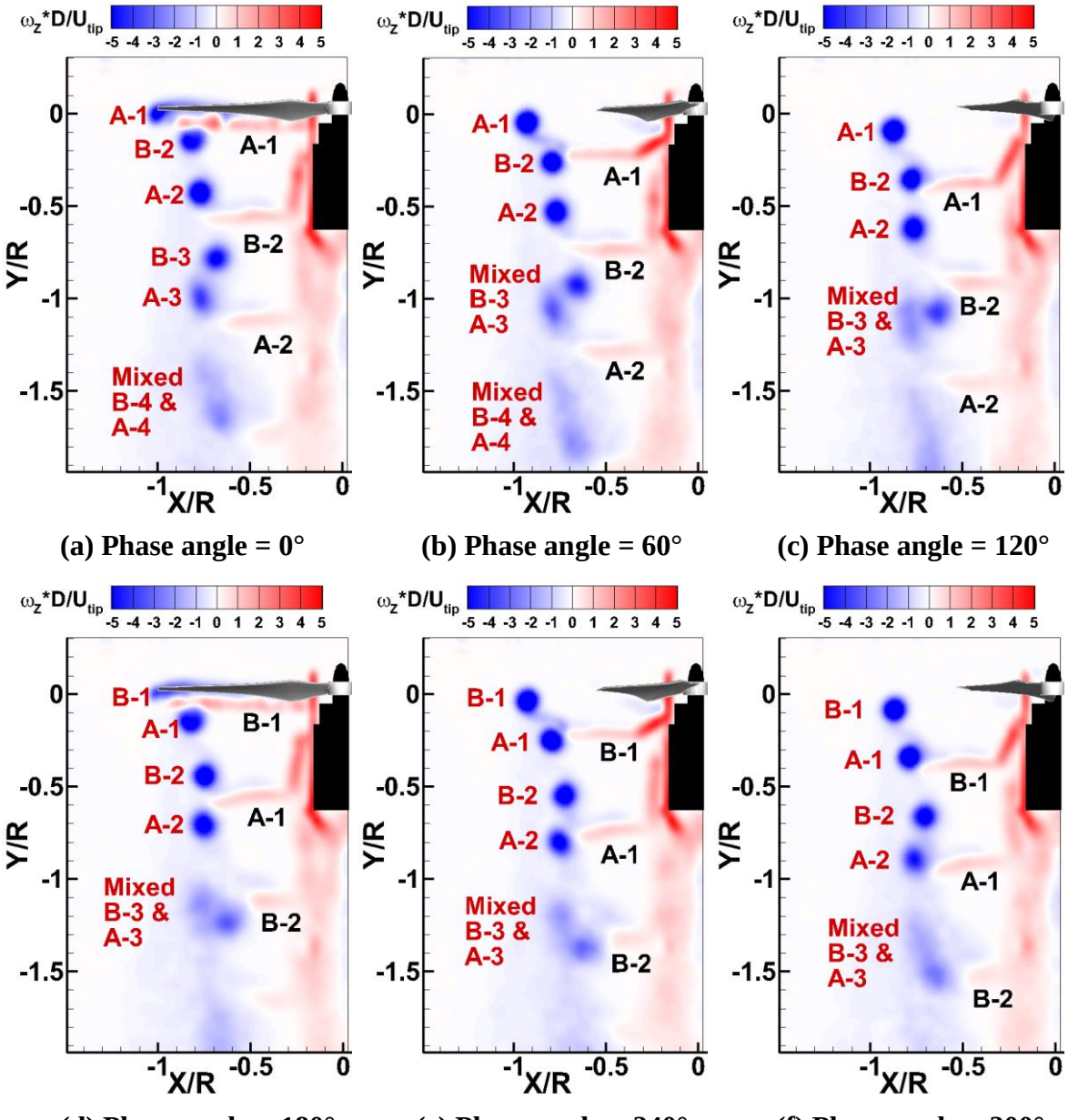

(a) Phase angle = 0° **(b) Phase angle = 60°** **(c) Phase angle = 120°**

(d) Phase angle = 180° **(e) Phase angle = 240°** **(f) Phase angle = 300°**

Fig. 8 Vorticity distributions of the "Phase-locked" PIV measurement results at different phase angles

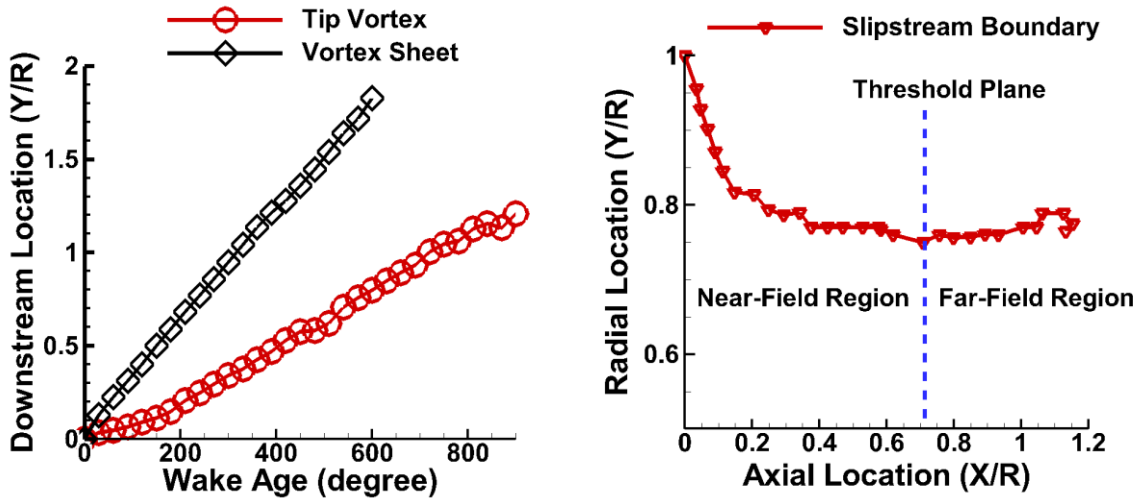

(a) Tip vortex and vortex sheet location (b) Slipstream boundary

Fig. 9 The location of tip vortex and vortex sheet of blade-1 and slipstream boundary

difference in the Y-direction. Meanwhile, they travelled towards each other due to the incoming vortex sheet B-2 push the tip vortex B-3. As shown in Fig. 10 (d), the vortex B-3 passed vortex A-3 from the side with the phase angle kept increasing. The X-direction velocity components of vortex B-3 and A-3 were almost zero and positive, respectively. As the vortex pair kept travelling to the downstream, a stretching effect was observed due to the Y-direction velocity different, which can be clearly viewed in Fig. 10 (e) and (f). This indicate the diffusion effect of the propeller wake has strong effect on the tip vortices interactions. During the interaction period, the strength of these two vortices reduced quickly due to the diffusion caused by viscosity effect. At the end, the tip vortex A-3 lost its vortex core structure and merged with vortex B-3. This tip vortices interaction phenomenon has been viewed before through flow visualization[21]. Caradonna. However, there was no flow field information, such as, velocity and vorticity. In current work, the evolution of tip

vortices interaction has been explored with detailed flow field data by using PIV technique. The dynamics process of the tip vortices interaction in current hover flight condition had similar trend with Brandt's finding[22]. In that work, Brandt studied the interactions of two unequal co-rotating vortices through numerical simulations. However, due to the existing induced flow, the tip vortices interaction in actual hover flight is not pure co-rotating vortices interaction. They have been affected by the vortex sheet and local inducted velocity a lot. The tip vortices merged and dissipated before a full roll-up motion occurred, they rotated less than 180° within one propeller rotating cycle.

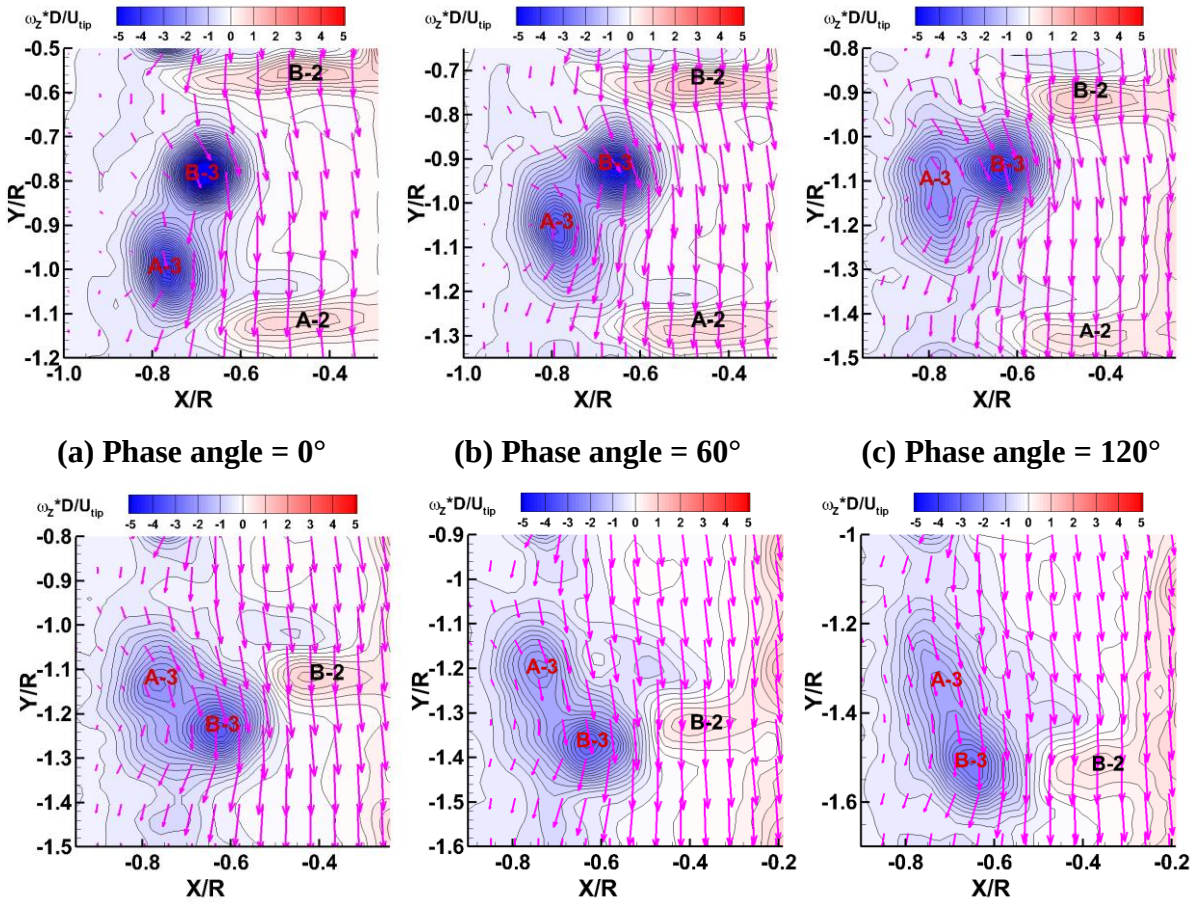

(a) Phase angle = 0° **(b) Phase angle = 60°** **(c) Phase angle = 120°**

(d) Phase angle = 180° **(e) Phase angle = 240°** **(f) Phase angle = 300°**

Fig. 10 Dynamic process of tip vortices interaction

2.4 Conclusion

An experimental study was conducted to investigate the unsteady aerodynamic thrust generated from the small UAS propeller and the detailed wake flow structure downstream of the propeller. During the experiments, JR3, a high-sensitive force-moment transducer was used to quantify the unsteady aerodynamics thrust. Meanwhile, a high resolution PIV system was used to measure the wake of the propeller through “free-run” and “phase-locked” measurements to quantify the flow characteristics.

The aerodynamic thrust measurement results clearly illustrated that the mean thrust generated from the propeller increased as a function of rotational speed with a quadratic trend. At the same time, the thrust perturbation increased with the gain of the rotational speed. The FFT analysis results explained that the increase of the thrust perturbation is mainly caused by the two blade configuration since the fluctuation of thrust at first and second harmonics of the blade passing frequency raised as the rotational speed increase.

The ensemble-average flow quantities (e.g., mean velocity and mean vorticity) of the propeller wake were obtained through “free-run” PIV measurements. Three typical flow regions: quiescent flow region, inflow region, and induced flow region, were explored. The development of the induced velocity was also obtained through this measurement.

The periodic velocity drop at the slipstream boundary was captured by “phase-locked” PIV measurements, which due to the tip vortex formation. The core structure of the tip vortices was observed in the vorticity measurement results. In addition to the tip vortices, the positive and negative vortices due to the flow passing the trailing edge also has been viewed, which was associated with the “strip shape” low speed region due to the blade cut-in. By tracking the location of the tip vortices and vortex sheet, the travelling speeds and the

slipstream boundary were achieved. Another important finding was the evolution of the tip vortices interaction. Due to the diffusion and the interaction between tip vortex and vortex sheet, the clearly roll-up motion of the tip vortices interaction started at the downstream about 0.7R. The dynamic process of the interaction from phase angle 0° to 300° was detailed explained. At the end, the previous tip vortex merge with the incoming vortex and dissipated.

References

[1] Floreano, D., and Wood, R. J., "Science, technology and the future of small autonomous drones," *Nature*, vol. 521, 2015, pp. 460–466.

[2] Bouabdallah, S., Noth, A., and Siegwart, R., "PID vs LQ control techniques applied to an indoor micro quadrotor," *2004 IEEE/RSJ International Conference on Intelligent Robots and Systems (IROS) (IEEE Cat. No.04CH37566)*, vol. 3, 2004, pp. 2451–2456.

[3] Castillo, P., Lozano, R., and Dzul, A., "Stabilization of a Mini Rotorcraft with Four Rotors," *IEEE Control Systems*, vol. 25, 2005, pp. 45–55.

[4] Madani, T., and Benallegue, A., "Backstepping Control for a Quadrotor Helicopter," *Intelligent Robots and Systems, 2006 IEEE/RSJ International Conference on*, 2006, pp. 3255–3260.

[5] Raffo, G. V., Ortega, M. G., and Rubio, F. R., "An integral predictive/nonlinear H∞ control structure for a quadrotor helicopter," *Automatica*, vol. 46, 2010, pp. 29–39.

[6] Hoffmann, G., Huang, H., and Waslander, S., "Quadrotor helicopter flight dynamics and control: Theory and experiment," *American Institute of Aeronautics and Astronautics*, 2007, pp. 1–20.

[7] Huang, H., Hoffmann, G. M., Waslander, S. L., and Tomlin, C. J., "Aerodynamics and control of autonomous quadrotor helicopters in aggressive maneuvering," *Proceedings - IEEE International Conference on Robotics and Automation*, 2009, pp. 3277–3282.

[8] Brandt, J. B., and Selig, M. S., "Propeller Performance Data at Low Reynolds Numbers," *49th AIAA Aerospace Sciences Meeting*, 2011, pp. 1–18.

[9] Merchant, M., and Miller, L. S., "Propeller Performance Measurement for Low Reynolds Number UAV Applications," *44th AIAA Aerospace Sciences Meeting and Exhibit*, 2006.

[10] Russell, C., Jung, J., Willink, G., and Glasner, B., "Wind tunnel and hover performance test results for multicopter UAS vehicles," *Annual Forum Proceedings - AHS International*, 2016.

[11] Lopez, O. D., Escobar, J. A., and Pérez, A. M., "Computational Study of the Wake of a Quadcopter Propeller in Hover," *23rd AIAA Computational Fluid Dynamics Conference*, 2017, pp. 1–9.

[12] Liu, J., and Luo, S., "Navier-Stokes Equations based Flow Simulations of Low Reynolds Number Propeller for Unmanned Aerial Vehicle," *55th AIAA Aerospace Sciences Meeting*, 2017, pp. 1–13.

[13] Ning, Z., Wlezien, R. W., and Hu, H., "An Experimental Study on Small UAV Propellers with Serrated Trailing Edges," *47th AIAA Fluid Dynamics Conference*, 2017, pp. 1–17.

[14] Ning, Z., and Hu, H., "An Experimental Study on the Aerodynamic and Aeroacoustic Performances of a Bio-Inspired UAV Propeller," *35th AIAA Applied Aerodynamics Conference*, 2017, pp. 1–15.

[15] Zhou, W., Ning, Z., Li, H., and Hu, H., "An Experimental Investigation on Rotor-to-Rotor Interactions of Small UAV Propellers," *35th AIAA Applied Aerodynamics Conference*, 2017, pp. 1–16.

[16] Eppler, R., *Airfoil design and data*, Springer Berlin Heidelberg, 1990.

[17] Leishman, J. G., *Principles of helicopter aerodynamics*, Cambridge University Press, 2006.

[18] Bristeau, P., Martin, P., Salaün, E., and Petit, N., "The role of propeller aerodynamics in the model of a quadrotor UAV," 2009.

[19] Hu, H., Yang, Z., and Sarkar, P., "Dynamic wind loads and wake characteristics of a wind turbine model in an atmospheric boundary layer wind," *Experiments in Fluids*, vol. 52, 2012, pp. 1277–1294.

[20] Verbeke, J., and Debruyne, S., "Vibration analysis of a UAV multirotor frame."

[21] Caradonna, F. X., Henley, E., Mahalingam, R., Silva, M., Huang, S., Komerath, N. M., Reddy, U., Funk, R., Wong, O., Ames, R., Darden, L., Villareal, L., and Gregory, J., "An experimental study of a rotor in axial flight," *AHS Technical Specialists' Meeting for Rotorcraft Acoustics and Aerodynamics*, 1997.

[22] Brandt, L. K., and Nomura, K. K., "Characterization of the interactions of two unequal co-rotating vortices," *Journal of Fluid Mechanics*, vol. 646, 2010, pp. 233–253.

CHAPTER 3

EXPERIMENTAL INVESTIGATION ON THE SERRATED TRAILING EDGE PROPELLER OF SMALL UNMANNED AERIAL SYSTEM

Zhe Ning, Richard Wlezien, Hui Hu

Department of Aerospace Engineering, Iowa State University, Ames, Iowa, 50011

Abstract

In the current study, three different uniform saw-tooth serrations were applied to the trailing edge of the baseline propeller to examine the noise attenuation potential of the serration on a small UAS propeller operating at a low Reynolds number (Re=40,000). The aerodynamics forces and sound pressure level at hover flight condition were obtained from high-accuracy force and sound measurements. Meanwhile, a high-resolution PIV technique was used to measure the detailed flow structure. Comparing the results between the baseline propeller and the saw-tooth serrated trailing edge propellers revealed that the serration at trailing edge reduced the noise level with no effect on the aerodynamic thrust. In addition, it has been found that noise attenuation effects increase with the serration size increasing has been founded. The flow field measurements illustrated that the serrated trailing edge propellers had a limited effect on the mean flow. However, the serration significantly changed the flow passing the trailing edge.

3.1 Introduction

Because of the reduction of the size and cost of small electronic devices (e.g., processors, sensors, and batteries), the small Unmanned Aerial System (UAS) is becoming a hot topic in both industry and academic fields[1]. As a popular platform of small UAS, the rotary-wing system has gained more attention due to the good hovering ability and vertical take-off and landing (VTOL) motion[2]. With these features, the rotary-wing UAS has been applied to many civilian applications, such as, video mapping, construction, deliveries, rescue operations, and personal entertainment. The rotary-wing UAS can fly stably to accomplish many complex tasks with well-developed control theory. However, the aeroacoustic noise is an essential problem associated with this configuration during its operation. The aerodynamics noise generated from an operating rotary-wing UAS can annoy humans, as well as wild animals[3]. For a rotary-wing UAS, the noise level increases significantly as the propeller count grows[4]. Therefore, cutting down the aeroacoustic noise level from the propeller of the rotary-wing UAS is highly desired. At the same time, the reduction in noise would also extremely broaden the working range of the small UAS[5,6].

During the operation of the rotary-wing UAS, the aerodynamic noise is generated from the propellers. The aerodynamic noise consists of inflow turbulence noise and airfoil self-noise. Between these two sources, the airfoil self-noise contributes a larger percentage to the total noise level. Brooks[7] investigated the airfoil self-noise generation mechanism, and divided it into five categories. Among these five types, four of them are linked to the flow interaction between turbulence and trailing edge. By modifying the trailing edge with a saw-tooth serration, a bio-inspired geometry, noise attenuation can be achieved. Current experimental and theoretical research on 2-D flat plate, symmetric airfoils and asymmetric

airfoils approved that the trailing edge serration could decrease the scattering efficiency, which results in a reduction of the trailing edge turbulent noise[8–14]. Gruber found that the serrated trailing edge could reduce the noise when the St is smaller than 1 and increase the noise level when St is larger than 1[8]. Moreau[12] and Herr[9] conducted experiments and concluded that the serrated trailing edge also had the potential to weaken the vortex shedding noise if the ratio of the trailing edge thickness to boundary-layer displacement thickness is larger than 0.3. From the aerodynamics perspective, the saw-tooth serrated trailing edge had limited effect on lift. However, it would increase the drag coefficient and the turbulence[6,8,9,13]. This is because the serration would increase the turbulent mixing at trialing edge and reduce the correlation length of turbulence[12]. By adding the saw-tooth serration to the trailing edge of a wind turbine prototype, Oerlemans[14] discovered that broadband noise emitted from the wind turbine had been reduced substantially.

Although the saw-tooth serration has been tested near the trailing edges of flat plates, symmetric and asymmetric airfoils, and real wind turbine blades at relatively high Reynolds numbers[8–10,13–17], no research was found investigating the effects of serrated trailing edges on the aerodynamic and aeroacoustic performances of a small UAS propeller operated at much lower Reynolds numbers (~10^4). In order to get a better understanding about the variation of aerodynamics forces, noise emission, and flow structure in the wake due to the serrated trailing edge, an experimental study has been performed to examine the aerodynamic and aeroacoustic characteristics of serrated trailing edge propellers under hover flight condition.

3.2 Propeller models design and experimental setup

3.2.1 The design of the baseline and serrated trailing edge propellers

In the present study, an E63 airfoil[18] (low Reynolds number airfoil) was used to design the baseline propeller in order to generate 3N designed thrust. Due to the strength concerns the thickness of the airfoil was doubled along the camber line. The baseline propeller had a diameter of 240mm and tip chord of 8mm. The chord lengths along the propeller radius from tip to 30% radius were calculated by the optimal chord length equation $C_r = \frac{c_{tip}}{r}$, where C_r is the chord length at the corresponding radius location, and r represents a non-dimensional radial distance, which is 0 at the rotating center and 1 at the tip[19]. The twist angle of the baseline propeller at the tip and 30% radius from the center were 11.6° and 28.1°, respectively. In previous studies, researchers always added the saw-tooth serration directly on the trailing edge of the 2D flat plate or airfoils[8,10,13]. In addition, Oerlemanse added the saw-tooth serration on the trailing edge of the wind turbine prototype in the rotating motion study[14]. Therefore, in current studies, the saw-tooth serrations were added to the trailing edge of the baseline propeller with three different sizes, shown in Fig.1. According to Howe[11], in order to use the saw-tooth serration at the propeller trailing edge to reduce noise, some important geometry parameters need to be considered. Fig. 2 shows the geometry of a typical saw-tooth serration, where 2h is the serration height (or amplitude), λ is the width, and Θ is the inclined angle. The ratio between half height of the serration and the boundary layer thickness at the trailing edge (h/δ) should larger than 0.25, otherwise the amplitude of the serration is too small, and the turbulent eddies pass over the saw-tooth without significant interaction. Thus, the system would experience no noise reduction. Secondly, the inclined angle should be less than 45 degrees, which means the width/height ratio (λ/h) of the

serration will smaller than four. In current work, the three different serrations have the same height (2h=6mm), which is larger than 0.25 of the boundary layer thickness. The three serrated trailing edge propellers had width/height ratios (λ/h) of 0.6, 0.9, and 1.2, respectively. These design parameters will ensure the inclined angle of the serration is lower than 45 degrees. All of the propellers were manufactured by a high-accuracy 3-D printing machine with a layer by layer resolution of 20 microns. The materials of the propellers were hard plastic (VeroWhite).

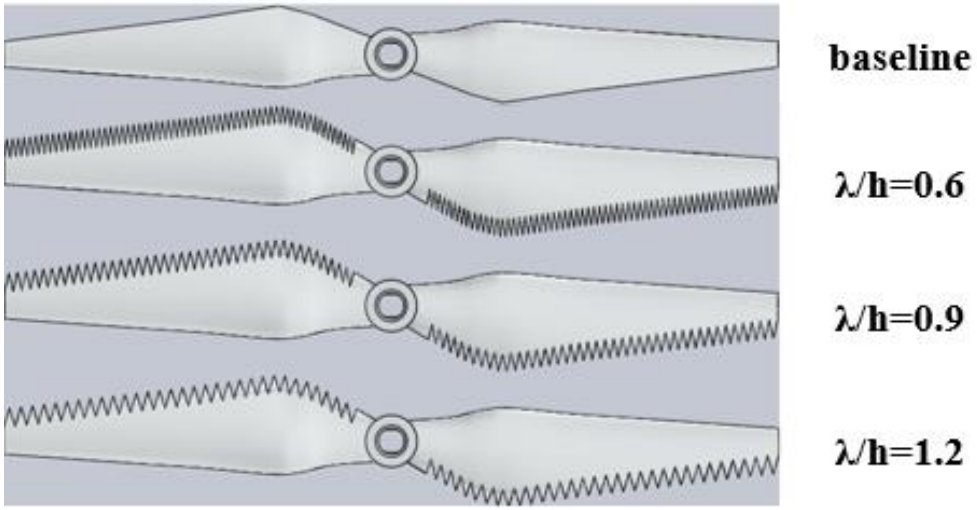

Figure 1. The baseline propeller and the saw-tooth serrated trailing edge propellers

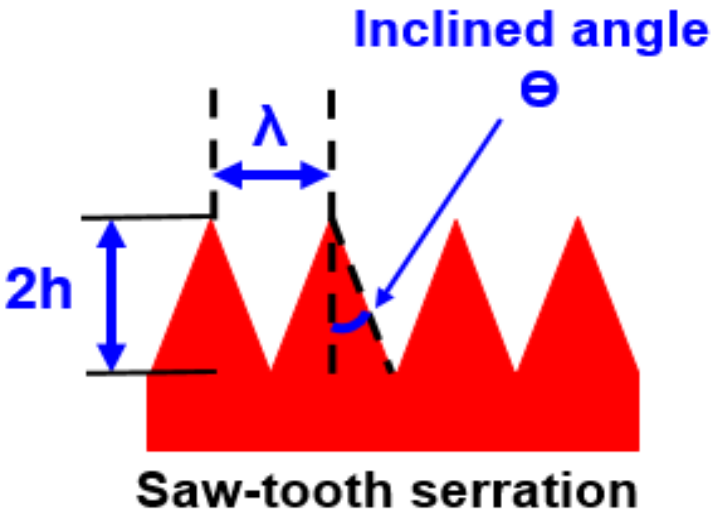

Figure 2. Saw tooth serration geometry sketch

3.2.2 Experimental setup for the measurements

The aeroacoustic noise measurement was conducted in an anechoic chamber (as shown in Fig. 3 (a)) located in the department of aerospace engineering at Iowa State University, with a physical dimension of 12×12×9 feet. The chamber provided a 100Hz cut-off frequency and about 20dB background noise level with respect to the reference of 20μpa. In the current measurement, the rotor was operated at hover flight condition (thrust=3N). Each measurement lasted for 30 seconds. As shown in Fig. 3 (b), the sound spectrum measurement was conducted at hub height and 5D away from the center of the propeller at 0° azimuth angle. The 5D separation distance was chosen because it can be considered as the far wake. In the near wake (<3D), the turbulence levels of the surrounding flow were high, which would affect the results of the sound measurement. In the Fig. 3, the blue mark represented the measurement location and the red arrow indicates the induced airflow direction.

In the current study, the aerodynamic forces and detailed flow structure downstream of the propeller were also measured in addition to the aeroacoustic measurement. The experimental setup used in the current study was shown in Fig.4. The propeller was driven by a brushless motor (i.e., dji 2212) with the power from a direct current power supply. The voltage of the power supply was kept at 11.1 V for all the measurements. The rotational speeds of the propellers ranged from 0 to 6000 RPM, which was determined by the signal from a function generator via an electronic speed controller. During the test, a tachometer was used to detect the pre-marked blade to quantify the rotational frequency. Meanwhile, a pulse signal was generated. This signal was used for the “phase-locked” PIV measurement later. The aerodynamic forces were measured by a high-sensitivity force-moment sensor (JR3

load cell), which had a precision of ±0.1N (± 0.25% of the full range). It should be mentioned that a 0.2D clearance gap was maintained to reduce the flow interaction between the support rod and propeller. The 0.2D is a typical separation distance for a small UAS.

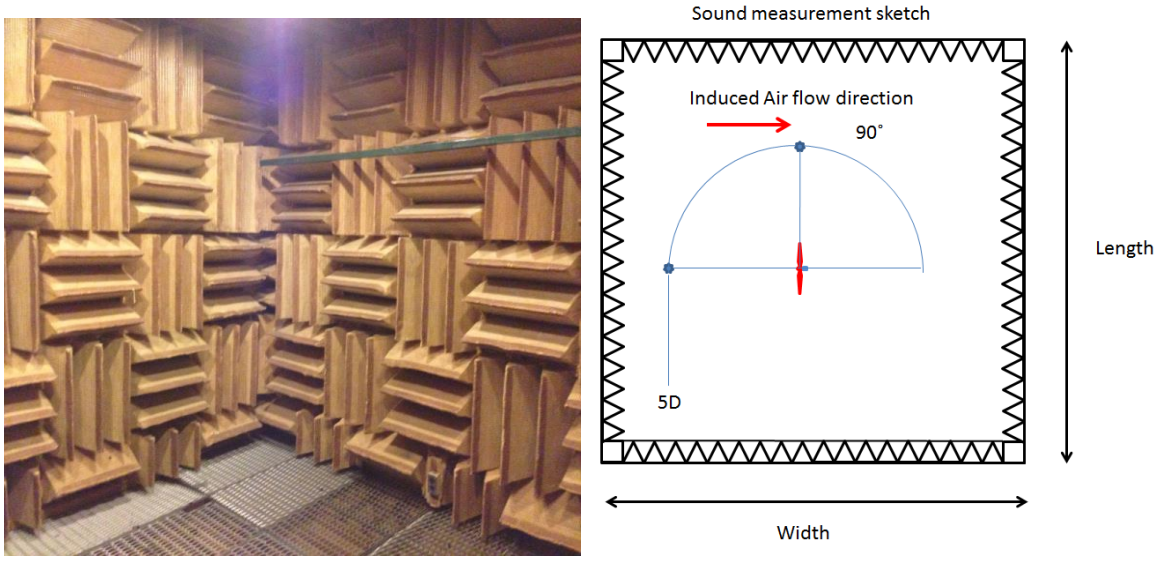

(a) (b)

Figure 3. The anechoic chamber used for aeroacoustic measurements and the sound measurement sketch

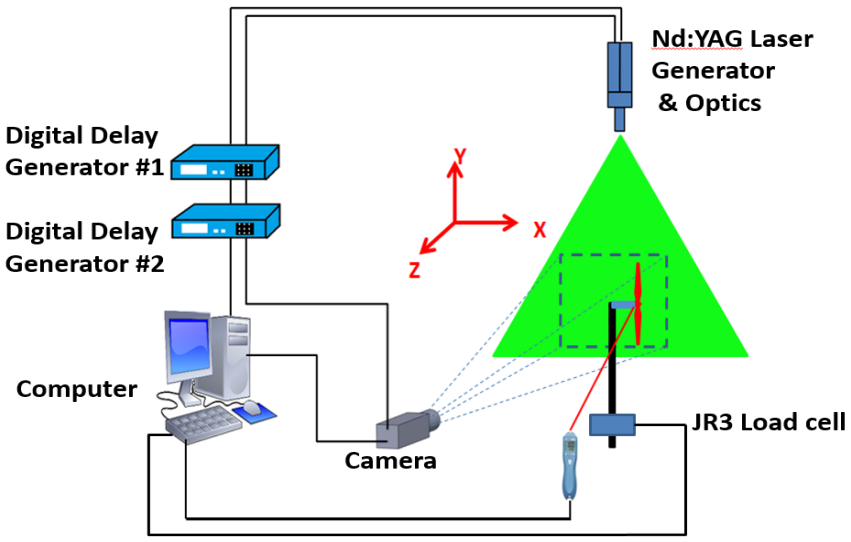

Figure 4. Experimental setup for force and PIV measurements at hover flight motion

In order to quantify the detailed flow structure downstream of the propellers, a high-resolution digital PIV system was used. Both “free-run” and “phase-locked” PIV measurements were conducted to achieve the ensemble-average flow structure and detailed flow structure at certain phase angles. For the “free-run” measurement, 1000 frames of instantaneous PIV measurements were used to generate the ensemble-average results. The phase-locked PIV measurements were conducted at 6 different phase angles ranging from 0° to 150° with 30° increments. Each of the phase-average result was calculated from 255 frames of instantaneous measurements. During the PIV measurement, about 1μm water-based droplets generated by the fog machine (i.e., ROSCO 1900) seeded the whole flow field as the tracer particles. The field illumination was provided by a double-pulsed Nd:YAG laser generator with a power of 200mJ per pulse at a wavelength of 532nm. Through a set of optics, the laser beam was formed into a thin laser sheet with an approximate thickness of 1mm at the test section. A high-resolution (2048×2048 pixels) charge-coupled device (CCD) camera with an axis perpendicular to the laser sheet was used to capture the raw images of the local flow. In order to cooperate the laser illumination and image taking, the camera and laser generator were connected to the computer via a digital delay generator to control the timing. A second digital delay generator was used to add a delay time to the signal from the tachometer to acquire “phase-locked” PIV measurements at different phase angles.

3.3 Measurement results and Discussions at hover flight motion

3.3.1 Aerodynamics force measurement results at hover motion

As listed in the Table 1, the aerodynamics forces of the baseline and three serrated trailing edge propellers were measurement at different rotational speeds ranging from 0 to

6000RPM. Fig. 5 illustrates the power requirements and rotational speed variations at different thrust values. The designed thrust was represented by a dashed line and the symbols indicated the measurement results of the aerodynamic forces. Each symbol denoted an average value of a 30 seconds measurement with a sampling frequency of 1000Hz. As shown in Fig.5 (a), the power requirement of the baseline propeller was the same as the three serrated trailing edge propellers. They all needed 36 watts to generate the 3N designed thrust. This means that the saw-tooth serrated trailing edge had no effect on the aerodynamic thrust generation, which leads to the same conclusion as previous research work[8,9]. The mean flow structure provided in the flow field measurement further support detailed explanation of this result. Meanwhile, as shown in Fig. 5 (b), the serrated trailing edge propellers rotated slightly slower than the baseline propeller when they generated equal thrust. The equal thrust generation means power input was the same, namely torque input was constant. Under constant torque, the decreased rotational speed means the drag increased. The increase in drag due to the serrated trailing edge has also been reported by Gruber[8,9].

Table1. Test conditions of the force measurement at hover flight motion

Blade type	Rotational direction	Voltage Condition	Rotational speed (RPM)
Baseline propeller	CCW (Counter Clock-wise)	11.1	0-6000
Propeller with Saw-tooth serration at λ/h=0.6	CCW (Counter Clock-wise)	11.1	0-6000
Propeller with Saw-tooth serration at λ/h=0.9	CCW (Counter Clock-wise)	11.1	0-6000
Propeller with Saw-tooth serration at λ/h=1.2	CCW (Counter Clock-wise)	11.1	0-6000

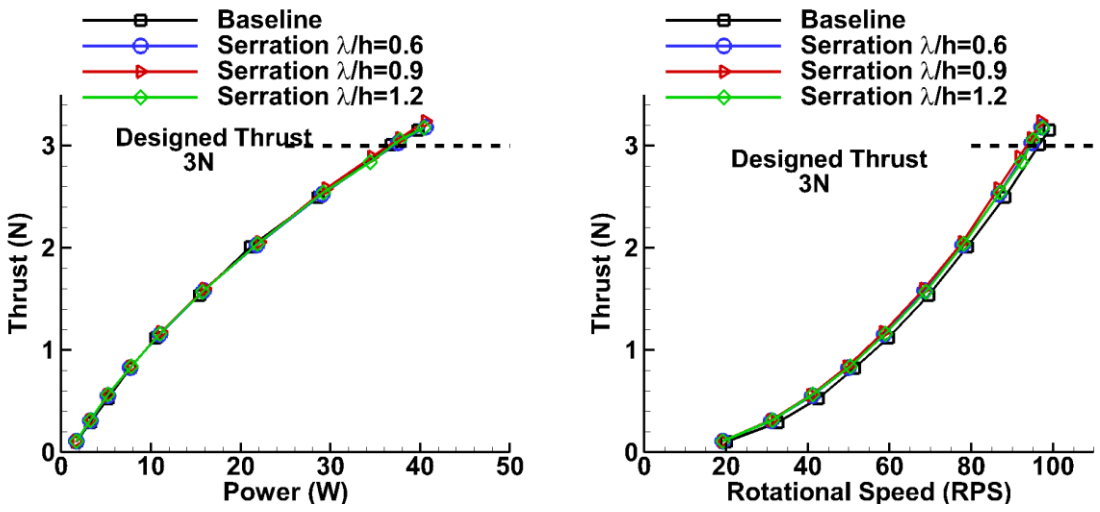

(a) (b)

Figure 5. force measurement results of 4 propellers at different rotational speeds

3.3.2 Sound measurement results at hover motion

In addition to the aerodynamic force measurement, a sound measurement also has been conducted. The baseline propeller and serrated trailing edge propellers were placed in the anechoic chamber to investigate the noise attenuation effect due to the serrations. During the measurement, the propeller operated at hover motion, a unique flight condition for vertical take-off and landing aircraft, where the thrust created by the propeller was equal to the aircraft weight. The effect of the noise attenuation due to the serrated trailing edge was analyzed through a spectrum comparison. The sound pressure level was calculated by Equation 1, where the reference pressure was 2μPa. The measured sound pressure level (SPL) comparison results at low frequency are shown in Fig. 6 (a), (c), and (e). It canbe easily found that the serrated trailing edge had no significant effect on the low frequencies. The peaks in the plot, known as the tonal noise, which are associated with the blade passing frequency (rotational frequency times number of the blades). As mentioned in the previous

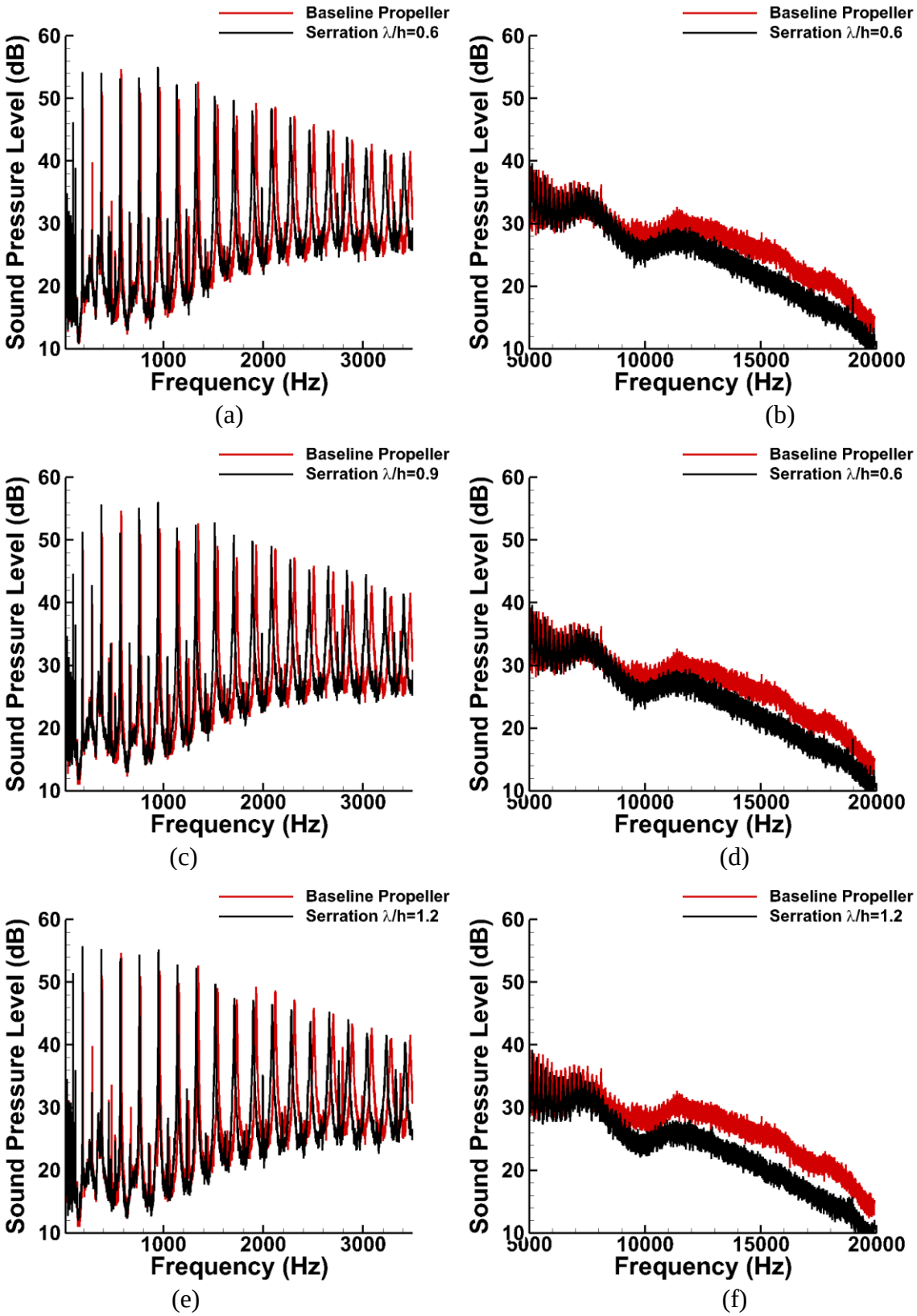

Figure 6. Sound spectra distributions comparison between the baseline propeller and three serrated trailing edge propellers at low frequency (left) and high frequency (right)

section, the serrated trailing edge propellers rotated slightly slower than the baseline propeller. Therefore, a slightly shift in the tonal noise component in the frequency domain has been found in these three figures. For a propeller operated at a low Mach number (M<1), the tonal noise is dominant by the loading noise. With the very similar loading on the four propellers, the similar tonal noise components could be expected. On the other hand, the noise attenuation effect due to the serrated trailing edge was found most significant at high frequencies. The serration on the trailing edge can increase the mixing of the turbulent flow and reduce the correlation length of the turbulence[8,11,13]. Therefore, the scattering efficiency of the turbulent boundary layer trailing edge noise would decrease. As mentioned before, the experimental researches show that serration will decrease the noise in the frequency domain when St<1, and increase the noise level at a Strouhal number greater than 1[8,9]. In present study, by using equation 2, the estimated boundary layer thickness was 0.22mm based on tip chord length (~8mm) and tip speed (~71m/s). The frequency corresponding to St=1 is 320,000Hz. Although the sound measurement results only present up to 20,000 Hz, noise attenuation effect was observed in this domain, which partially form the same conclusion. Another important observation was that as the serration sizes increased the noise attenuation effect also increased. This can be viewed clearly in the Fig. 6 (b), (d), and(f). It was found that the serrated trailing edge propellers with λ/h ratios of 0.6, 0.9, and 1.2 reduced the noise by 0.9dB, 1.4dB, and 1.6dB ralative to the baseline propeller, respectively, by integrating the sound pressure at the human ear hearing domain (20-20k Hz). This trend was also reported by Moreau[13] and Chong[15]. One possible reason for this phenomenon could be that the vortex pairs generated from the side edges of the serration restrict the mixing. As mentioned by León[20], a pair of vortices will be generated when the flow passes over the serration. Because

of the pressure difference between the two serrations, the vortex pairs will create an upwash flow between the serrations, and a downwash flow at the tip of serration. This vortex pairs would benefit the turbulence mixing process. However, if the serration is too fine, the vortex pairs could interact with each other and restrict upwash flow between the serrations. Thus, the turbulence mixing may be reduced. Therefore, the noise attenuation effect may be decreased.

$$SPL\ (dB) = 20\ log_{10}\left(\frac{p}{p_{ref}}\right)(dB) \tag{1}$$

$$\delta^* = \frac{0.37C}{8Re_C^{0.2}} \tag{2}$$

$$\mathrm{St} = \frac{f\delta^*}{U} \tag{3}$$

3.3.3 Flow field measurement results at hover motion

As mentioned before, a high-resolution PIV system was used to investigate the detailed flow structure in the downstream of the four propellers at hover flight condition. The typical “free run” PIV measurement results of the baseline propeller was shown in Fig. 7. The term “free run” means the image capture frequency and the propeller rotational frequency were not harmonic. Fig. 7 (a) shows the raw image acquired by the CCD camera. The tip vortex structures were revealed downstream of the propeller in a queue, which can also be found in the instantaneous and “phase locked” PIV measurement results. In addition to the tip vortex, the vortex structure due to the blunt body effect of the motor and the vorticity fluctuations can be viewed clearly in Fig. 7 (b). Three typical flow regions can be easily identified from the ensemble-averaged velocity results in Fig. 7 (c) . The large blue

region denoted the quiescent flow region, where the flow velocity magnitude is small (<2m/s). The region above the propeller known as the inflow region. Due to the propeller rotation, the flow was sucked into the rotating plane and pushed downward to generate thrust. The region below the propeller is called the induced flow region. In this region, the flow velocity is higher than the other two regions. Because of the low pressure at the high velocity region, the flow shrunk inward. Fig. 7 (d) represents the ensemble-averaged vorticity results. Instead of clear tip vortex structures, the tip vortex region and the vortices after the motor are very obvious. The dissapation rate of these two types of vortice were high. Due to the dissipation, the size increase in the tip vortex region can be clearly obseved.

Fig. 8 shows the ensumble-average velocity comparison results among the baseline and the serrated trailing edge propellers. From the contour plot, it can be easily identified that these four propellers generated almost identical flow structure and velocity distribution in the downstream. Accoding to the momentum theory, the thrust generated from the propeller is proporional to the induced velocity. Therefore, the identified velocity distribution means the serrated trailing propellers generate thrust equal to the baseline propeller at hover flight motion. The similarity in the velocity distribution was another further evidence supporting the arguement that the serrated trailing edge had no significant effect on the aerodynamic thrust.

In addtion to the “free run” PIV measurements, “phase-locked” PIV measurements were conducted to obtain the detailed flow characteristics in the downstream, and to better understand the flow phenomena and the aerodynamic effect due to the saw-tooth serrated trailing edge. In the present study, the flow structure downstream of the propellers were studied at six different phase angles range from 0° to 150° with 30° increments. Fig. 9

represents the velocity and vorticity distributions of the baseline propeller at phase angle 0° and 120°. The 0° phase angle means the propeller is just cutting the measurement plane. Same as the "free run" PIV measurement results, three typical flow regions were also obseved in "phase-locked" PIV measurment results. One phenomenon was not captured by the "free run" PIV measurement was the periodic velocity deficit located at the boundary between the induced flow region and quiescent region in the near wake (within one radius). This is mainly because of the blade tip cutting the flow, which results in the formation of the tip vortices. Tip vortex, a typical flow structure in the wake, was generated at the tip of the propeller due to the pressure difference between pressure side and suction side. This structure can be found in the vorticity distribution, figure 9 (c) and (d). With the phase angle increased from 0° to 120°, the tip vortex structure traveled downstream and shrank inwards because the induced velocity was low at the tip and high in the middle, which resulted in a low-pressure

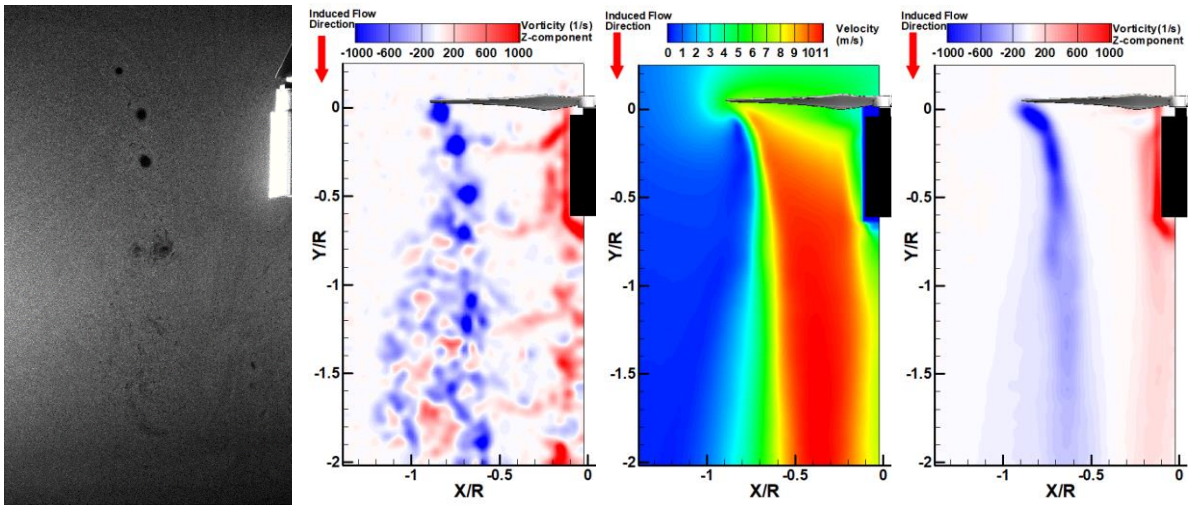

(a) Raw image (b) Instantaneous vorticity (c) averaged velocity (d) averaged vorticity

Figure 7. "Free run" PIV measurement results of baseline propeller at hover motion

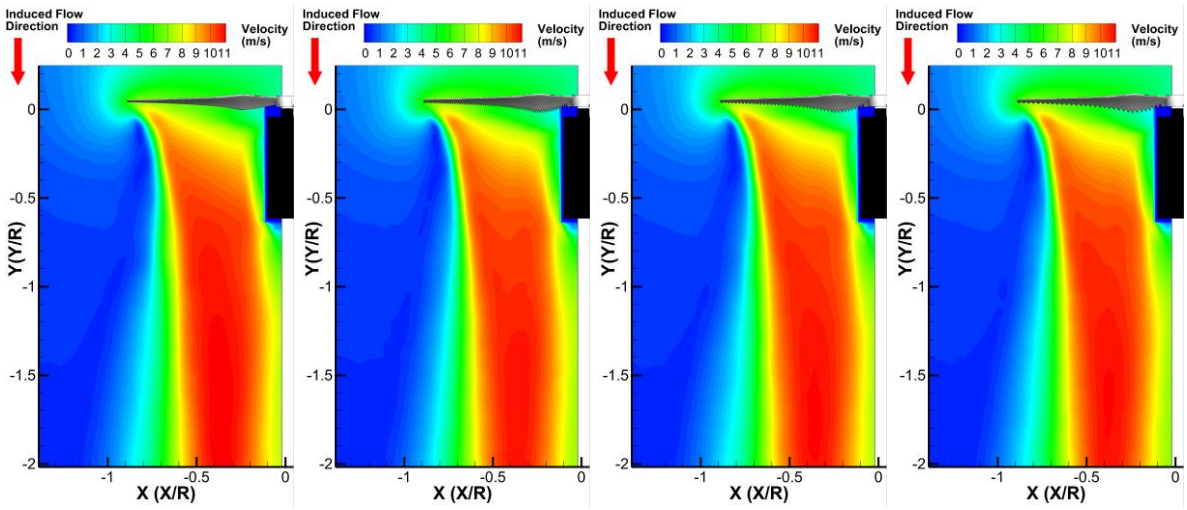

(a) baseline (b) serration λ/h=0.6 (c) serration λ/h=0.9 (d) serration λ/h=1.2

Figure 8. Ensemble average velocity comparison results of baseline and serrated trailing edge propellers

region in the middle section. Another interesting phenomenon observed was the tip vortex interaction. It starts at about 0.6 R downstream, the incoming tip vortex structure started to interact with the previous one. These two tip vortices mixed and dissipated at about 1.2 R downstream. This mixing and dissipation resulted in the tip vortices getting larger while losing their strength, and the core structures disappearing. Besides the tip vortices, both positive and negative vorticity regions created by the flow passing the trailing edge of the propeller can be viewed in all the plots. The strength of these vortices is smaller compared to the tip vortices. Because the velocity gradient was small going from tip to center, the results was almost parallel to the rotating plane. This pair of vortices began to mix with the surrounding wake and dissipated at about one rotor radius downstream. Although the serrated trailing edge had no effect on the mean flow structure, it does affect the instantaneous flow struture, especilly the flow passing over the trailing edge. Fig. 10 represents the vorticity distribution results of the baseline and serrated trailing edge propellers at the 90° phase angle. The structure and strength of the tip vortices of between the three serrated trailing edge

propellers was almost the indentical compared to the baseline propeller. However, the flow structure of the vortices due to flow passing trailing edge were found to be significantly different. It could be found in the figure that the tilting direction of these vorticity pairs of the baseline propeller were different from the three serrated trailing edge propellers at the downstream between 0.5R to 1.5R. This is because the velocity difference in the downstream is caused by the serrated trailing edge at any instantaneous time. As illustrated by León[20], a pair of vortices will be generated after the flow passes the serration. This vortex pair would benefit the turbulence mixing process and alter the pressure distribution downstream of the trailing edge, resulting in a velocity variation after the flow passes trailing edge. The velocity distributions of the baseline and serrated trailing edge propellers at the different downstream locations in the wake are given in figure 11. At about 0.2R downstream, the three serrated trailing edge propellers generated higher velocity at the tip and lower velocity at the middle span compared to the baseline propeller. At about 0.7R downstream, instead of a single hump shape, the velocity distributions of the three serrated trailing edge propellers produced double humps. Further downstream, the velocity distributions of the four propellers formed a parabolic shape with peak value shifts. These differences in the velocity distribution proved that the serrated trailing edge affected the flow passing it. One interesting phenomenon is that the velocity distributions of the serrated trailing edge propellers with λ/h ratios of 0.9 and 1.2 were very similar. And according to the sound measurement results, these two propellers also had a better noise reduction effect than the smallest serration size propeller.

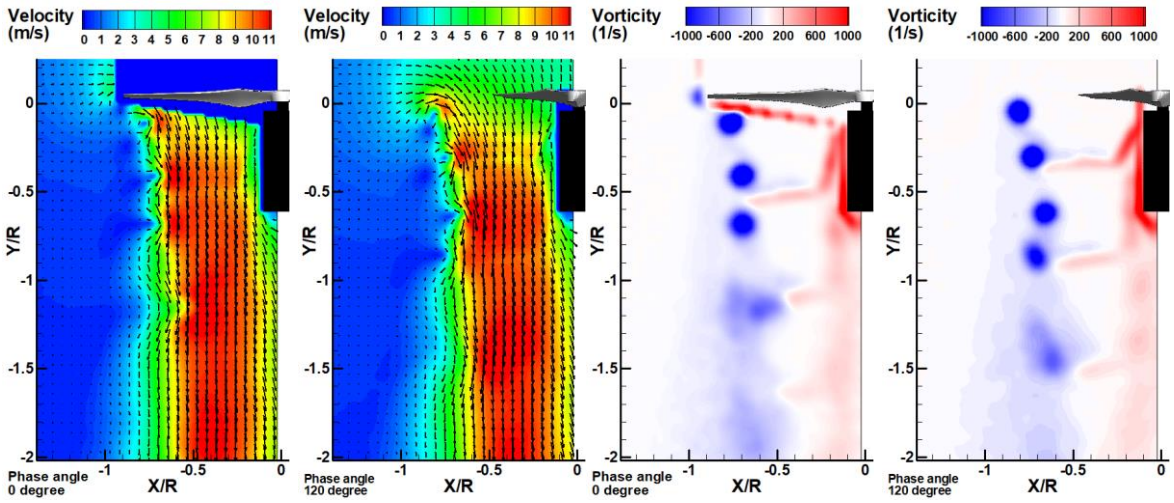

(a) (b) (c) (d)

Figure 9. "phase-locked" PIV measurement results of the baseline propeller at 0° and 120° phase angle

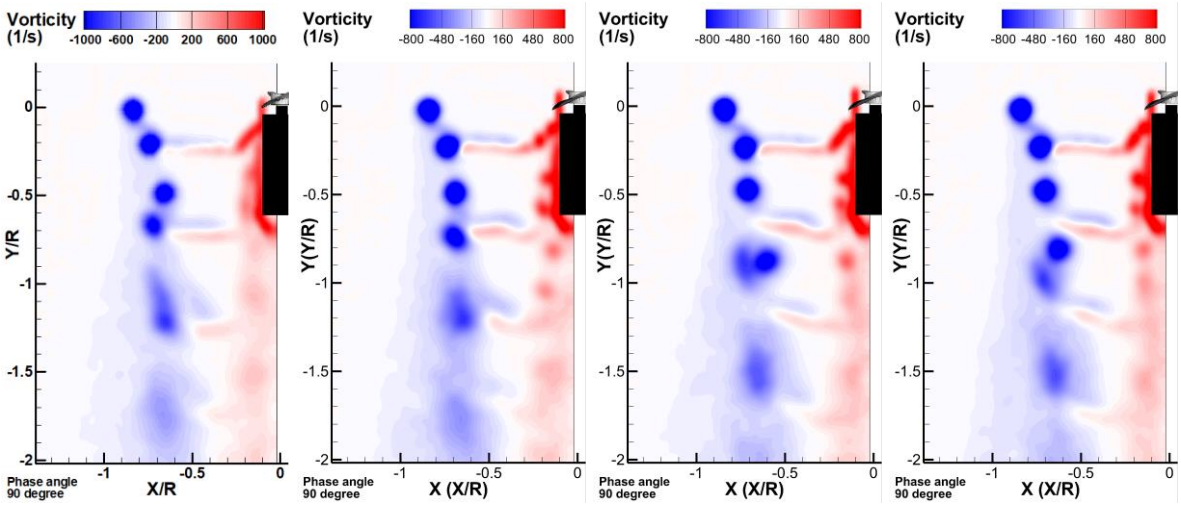

(a) baseline (b) serration λ/h=0.6 (c) serration λ/h=0.9 (d) serration λ/h=1.2

Figure 10. Vorticity comparison between the baseline propeller and three serrated trailing edge propellers at 90° phase angle

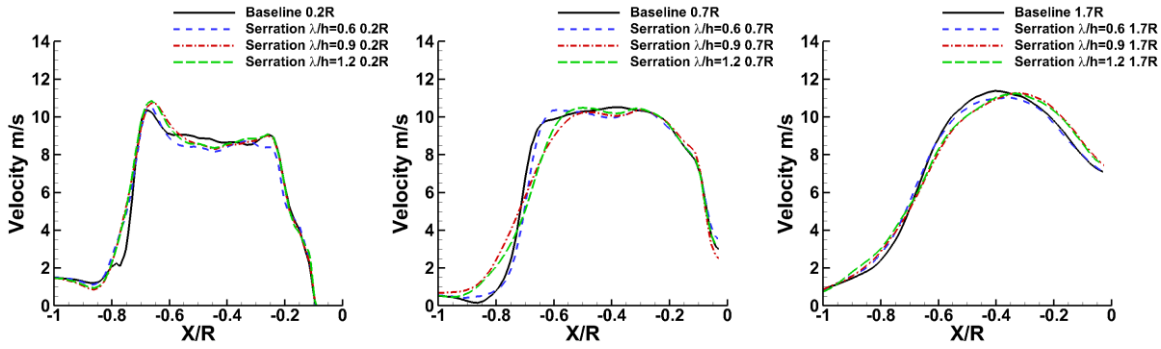

(a) 0.2R downstream (b) 0.7R downstream (b) 1.7R downstream

Figure 11. Velocity comparison are different downstream location

3.4 Measurement results and discussions at forward flight motion

3.4.1 Aerodynamics force measurement results at forward flight

In addition to the hover motion analysis, the aerodynamic force was also measured in the forward flight condition. Since the smallest serration size propeller had poor aerodynamic performance due to geometry deforming, the forward flight study was only focused on the baseline propeller and the SSTE propellers with λ/h ratios of 0.6, 0.9, and 1.2. The power versus lift results at different pitch down angles are shown in figure 12. Compared to the baseline propeller, all three of the serration propellers required the same power to generate equal thrust. With the pitch down angle increasing, more power was required to create same lift. Figure 13 shows the lift versus rotational speed comparison results of the 4 different propellers. Unlike in the hover motion test, all three SSTE propellers rotated slower than the baseline propeller at forward flight when they generated the same lift. In forward flight, the baseline propeller rotated about 5 Hz faster than the SSTE propellers. The three SSTE propellers had same rotational speed and required same power input to produce equal lift, which indicated that the serration size did not affect the lift generation. As mentioned by

Gruber, the serration has no significant effect on the lift generation[8,9]. However, it would slightly increase the drag coefficient. Under constant torque, this drag increase would cause the rotational speed to decrease. With this change in the rotational speed, the operating angle of attack would also vary. This phenomenon would lead to the same lift generation. In order to generate same lift, the rotational speed of all of the propellers would need to increase to match the effects of the pitch down angle increasing.

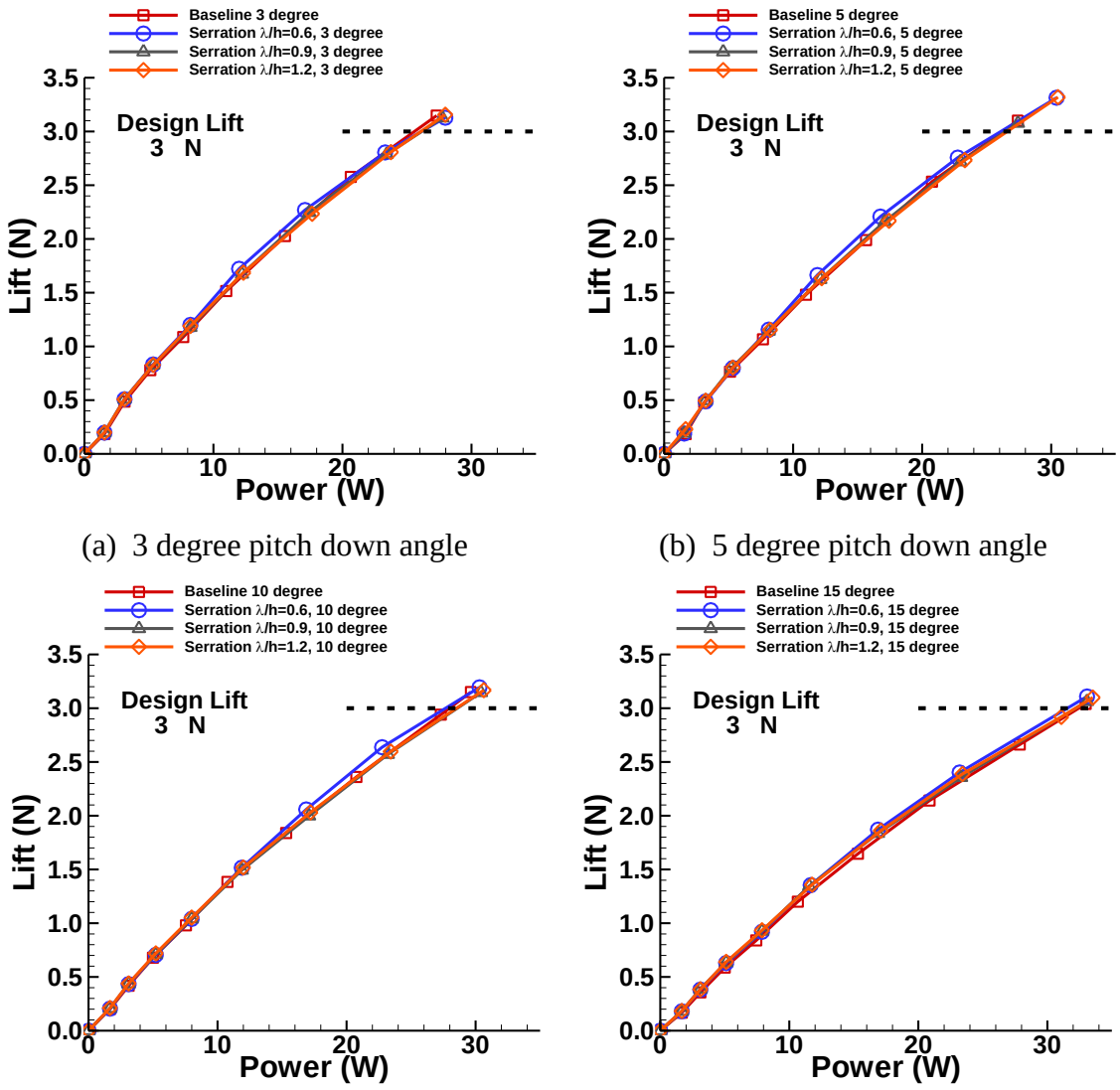

(a) 3 degree pitch down angle

(b) 5 degree pitch down angle

(c) 10 degree pitch down angle

(d) 15 degree pitch down angle

Figure 12. Lift vs power at different pitch angle of baseline and serrated trailing edge propellers

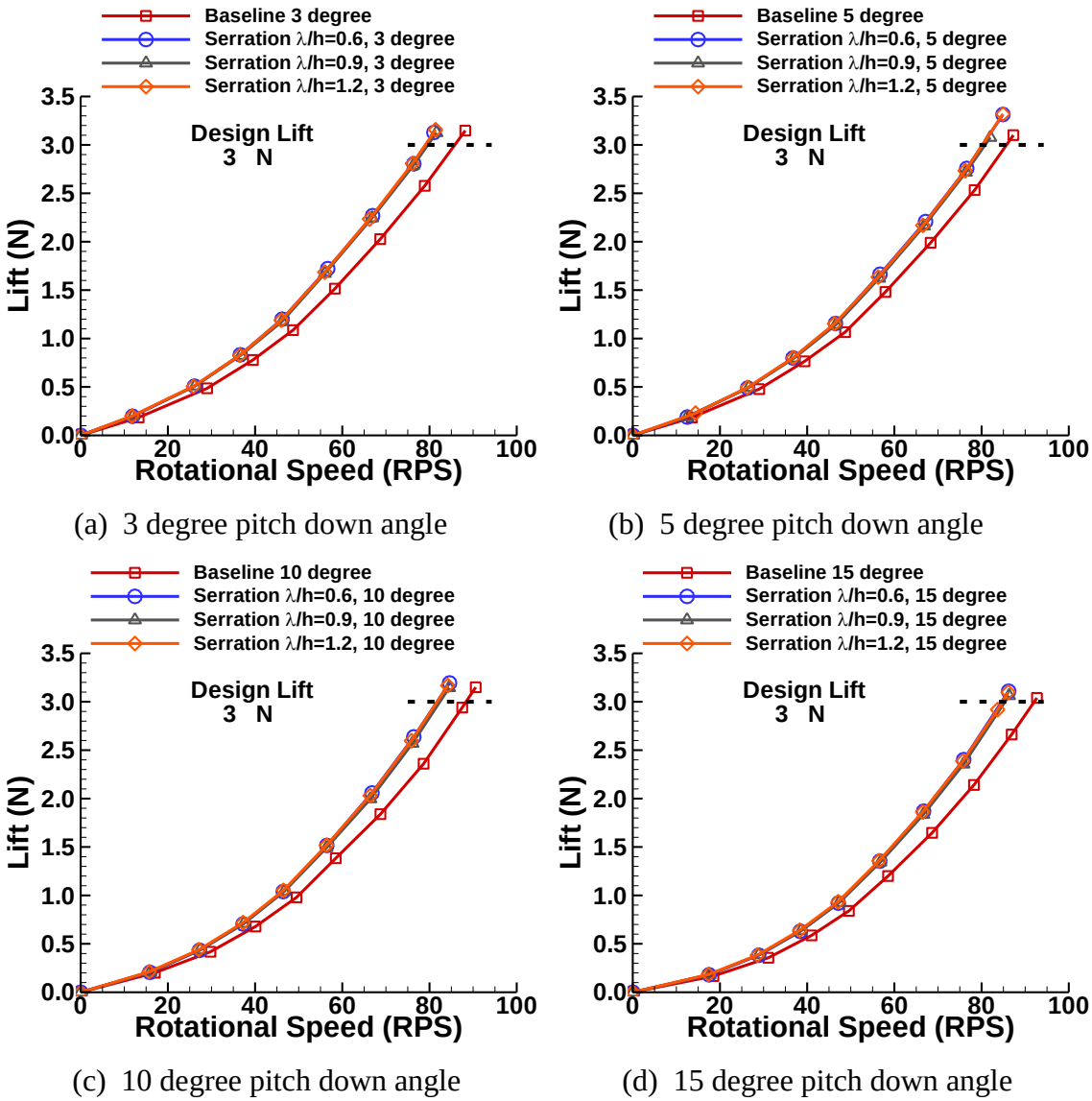

(a) 3 degree pitch down angle (b) 5 degree pitch down angle

(c) 10 degree pitch down angle (d) 15 degree pitch down angle

Figure 13. Lift vs rotational speed at different pitch angle of baseline and serrated trailing edge propellers

3.4.2 Flow field measurement results at forward flight

The flow field measurements were also conducted in forward flight. Since the propeller is not perpendicular to the incoming flow, the relative velocity of the two side blades will be different. As shown in figure 14, the blade which rotates into the incoming flow is the advacing blade, where relative velocity is the rotational speed plus the incoming

flow speed at 0 degrees pitch down angle. The blade which rotates with the incoming flow called retreating blade, where relative velocity is the rotational speed minus the incoming flow speed at 0 degrees pitch down angle. Therefore, at certain region close to the center, the incoming flow velocity is higher than the rotaitonal speed. As a result, the air flows from trailing edge to the leading edge. This region is called reverse flow region. The velocity distribution sketch of longitudinal and lateral inflow are also provided in this figure. Figure 15 shows the “free run” PIV measurement results of the 4 propellers with 10m/s wind speed and 10 degree pitch down angle in the middle plane. The two high velocity regions in the wake can be clearly viewed in all the plots. This is induced by the propeller rotation. The vorticity due to the flow passing motor also can be viewed down to the rotor. The flow field of the SSTE propellers were very similar to the baseline propeller. By tracking the velocity

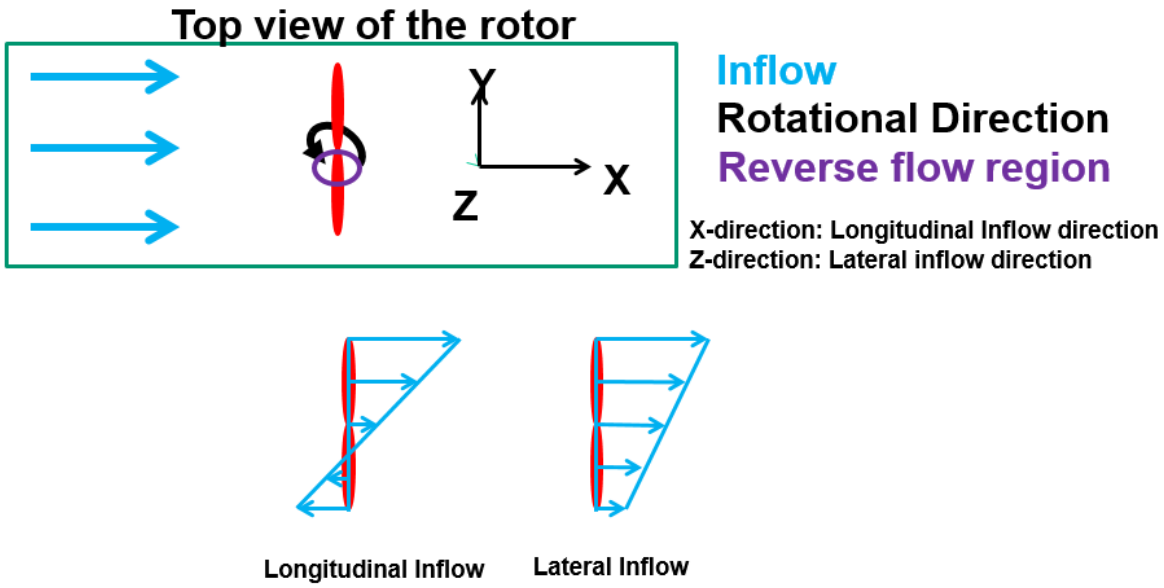

Figure 14. flow sketch at forward flight

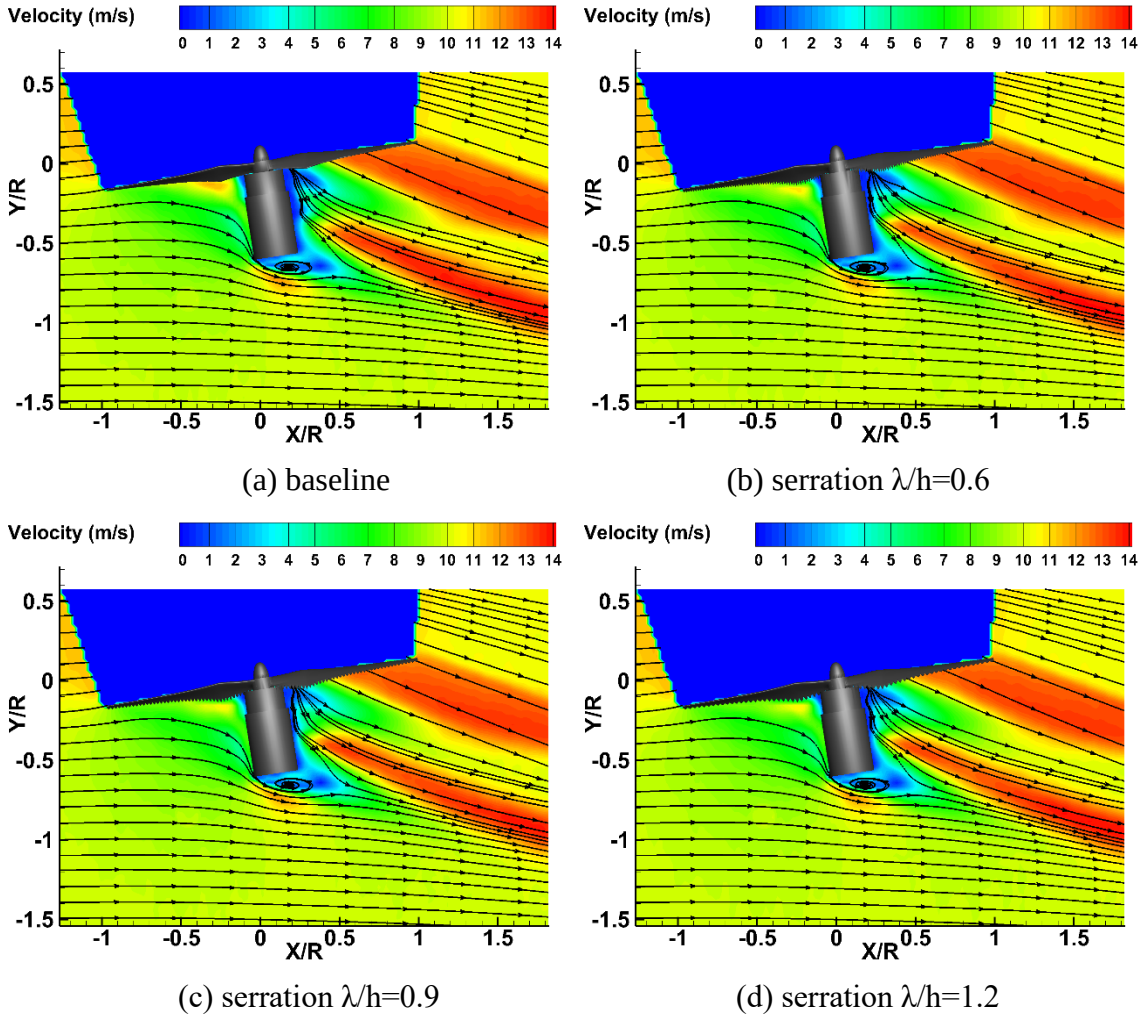

(a) baseline (b) serration λ/h=0.6

(c) serration λ/h=0.9 (d) serration λ/h=1.2

Figure 15. Ensemble-averaged velocity of the "free-run" PIV measurement results at forward flight

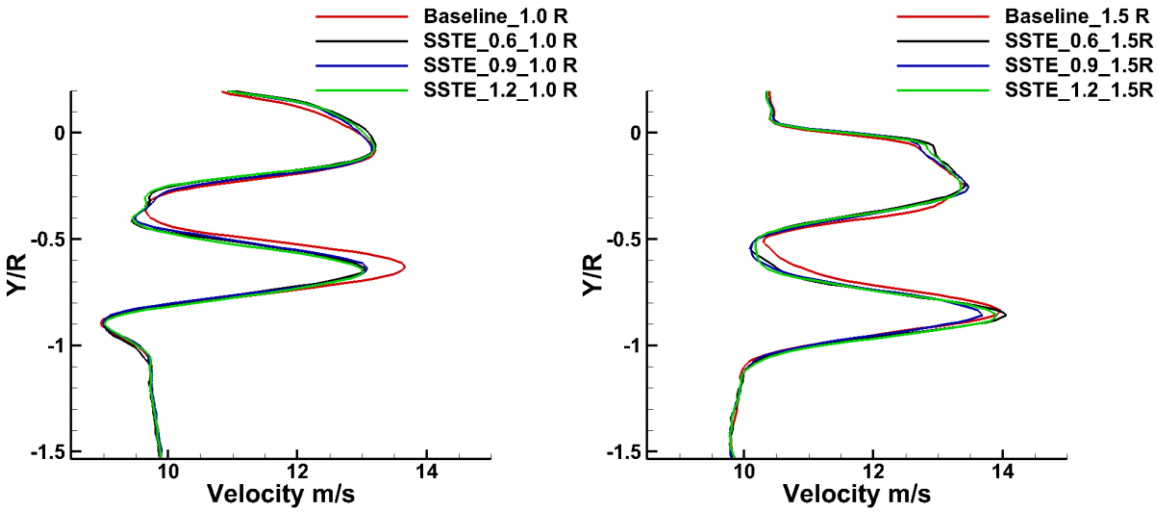

Figure 16. Velocity comparison are different downstream location in forward flight

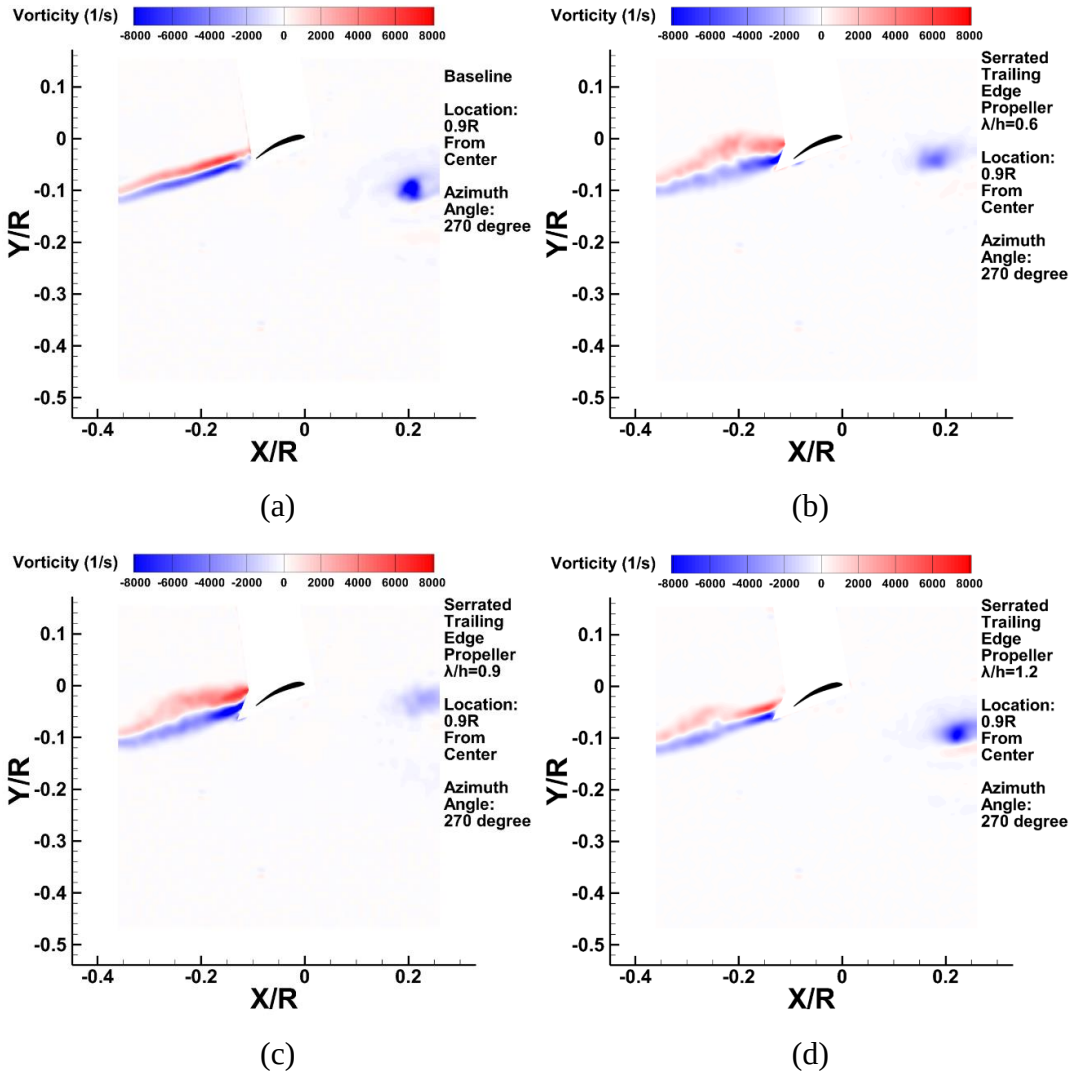

Figure 17. "Phase locked" PIV measurement results at ψ=270° at 90% radius

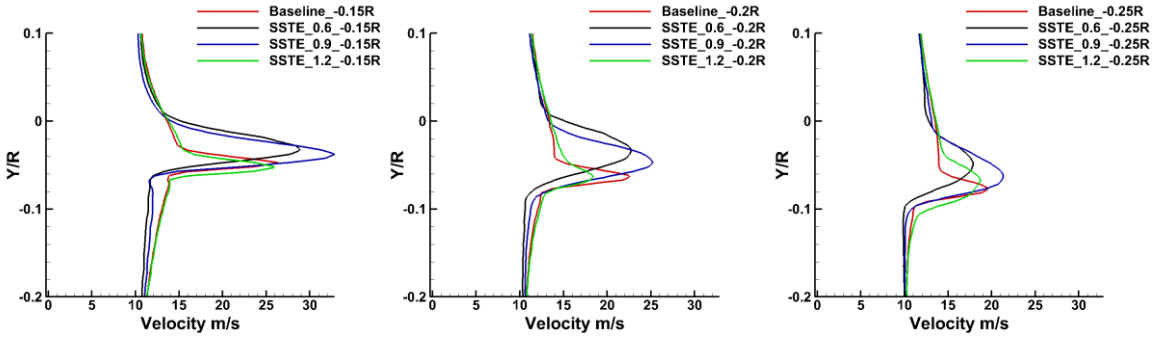

Figure 18. Velocity comparison are different downstream locations

distributions at different downstream locations (1.0R and 1.5R), a slight velocity change due to the serration could be found in figure 16. At 1.0R downstream, the three serrated trailing edge propellers had almost same profile. This indicated that the serration sizes did not affect the mean flow. The baseline propeller generated higher induced velocity from 0.4R to 0.8R compared to the serrated trailing propellers. Chord section "phase locked" PIV measurements were also conducted at 270° azimuth angle and at 90% radius from the rotating center. The vorticity distribution results of the 4 propellers at 0.9R are shown in figure 17. The blue region at 0.2R in the front of the airfoil is the tip vortex generated from another blade. The tip vorticy dissapation speed of the SSTE propellers is faster compared to the baseline propeller. The vorticies due to the flow passing trailing can be clearly viewed downstream of the airfoil. Due to the serration, the wake region increases significantly, which has been obseved by Finez[16], Gruber[8,9], and Moreau[13] in their 2D airfoil measurements. One interesting phenomenon is the wake geometry of the serrated trailing edge propeller with λ/h of 1.2. It started with a similar wake size as the baseline propeller. A short time later, the wake size increased significantly. The other two serrated trailing edge propellers showed the large wake size start directly from the trailing edge. Figure 18 shows the velocity distribution comparison results of the 4 propellers at the three different downstream locations of the trailing edge. The propellers with serration sizes of λ/h equal to 0.6 and 0.9 had a large wake region compared to baseline propeller. The serrated trailing edge propeller with a λ/h of 1.2 had a similar wake size to the baseline propeller at -0.15R downstream. This phenomenon was also observed by Moreau[13]. In his research, the plate with narrow serration generated a large wake size, and the plate with wide serrations generated a similar wake to reference plate. As the flow traveled to the downstream, the decrease of the wake velocity and the

increase of the wake region can be clearly visualized for the SSTE propeller with λ/h of 1.2. Probably, the best serration size is the one that does not increase the wake size significantly, but instead increases the turbulent mixing.

3.5 Conclusion

An experimental study has been conducted to examine the effects of the serrated trailing edges on the aerodynamic and aeroacoustic performance of the small UAS propellers, operated under hover-flight conditions. The sound pressure level spectrum measurement results indicated that the saw-tooth serrated trailing edge restrict the total noise emission by decreasing the noise level at high frequencies and maintaining the noise level at low frequencies. It was found that larger serrations resulted in better noise attenuation effects compared to the smaller serration. The comparison results of the force measurements between baseline and serrated trailing edge propellers proved that the saw-tooth serration had no significant effect on the thrust generation. The flow-filed measurement results revealed that the serrated trailing propellers generated almost identical mean flows at hover-flight conditions when compared to the baseline propeller. However, the serrations did significantly influence the flow passing over the trailing edge.

References

1 Floreano, D., and Wood, R., “Science,technology and the future of small autonomous drones,” *Nature,* vol. 521(7553), 2015, pp. 460–466.

2 Hoffmann, G., Huang, H., Waslander, S., and Tomlin, C., “Quadrotor Helicopter Flight Dynamics and Control: Theory and Experiment,” *AIAA Guidance, Navigation and Control Conference and Exhibit,* 2007.

3 Ditmer, M., Vincent, J., Werden, L., Tanner, J., Laske, T., Iaizzo, P., Garshelis, D.,

and Fieberg, J., “Bears Show a Physiological but Limited Behavioral Response to Unmanned Aerial Vehicles,” *Current Biology*, vol. 25, Aug. 2015, pp. 2278–2283.

[4] Intaratep, N., Alexander, W. N., Devenport, W. J., Grace, S. M., and Dropkin, A., “Experimental Study of Quadcopter Acoustics and Performance at Static Thrust Conditions,” *22nd AIAA/CEAS Aeroacoustics Conference*, 2016, pp. 1–14.

[5] Leslie, A., Wong, K. C., and Auld, D., “Broadband noise reduction on a mini-UAV Propeller,” *29th AIAA Aeroacoustics Conference*, 2008, pp. 5–7.

[6] Sinibaldi, G., and Marino, L., “Experimental analysis on the noise of propellers for small UAV,” *Applied Acoustics*, vol. 74, Jan. 2013, pp. 79–88.

[7] Brooks, T. F., Pope, S., and Marcolini, M. A., “Airfoil Self-Noise and Prediction,” *NASA Reference Publication 1218*, 1989, pp. 1–142.

[8] Gruber, M., Joseph, P. F., and Chong, T. P., “Experimental investigation of airfoil self noise and turbulent wake reduction by the use of trailing edge serrations,” 2010.

[9] Gruber, M., Joseph, P., and Chong, T., “On the mechanisms of serrated airfoil trailing edge noise reduction,” *17th AIAA/CEAS Aeroacoustics Conference (32nd AIAA Aeroacoustics Conference)*, 2011.

[10] Herr, M., and Dobrzynski, W., “Experimental Investigations in Low-Noise Trailing-Edge Design,” *AIAA JOURNAL*, vol. 43, 2005.

[11] Howe, M. S., “AERODYNAMIC NOISE OF A SERRATED TRAILING EDGE,” *Journal of Fluids and Structures*, vol. 5, 1991, pp. 33–45.

[12] Howe, M. S., “A review of the theory of trailing edge noise,” *Journal of Sound and Vibration*, vol. 61, Dec. 1978, pp. 437–465.

[13] Moreau, D. J., and Doolan, C. J., “Noise-Reduction Mechanism of a Flat-Plate Serrated Trailing Edge,” *AIAA Journal*, vol. 51, Oct. 2013, pp. 2513–2522.

[14] Oerlemans, S., Fisher, M., Maeder, T., and K?gler, K., “Reduction of Wind Turbine Noise Using Optimized Airfoils and Trailing-Edge Serrations,” *AIAA Journal*, vol. 47, Jun. 2009, pp. 1470–1481.

[15] Chong, T. P., Joseph, P., Vathylakis, A., and Gruber, M., “On the Noise and Wake flow of an Airfoil with Broken and Serrated Trailing Edges,” *17th AIAA/CEAS Aeroacoustics Conference (32nd AIAA Aeroacoustics Conference)*, 2011.

[16] Finez, A., Jacob, M., Roger, M., and Jondeau, E., “Broadband Noise Reduction Of Linear Cascades With Trailing Edge Serrations,” *17th AIAA/CEAS Aeroacoustics Conference (32nd AIAA Aeroacoustics Conference)*, 2011.

[17] Geyer, T., Sarradj, E., and Fritzsche, C., “Measurement of the noise generation at the trailing edge of porous airfoils,” *Experiments in Fluids*, vol. 48, 2010, pp. 291–308.

[18] Eppler, R., *Airfoil design and data*, Springer Berlin Heidelberg, 1990.

[19] Leishman, J. G., *Principles of helicopter aerodynamics*, Cambridge University Press, 2006.

[20] Arce Leon, C., Ragni, D., Prbsting, S., Scarano, F., and Madsen, J., “Flow topology and acoustic emissions of trailing edge serrations at incidence,” *Experiments in Fluids*, vol. 57, May 2016, p. 91.

CHAPTER 4

EXPERIMENTAL INVESTIGATION ON THE AERODYNAMIC AND AEROACOUSTIC CHARACTERISTICS OF A BIO_INSPIRED SMALL UNMANNED AERIAL SYSTEM PROPELLER

Zhe Ning and Hui Hu

Department of Aerospace Engineering, Iowa State University, Ames, Iowa, 50011

Abstract

Under rapid development, the small UAV is facing two essential problems: aerodynamics efficiency and noise emission. In this work, the aerodynamic and aeroacoustics characteristics of a novel bio-inspired UAV propeller with the unique planform shape inspired by the cicada wing and maple seed was experimentally investigated by comparing with conventional baseline propeller at hover flight condition. The design thrust (3N) and solidity (0.12) are kept same for both propellers. The aerodynamics forces and sound measurements revealed that, compared with baseline propeller, the bio-inspired propeller could generate equal thrust and emit lower noise under constant power input. In addition, the flow field measurements obtained from Partial Image Velocimetry (PIV) illustrated that the bio-inspired propeller produced a smaller wake region and demonstrated a fast decay rate of tip vortex strength compare to baseline propeller.

4.1 Introduction

In the past twenty years, the Unmanned Aerial Vehicle (UAV) has developed rapidly due to the reduction of the sizes and costs of small electronic devices, such as processors, sensors,

and batteries[1]. Specifically, the rotary-wing system has become a popular configuration due to its hovering ability and vertical take-off and landing (VTOL) motion [2]. Fitted with these attributes, the rotary-wing UAV has been put to use in a variety of applications (e.g., video taking & mapping, building &construction, delivery, rescue operation, and personal entertainment).

During the last two decades, the development of the rotary-wing UAV was focused on control theory and functional development. In a study performed by Achtelik[3], the flying motion of a quadcopter was controlled by visual feedback and sensor measurements to accomplish autonomous flight. Mellinger[4] studied real-time trajectories and controllers to drive a quadcopter to execute aggressive maneuvers. Lindsey[5] used teams of quadcopters to construct buildings, and Mirjan[6] used flying robots to build a bridge. Although the control theory and application has been well developed, less emphasis has been placed on the aerodynamic performance. Currently, the operational time of rotary-wing small UAV is lower than one hour, which is too short for many applications, such as delivery, inspection, and recording video. Therefore, the aerodynamic efficiency, especially the propeller efficiency, is an essential consideration for the design progress providing the known constraints of the battery charge and motor power. The numerical work done by Bristeau[7] illustrated that the flexibility of the propellers has significant effect on the quadcopter dynamic performance, under the assumption of constant local angle of attack (AOA) and induced velocity. Since the rotary-wing UAV always consists of multiple rotors, with small separation distances between rotors, numerical analyses have proved that the strong flow interaction will result in up to 5% thrust decrease[8]. During flight, the rotor will be affected by tip vortices generated from the rotor itself, as well as neighboring rotors[9]. For current small UAV propellers, a larger gap between rotors must be maintained in order to make up the thrust deficit due to the flow interaction. In other words, the size of the rotary-wing UAV will increase. A

significant result is that the bending strength at the joint between arm and fuselage will increase. Furthermore, the weight of the UAV will slightly increase, which may balance out or reduce the total efficiency. Besides the aerodynamic constraints, the noise generated from the operating rotary-wing UAV is another essential problem, which will have significant impact on human health, as well as wild animals. In a study executed by Ditmer[10], the noise generated from a UAV increases the heart rates of bears, which indicates raised levels of stress. According to Leslie[11] and Sinibaldi[12], noise reduction of UAVs could broaden their mission ranges. Therefore, the noise generated from rotating propeller need to be considered during the design process.

Understanding that the propeller is the main component of lift generation and aerodynamic noise, the focus of this study is to design a UAV propeller with the same power input that can achieve the same or improved aerodynamic performance, while reducing noise levels. In determining a potential solution, nature always provides inspiration to researchers and engineers. As shown in Figure 1, cicada wings and maple seeds have their planform different from traditional propellers. Instead of having a tapered planform shape, they have large chord length in the mid-span region. Most of the thrust for a rotary wing is known to be generated between the 50% to 90% radius, as shown in Figure 2. The planform of insect wings and maple seeds seems to have a better match with the lift distribution, where the chord length is large at high lift region. Beside the geometry, another important factor is the Reynolds number. At Reynolds numbers ranging from 10,000 to 100,000, the lift/drag ratio dramatically increases as the Reynolds number increases. As shown in figure 3, the lift/drag ratio at a Reynolds number of 100,000 is almost twice that of when the Reynolds number is 50,000 for the same E63 airfoil (a typical low Reynolds number airfoil)[13]. The increasing chord length will increase the chord

Reynolds number. As a result, the propeller will operate in the regime with a better lift/drag ratio if this configuration of planform is used into design.

With this in mind, we conducted an explorative study to evaluate the aerodynamic and aeroacoustic performances of a novel bio-inspired UAV propeller with the unique planform shape inspired by the cicada wings and maple seeds. The bio-inspired UAV propeller was designed to have the same planform area and the same airfoil cross sectional shape, thus yielding the same weight as a conventional tapered UAV propeller. It was expected that the bio-inspired UAV propeller will have comparable or even better aerodynamic and aeroacoustic performances in comparison to the conventional tapered UAV propellers. In the present study, a conventional tapered UAV propeller was used as the baseline for the comparative study, and the aerodynamic forces generated by the bio-inspired UAV propeller under hovering conditions will be measured quantitatively by using a high-sensitive force/moment transducer (JR3 load cell). The aeroacoustic performance of the bio-inspired propeller was characterized in an anechoic chamber. Furthermore, a high-resolution digital Particle Image Velocimetry (PIV) system was also used to achieve detailed flow field measurements to quantify the evolution of the unsteady vortex structures in the wake of the propellers. The aerodynamic force and aeroacoustic measurement results were correlated to the detailed flow field measurements in order to elucidate the underlying physics.

Figure 1. Wing planform of cicada and maple seed

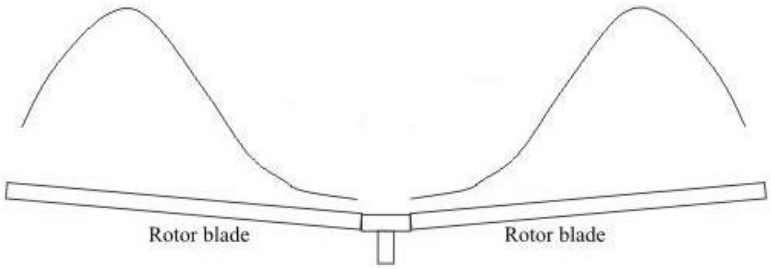

Figure 2. Aerodynamic force distribution of a rotor.

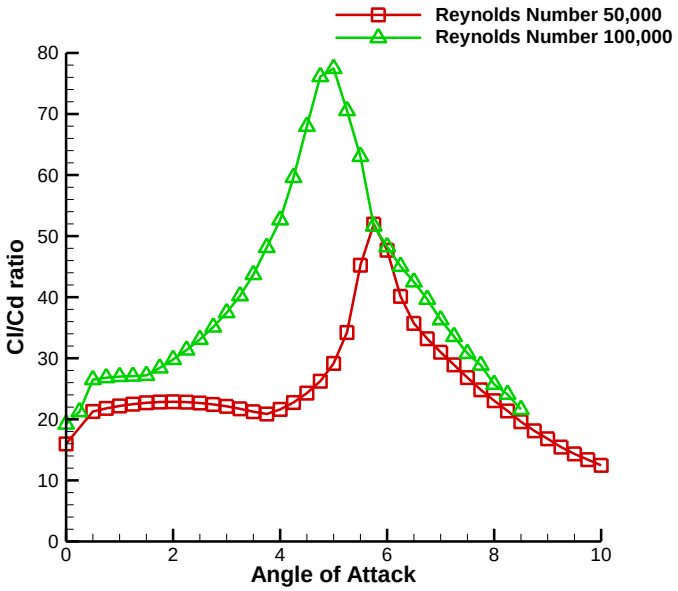

Figure 3. life/drag ratio of a low-Reynolds E63 airfoil vs AOA at Re=50,000 & Re=100,000

4.2 Propeller design and experimental setup

4.2.1 Propeller design

As shown in figure 4, in order to accomplish a designed thrust of 3N, an E63 airfoil shape was used to design the baseline propeller. The thickness of the airfoil was doubled based on the camber line due to a strength concern. The propeller was 240mm in diameter and 11mm at the chord tip. The chord lengths along the propeller radius from tip to 30% radius were calculated

by the equation $C_r = \frac{C_{tip}}{r}$. where C_r is the chord length at corresponding radius location, and r represents a non-dimensional radial distance, which is 0 in the rotating center and 1 at tip. The blade twisted 11.6 degrees at the tip to 26.3 degrees at the 30% radius. The solidity was 0.12 which is widely used for conventional propeller. As shown in figure 5, the airfoil shape, designed thrust and rotational speed, and solidity used to design the bio-inspired propeller were kept the same as the baseline propeller design. This is with the notable exception of the design of the propeller planform, which was derived from a real maple seed configuration with a reduced aspect ratio. Both propellers were made of a hard plastic material (i.e., VeroWhitePlus, RGD835, manufactured by Stratasys, Inc.) by using a rapid prototyping machine (i.e., Connex 3D printer).

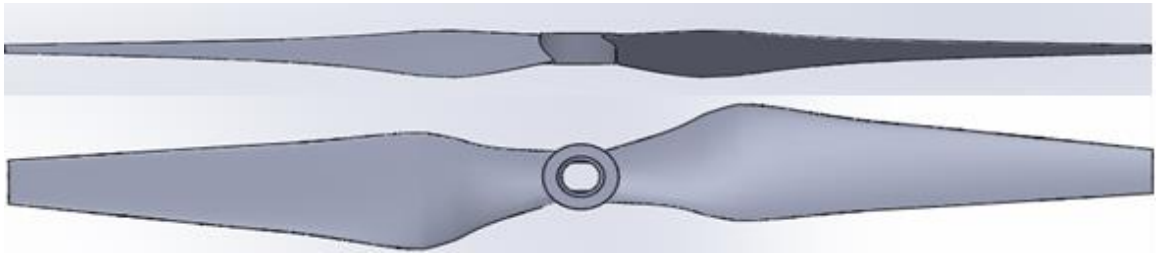

Figure 4. Baseline propeller

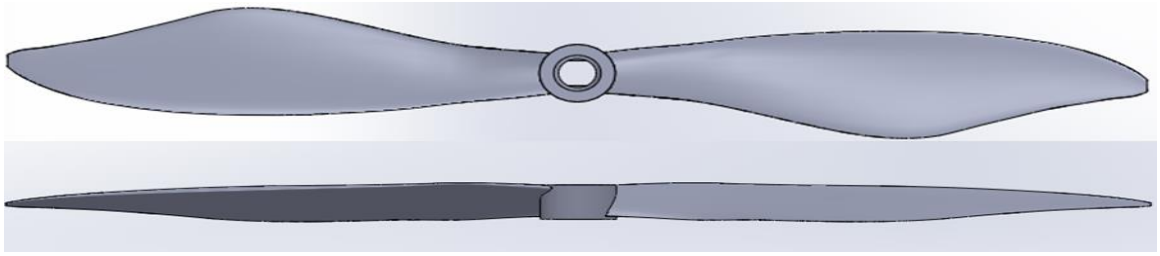

Figure 5. Bio-inspired propeller

4.2.2 Experimental setup

The noise at the hover flight condition was measured in an anechoic chamber (as shown in Figure 6 (a)) located in the Department of Aerospace Engineering at Iowa State University. The chamber has dimensions of 12*12*9 feet with a 100 Hz cut-off frequency. Figure 6 (b)

shows the sketch of the sound measurement. The red arrow represents the induced airflow direction, and the blue points represent the test locations. The spectrum measurement was conducted at 0 degrees and 5D away from the propellers. In the near field, closer than 5D, the turbulence level is high, which would affect the sound measurement. 5D is the standard distance that can be considered a far field distance.

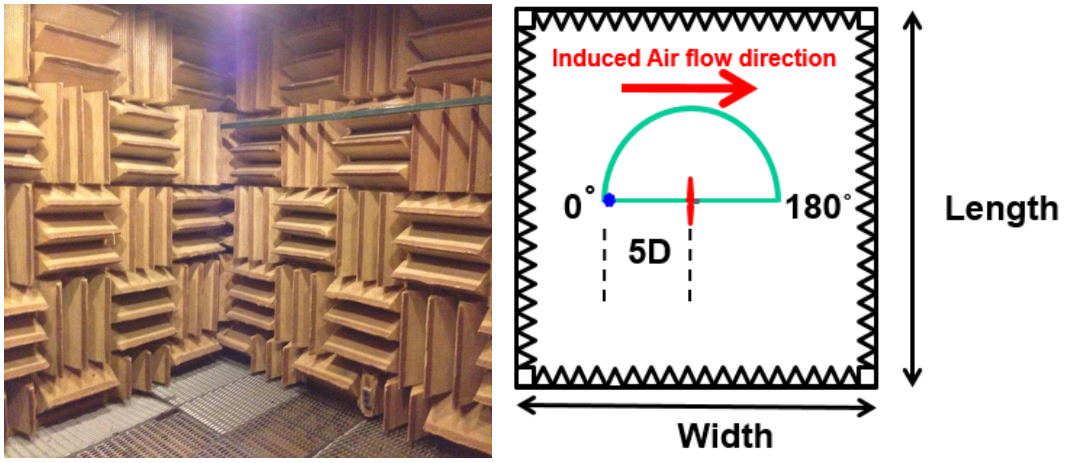

(a) (b)

Figure 6. Anechoic chamber and sound measurement sketch

Table1. Test conditions

Blade type	Rotational direction	Voltage Condition (V)	Rotational speed (RPM)
Baseline propeller	CCW (Counter Clock-wise)	11.1	0-6000
Bio-inspired propeller	CCW (Counter Clock-wise)	11.1	0-6000

Figure 7 shows the schematic of the experimental setup to be used in the present study to measure the dynamic force of the both propellers. A 0.2 diameter clearance gap was maintained between propeller and support tower. The power used to drive the motor was tabulated by a

direct current power supply. The UAV propeller was connected to a function generator via an electronic speed control. The rotational speed of the propeller was controlled by adjusting the duty cycle of the output signal from the function generator. During the experiment test, the rotational speed of the propeller was measured by tachometer. A high-sensitivity force-moment sensor (JR3 load cell) was used to measure the force and moment, and the precision of this sensor for force measurements was ±0.1N (± 0.25% of the full range). Different types of propellers (baseline & Bio-inspired) were tested under the conditions shown in Table 1.

In addition to the aerodynamic force measurements, a high-resolution digital PIV system was used to measure the flow field in order to quantify the detailed flow structures around the propeller. An interrogation window with 32×32 pixels and a 50% effective overlap were used to calculate the instantaneous velocity vectors. In order to determine the ensemble-average wake flow statistics and detailed flow structure at certain phase angles, both “free-run” and “phase-locked” PIV measurements were conducted in this study. The ensemble-average results were obtained from 1000 frames of instantaneous PIV measurements for free-run test. For the “phase-locked” PIV measurements, the phase-averaged flow velocity at certain phase angle range from 0 to 330 degrees subdivided into 30-degree increments were calculated from 255 frames of the instantaneous PIV measurements. Figure 8 shows the schematic of the PIV system used in this study. The air was seeded with ~1μm water based droplets by using fog generation. The field illumination was provided by a Nd;YAG laser generator with power 200 mJ per pulse at the wavelength of 532 nm. The laser sheet thickness was set to around 1 mm at test section. A high-resolution (2048 x 2048 pixels) charge-coupled device (CCD) camera with axis perpendicular to the laser sheet was used to capture the raw image. The camera and laser generator were connected to the computer via a digital delay generator, which controlled the timing of the image

capture and laser illumination. A second digital delay generator was used to modify the signal, in order to achieve the “phase-locked” PIV measurement.

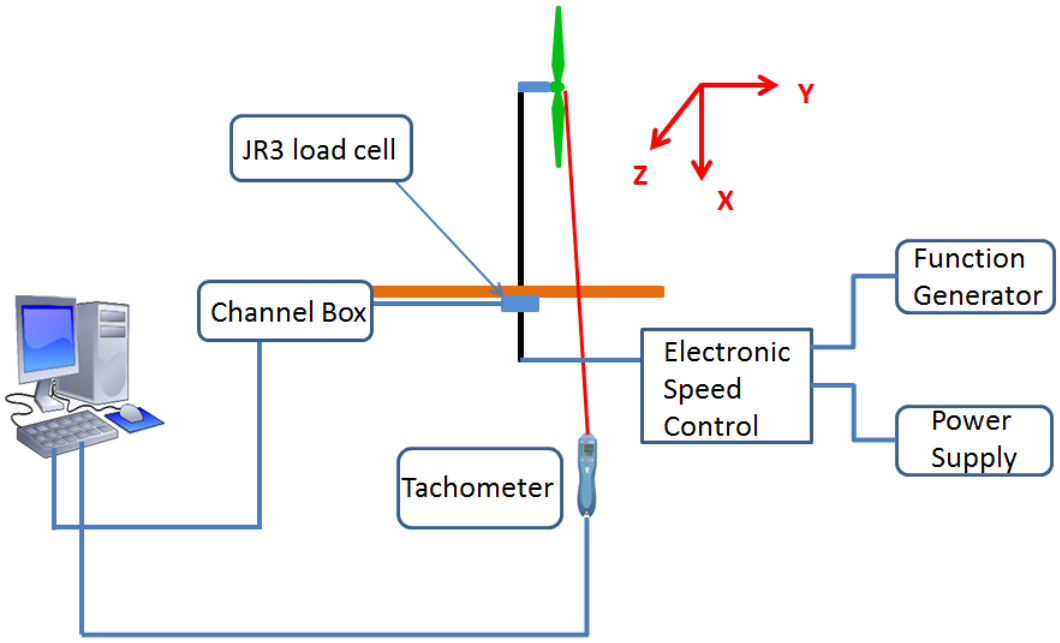

Figure 7. Experimental setup for the dynamic measurements of propeller

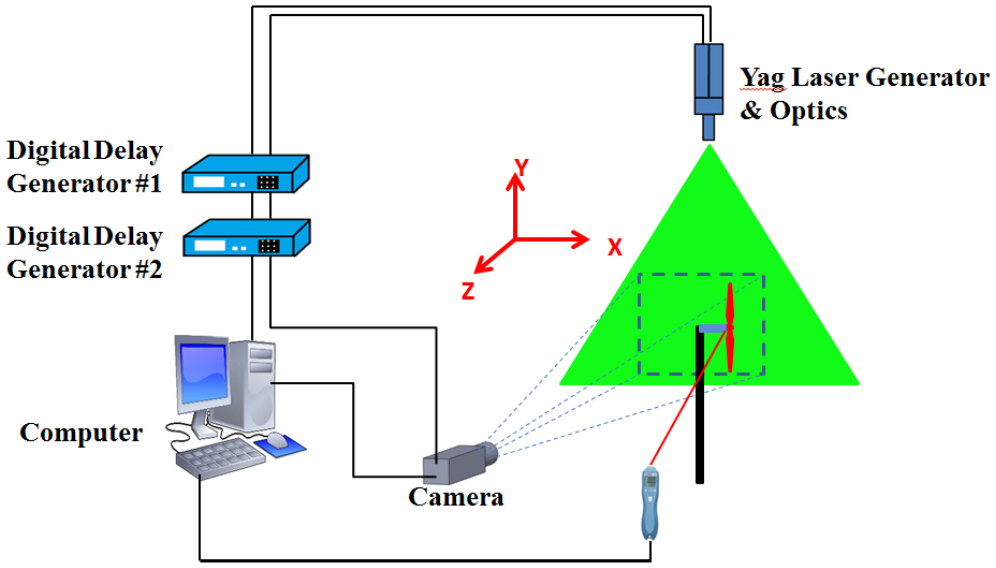

Figure 8. Experimental setup for the flow field measurement

4.3 Results and discussion

4.3.1 Aerodynamics performance results

The aerodynamic force measurements were conducted at different rotational speeds ranging from 0 to 6000 RPM for both propellers. Figure 9 presents the comparative results, where the design thrust is denoted by dashed line, and the results of baseline and bio-inspired are shown in red and black lines, respectively. This color line notation is also used in later comparisons. The symbols indicate the experimental data, and the lines are the best curve fits. Each data point is the average value of 30 second measurement with 1000Hz sampling frequency. In figure 9 (a), it should be noted that the thrust grows with the input power increasing. Compared with the baseline propeller, the bio-inspired propeller required same power to generate the design thrust. However, the rotational speed of the bio-inspired propeller was 3.5Hz lower than the baseline propeller at hover motion (thrust = 3N). This indicates that the thrust coefficient of bio-inspired propeller is higher than the baseline propeller. The thrust coefficient is defined by

$$C_T = \frac{T}{\rho A V_{tip}^2} \tag{1}$$

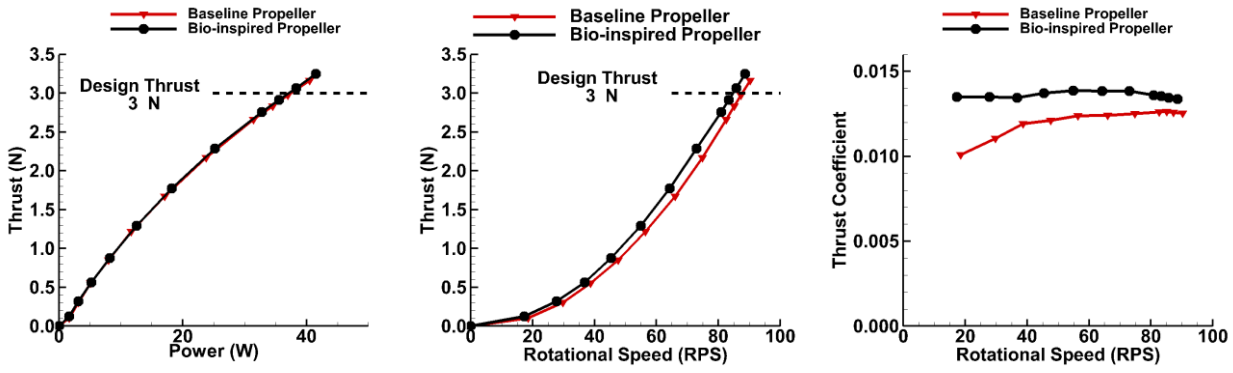

(a) (b) (c)

Figure 9. Force measurement results of baseline and bio-inspired propellers

It can be found in figure 9 (c), the thrust coefficient of bio-inspired propeller is about 10% higher than the baseline propeller.

4.3.2 Sound measurement results

As mentioned before, the sound measurements were conducted at hover motion, thus the thrust was kept constant (3N) for both propellers. Hover is unique flight condition for vertical take-off and landing aircraft, where the thrust generated from propeller equal to the aircraft weight. At this flight condition, the forward and vertical flight speed is zero. The experimental conditions at hover are listed in table 2. The aeroacoustic performance was characterized by sound pressure level (SPL) at different frequency, which calculated by

$$SPL\ (dB) = 20\ log_{10}\left(\frac{p}{p_{ref}}\right)(dB) \tag{2}$$

The reference pressure is 2×10^{-5} Pa. Compared with baseline propeller, the bio-inspired propeller could reduce noise up to 4 dB in the human hearing domain (20Hz~20,000Hz). As shown in figure 9 (a), the bio-inspired propeller generates lower SPL than the baseline propeller, which means it has the potential to reduce tonal noise as well as broadband noise. Figure 9 (b) reveals the sound spectra comparison results at the low frequency domain. The frequency axial is non-dimensionalized by blade passing frequency (BPF), which is defined by

$$BPF = rotational\ frequency \times blade\ number \tag{3}$$

All of the peak values shown in spectra are the tonal noise components, which are associated with BPF. The tonal noise consists of loading noise and thickness noise. The loading noise is generated from the force variation and the thickness noise comes from mass variation, which has

Table 2. Flight condition at hover motion

	Rotational speed (RPS)	Mean Thrust (N)	Thrust standard deviation (N)
Baseline propeller	86.5	3	0.278
Bio-inspired propeller	83	3	0.211

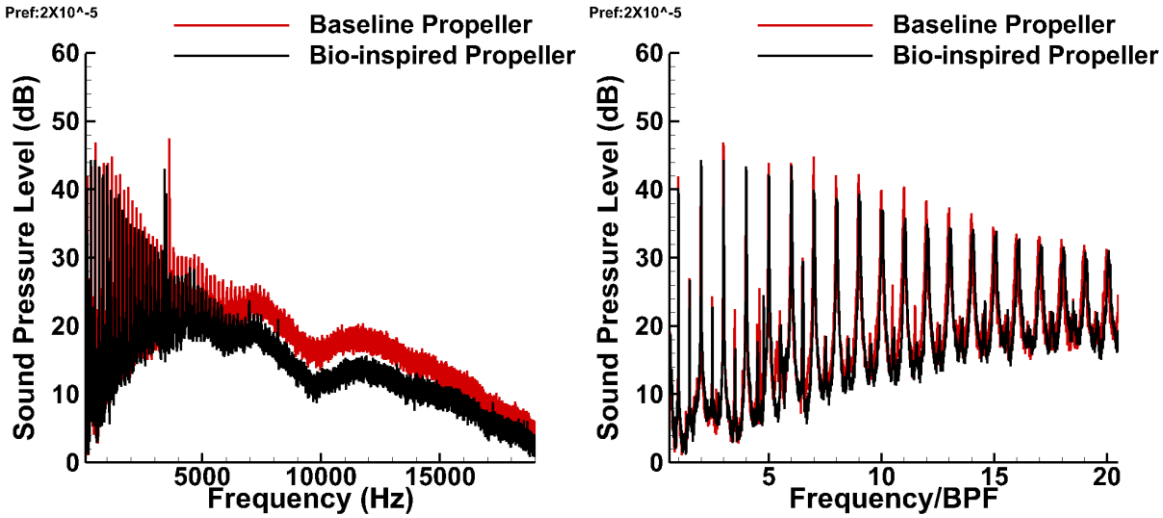

(a) (b)

Figure 11. Sound spectra comparison between the baseline propeller and bio-inspired propeller

been illustrated in terms 1 and 2 on right hand side of Lighthill's acoustic analogy equation

$$\left(\frac{\partial^2}{\partial t^2} - C_0^2 \frac{\partial^2}{\partial x_i^2}\right)\rho = \frac{\partial m}{\partial t} - \frac{\partial f_i}{\partial x_i} + \frac{\partial^2 T_{ij}}{\partial x_i \partial x_j} \tag{4}$$

At Mach number lower than 1, the loading noise dominates the tonal noise. Compared with baseline propeller, the reduction of the tonal noise of the bio-inspired propeller could be easily observed. This noise attenuation could be attributed to the small force variation of the bio-inspired propeller. As shown in table 2, the thrust standard deviation of the bio-inspired propeller is 24% lower than the baseline propeller. Another possible reason is the lower rotational speed.

By applying the free-space Green's function to equation 3, and do a scale analysis, it was found that the thickness noise is proportional to the U^2, the loading noise is proportional to the U^3, and the noise due to Lighthill's stress tensor is proportional to the U^4. Here, the U is the flow velocity. At hover motion, the rotational speed of bio-inspired propeller is low, which benefits the noise reduction.

4.3.3 "Free-run" PIV measurement results

In addition to the force and sound measurements, the flow field measurements downstream of the propellers were achieved through a high-resolution PIV system. Akin to the sound measurements, the flow structure measurements were also conducted at hover motion, where the flow field is azimuthally axisymmetric. The ensemble-averaged velocity distribution results of a typical "free-run" PIV measurement of both the baseline and bio-inspired propellers are shown in figure 12. The term "free-run" means the images taken were not harmonic with the propeller rotation. The X and Y axes were normalized based on the propeller radius (120mm). The induced airflow direction is denoted by the red arrow. The large blue region is the quiescent flow region, where the flow velocity is low. It indicates the rotating propeller did not affect this area significantly. The region above propeller is the inflow region. Due to the propeller rotation, the flow was sucked into the rotating plane. Another region is the induced flow region, also known as slipstream[14]. At there, the velocity is higher compared to other two regions. This is due to the propeller pushing the air. The pressure difference between inflow and induced flow region resulted in a thrust generated from propeller. The black lines shown in the plot are the streamlines. The densely streamlined area is the flow boundary between quiescent and induced flow region.

Compared with the baseline propeller, the flow speeds at quiescent and inflow region of bio-inspired propeller were almost the same. However, the velocity distribution of these two propellers were different at the induced flow region. The bio-inspired propeller had larger velocity gradient from flow boundary towards rotating axis compared with baseline propeller. Figure 13 shows the velocity profile at different downstream locations (0.166R, 0.5R, and 1R). The induced flow velocities downstream were almost same from tip to 0.75R for both propellers. Compared with baseline propeller, the bio-inspired propeller generated higher induced flow velocity in the region between 0.5R and 0.75R, where it has larger chord length. Meanwhile, the induced velocity of the bio-inspired propeller was lower than baseline propeller from center to 0.5R. Although the velocity distributions are different, the mass flow rate of both propellers were same, which are confirmed by the force measurement results. Based on the rotational speeds and chord lengths at different span-wise locations of both propellers, the chord Reynolds number distributions along the blade could be obtained. As shown in figure 15 (a), the bio-inspired propeller operated at higher AOA from 0.4R to 0.9 R compare to baseline propeller, which is mainly due to the large chord length at these locations. Because of the small chord length at the tip, the bio-inspired propeller operated at a lower AOA compare to baseline propeller. With the induced velocities provided by PIV measurements and the rotational speeds at hover motion, the operating AOA at different span-wise locations could be calculated. It was discovered in figure 15 (b) that the bio-inspired propeller operated at almost constant AOA, which was around 6 degrees. The operating AOA of baseline model varied from 11 to 4 degrees from the root to 0.85R. For both propellers, there is a large jump from 0.85R to 0.9R, which is mainly due to the

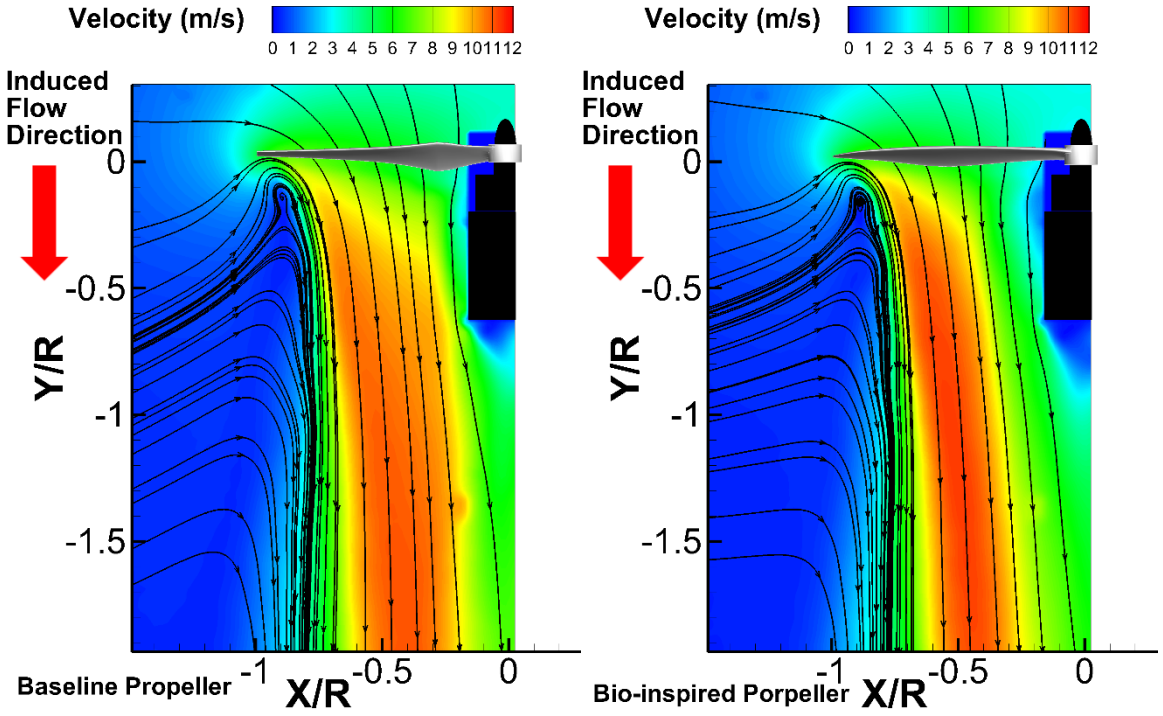

(a) (b)

Figure 12. "Free-run" PIV measurement results_ensemble-average velocity distribution

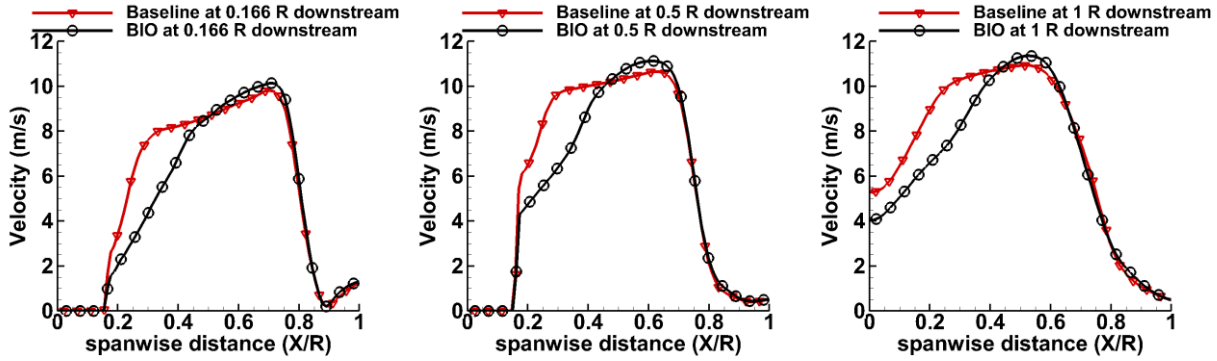

(a) (b) (c)

Figure 13. Velocity distribution comparison at different downstream location

large gradient of the induced velocity. From 0.85R to 0.9R, the induced velocities dropped from around 8.4 m/s to about 3.7 m/s for both propellers, and the rotational speed increased from 54 m/s to 60 m/s. According to blade element diagram (figure 14), the inflow angle of attack (Φ) decreased from 9 degrees to 3.5 degrees. Since the twist angle (Θ) varied smoothly, the sudden

change of the inflow AOA would lead to the operating AOA (α) jump. The U, U_P, and U_T represent the relative velocity, induced velocity, and rotational velocity, respectively.

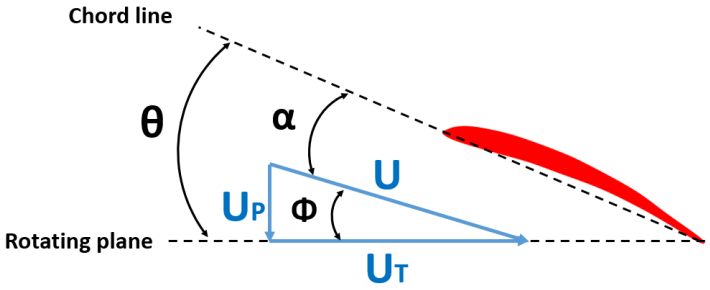

Figure 14. blade element

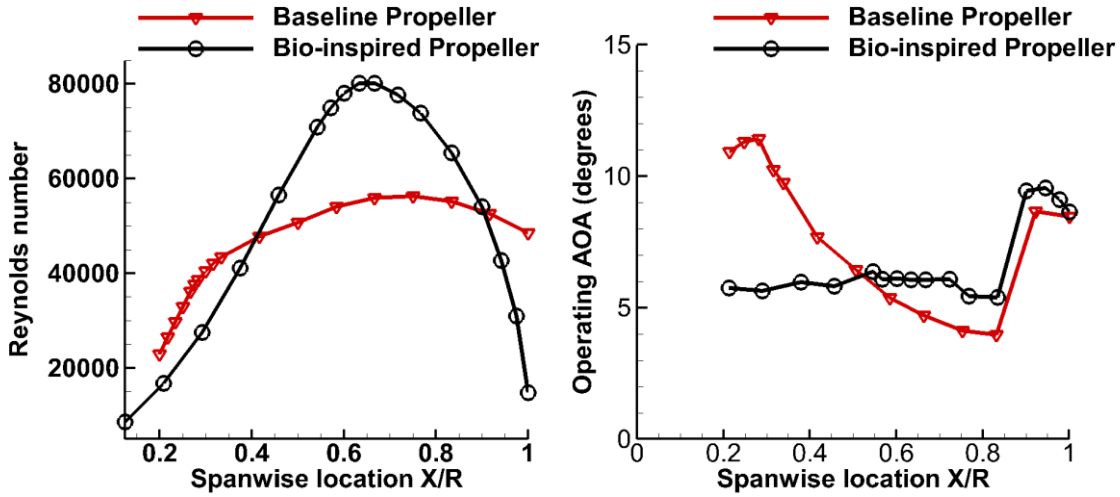

(a) Re distribution (b) AOA distribution

Figure 15. Reynolds number and operating AOA along the propellers

4.3.4 "Phase-locked" PIV measurement results

A "phase-locked" PIV measurement was also conducted at hover motion to illustrate the detailed flow characteristics of the downstream flow for the two different types of propellers. The term "phase-locked" means the images taken were harmonic with propeller rotation, so that the propeller appears in the same orientation every time an image is obtained. The phase angle

was defined as the angle between position of a pre-marked blade and the measurement plane. In this study, the phase angles ranged from 0 to 330 degrees with incremental changes of 30 degrees, which could provide detailed information of the wake generation and translation within a full cycle of propeller rotation.

Figure 16 shows the velocity distribution of the "phase-locked" PIV measurement results of the baseline propeller at 0, 60 and 120 degree phase angles. The 0 degree phase angle indicates that the propeller was just crossing the measurement plane. The three flow regions (inflow, induced flow and quiescent) can be visualized clearly in these plots, which are similar to the results achieved from the "free-run" PIV measurement. One phenomenon which was not captured by the "free-run" PIV measurements was the periodic velocity deficit close to the boundary between the induced flow and quiescent regions, which is due to the blade tip cutting flow and results in the formation of the tip vortices. Several strip shape, low-speed areas within the induced flow region also were not observed in the "free-run" PIV measurement. This phenomenon is due to

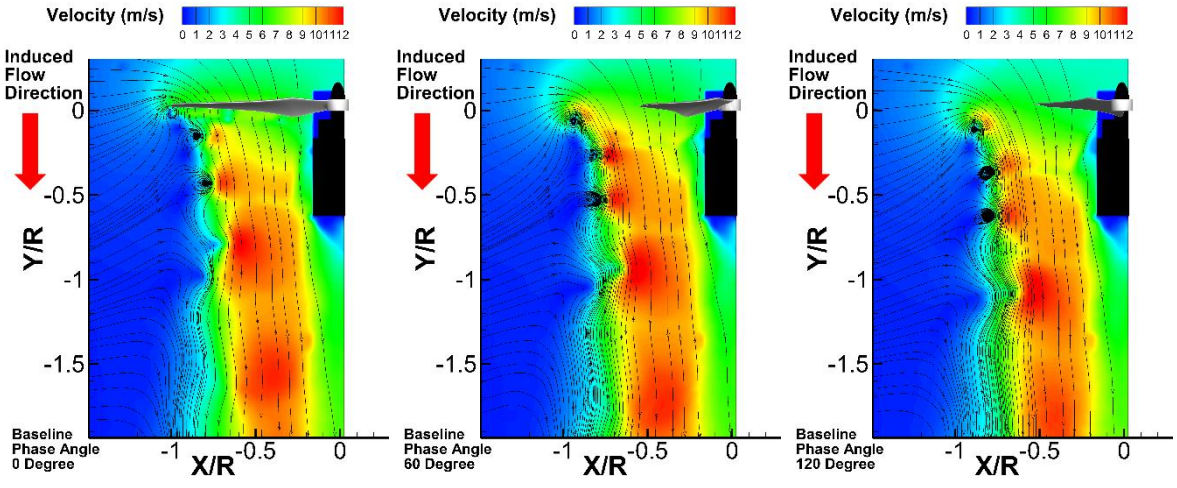

(a) (b) (c)

Figure 16. "Phase locked" PIV measurement results_velocity distribution of baseline propeller

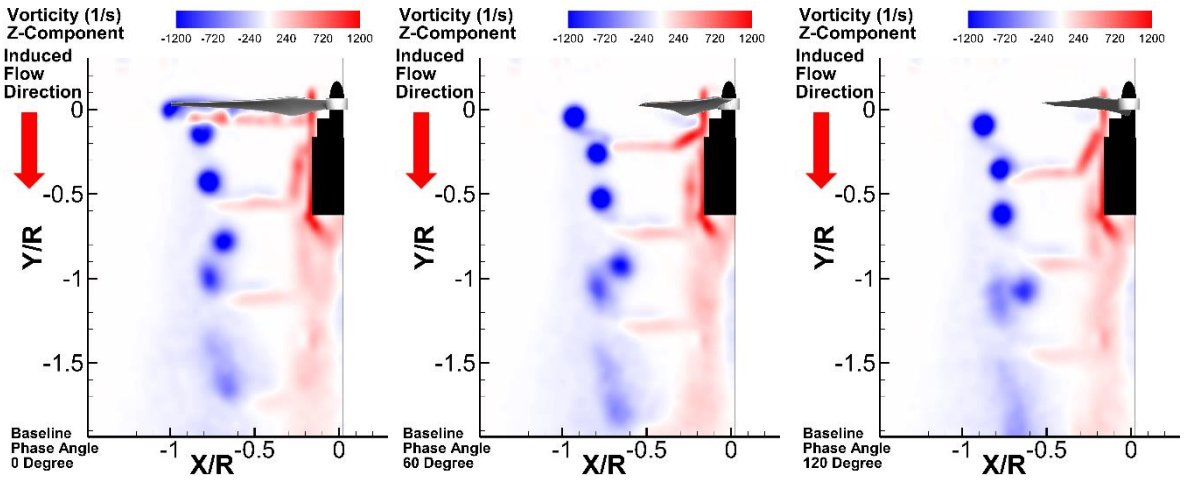

(a) (b) (c)

Figure 17. Phase locked PIV measurement results_vorticity distribution of baseline propeller

the propeller cut–in. The circular motion of the streamline represents the tip vortex structure. The vorticity distribution is displayed in figure 17. The tip vortex structure is shown clearly in figures (a) through (f). With the phase angle increasing, the tip vortex structure shrinks inward and travels towards the downstream direction. The positive and negative vorticity region located in the induced flow area is due to the flow passing the trailing edge. Due to the velocity difference, these vortices travel faster compared to tip vortices. As a result, the coming tip vortex starts to interact with the previous one at around the 70% radius downstream. This phenomenon is generally observed in rotor hover condition. Through flow visualization, Leishman[14] also observed this phenomenon in the wake of hovering helicopter blade. After the interaction, a pair of tip vortices will form one. The strength of it dropped dramatically and dissipated quickly.

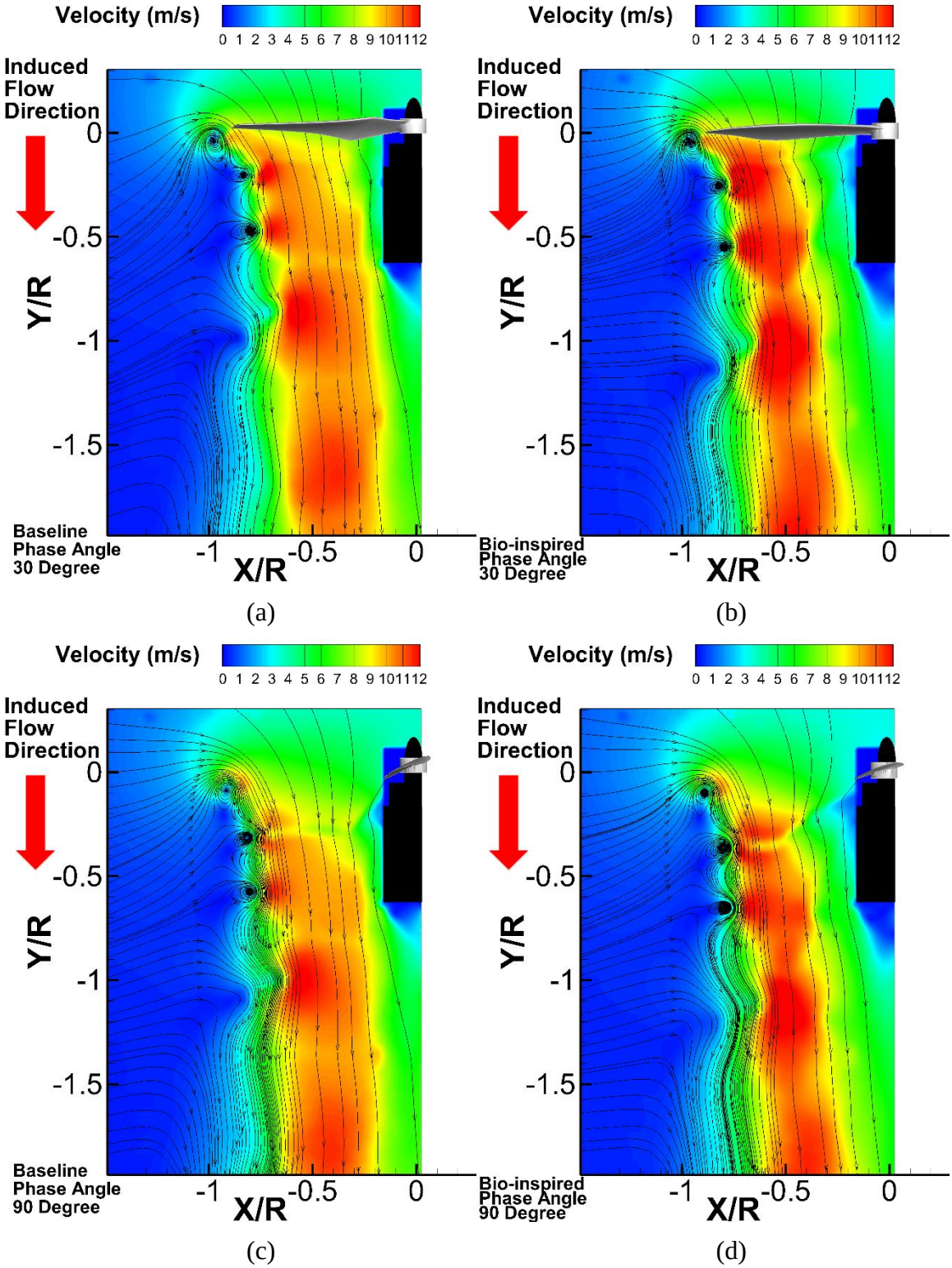

Figure 18. Velocity distribution comparison results at 30 and 90 degree phase angle

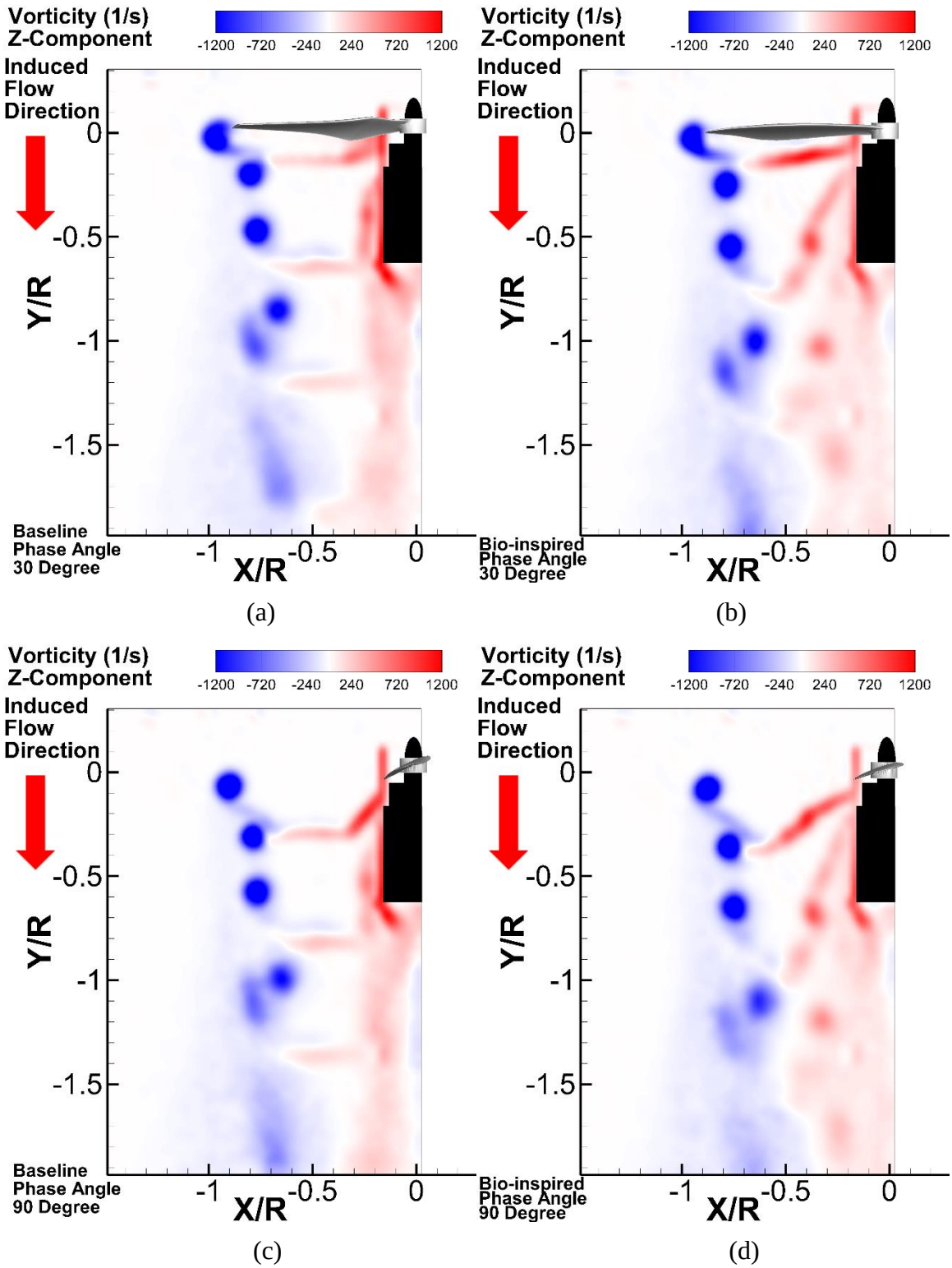

Figure 19. Vorticity distribution comparison results at 30 and 90 degree phase angle

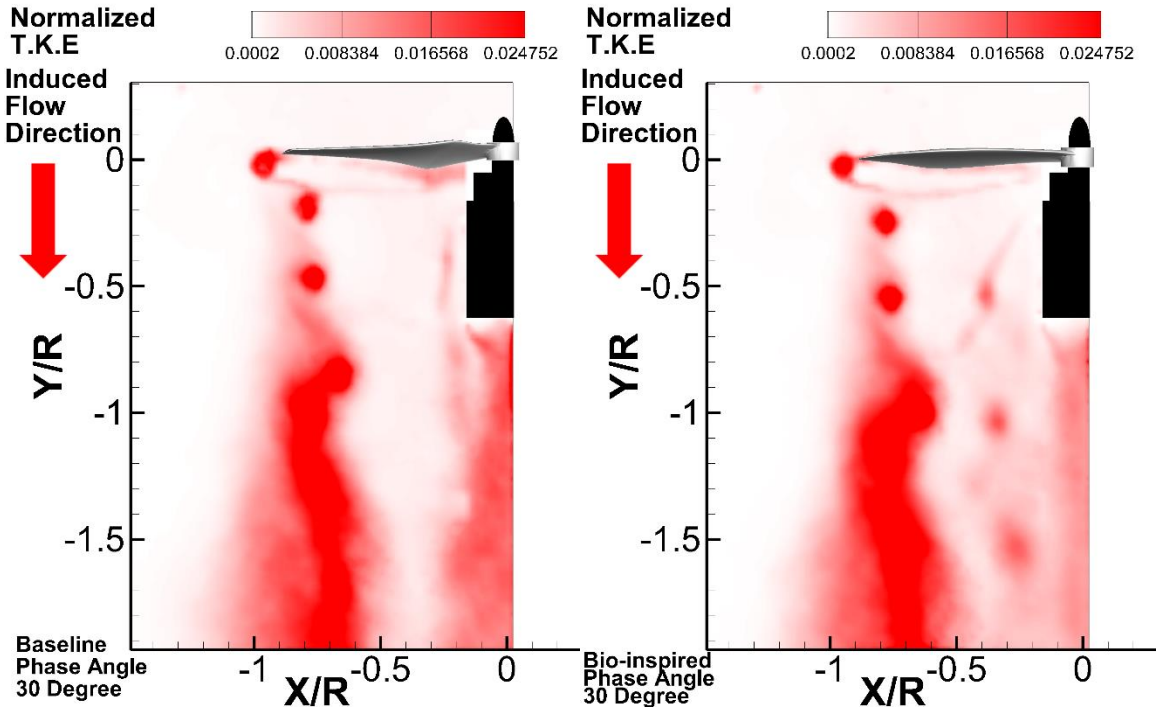

Figure 20. Normalized T.K.E distribution comparison results at 30 and 90 degree phase angle

The comparative results of the velocity distributions of baseline and bio-inspired propellers at 30 and 90 degree phase angle are shown in figure 18. Compared with the baseline propeller, the induced velocity of bio-inspired propeller was higher at the outer part of the induced flow region, and lower at the inner part. The velocity gradient from the flow boundary towards rotating axis of the bio-inspired propeller was larger than that of the baseline propeller. Figure 19 shows the comparative results of the vorticity distribution of two propellers. One significant difference between these two propellers was the shape of the vortices due to the flow passing trailing edge. As mentioned before, the velocity gradient of the baseline propeller along radial direction was small. As a result, the shape of these vortices were almost parallel to the rotating disk. However, the shape of the vortices of bio-inspired propeller tilted downward in the wake while traveling downstream. Another difference was the vorticity distribution in the

induced flow region after 0.5R downstream. The vorticity distribution of bio-inspired propeller was less organized than that of the baseline propeller. This phenomenon can be observed in figure 20, which represents the normalized turbulent kinetic energy (TKE). Here, the TKE is normalized by the average induced velocity. The high TKE level appears at the tip vortex region, and tip vortex interaction region.

4.3.5 Comparison of the characteristics of the wake flow for both propellers

The wake structure traveling speed was acquired by tracking the location of it at different wake ages. In the wake of the propellers, the translation speed of tip vortex was almost half of the tip of the shear layer. This is clearly shown in Figure 21 for both propellers. As mentioned before, this is the reason for the tip vortex interaction in the downstream. By tracking the center of the tip vortex at different wake age, the flow boundary could be acquired. It can be seen in figure 22 (a), the wake size of the bio-inspired propeller is smaller compared with the baseline model's. The tip vortex interaction happened at an earlier stage compared bio-inspired propeller to the baseline propeller. The tip vortex interaction of the bio-inspired propeller appeared at around a 700-degree wake age, and this phenomenon appeared at about an 800-degree wake age for baseline propeller. The figure 22 (b) reveals this comparison of the tip vortex strengths. At early wake age, two propeller had similar strength. After 500 degrees, the vorticity value of the tip vortices was lower for the bio-inspired propeller, as compared with the baseline propeller. This indicates the tip vortices decay rate of the bio-inspired propeller was faster than baseline.

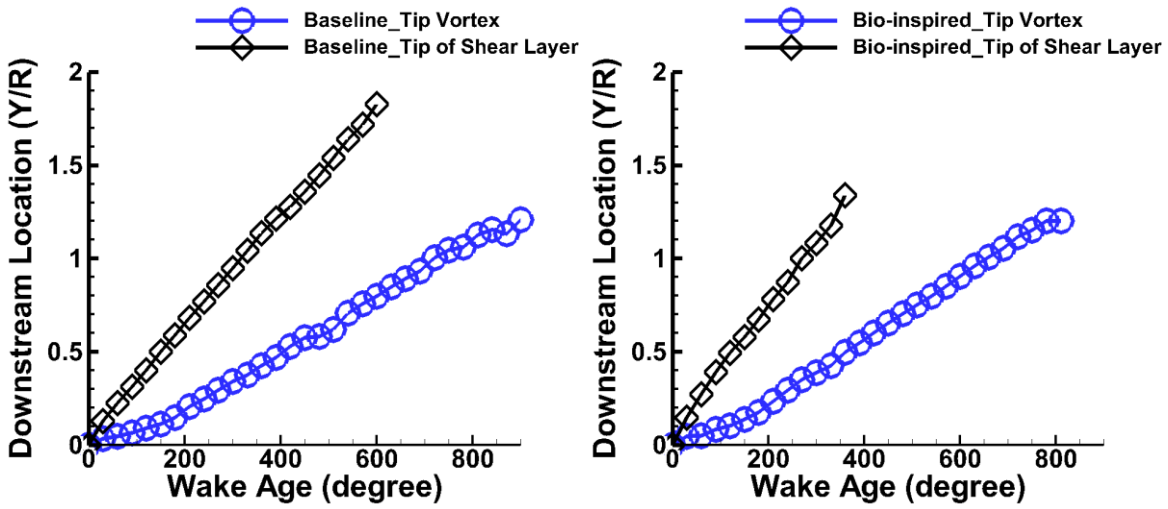

(a) (b)

Figure 21. Vortex location at different wake age

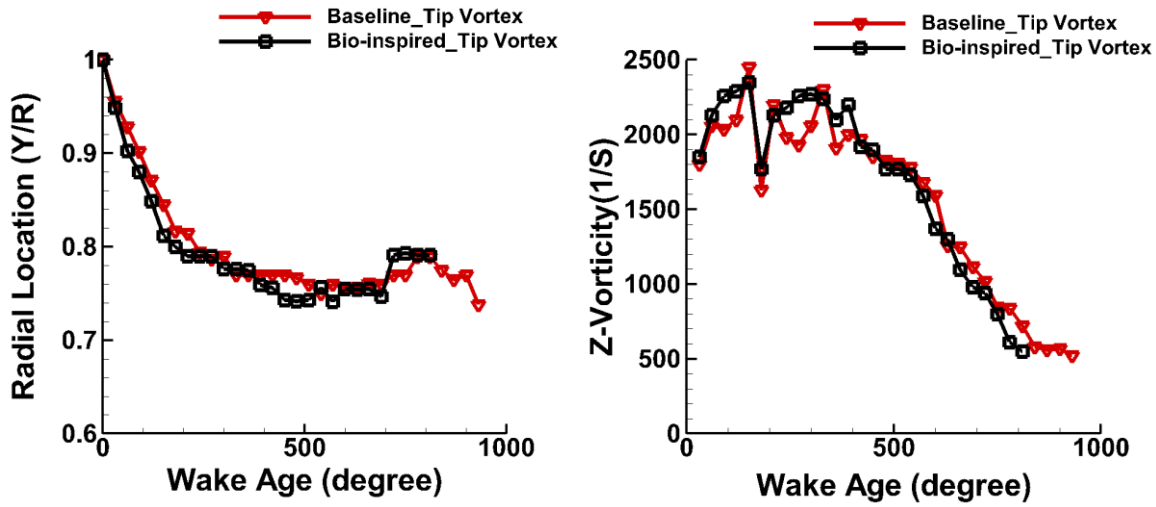

(a) (b)

Figure 22. Tip vortex location and strength comparison

4.4 Conclusion

In conclusion, a comparative experimental study on the aerodynamics and aeroacoustics characteristic between a baseline and a bio-inspired propeller was conducted through force

measurements, as well as sound and flow filed measurements. In this study, the design thrust and aerodynamic area were kept the same for both propellers. The force measurement results revealed that the bio-inspired propeller could generated same thrust as the baseline propeller under same power input. However, the rotational speed of bio-inspired propeller was slower than baseline at hover flight condition. The sound measurement results indicated that the bio-inspired propeller could reduce noise up to 4dB compared to baseline propeller at hover motion. Through PIV measurements, the velocity and vorticity distribution in the downstream are obtained. Compared with baseline, the bio-inspired propeller generated a smaller wake region and demonstrated a faster decay rate of the tip vortex strength.

References

[1] Floreano, D., and Wood, R., "Science,technology and the future of small autonomous drones," *Nature*, vol. 521(7553), 2015, pp. 460–466.

[2] Hoffmann, G., Huang, H., Waslander, S., and Tomlin, C., "Quadrotor Helicopter Flight Dynamics and Control: Theory and Experiment," *AIAA Guidance, Navigation and Control Conference and Exhibit*, 2007.

[3] Achtelik, M., Tianguang Zhang, Kuhnlenz, K., and Buss, M., "Visual tracking and control of a quadcopter using a stereo camera system and inertial sensors," *2009 International Conference on Mechatronics and Automation*, IEEE, 2009, pp. 2863–2869.

[4] Mellinger, D., Michael, N., and Kumar, V., "Trajectory generation and control for precise aggressive maneuvers with quadrotors," *The International Journal of Robotics Research*, vol. 31, Apr. 2012, pp. 664–674.

[5] Lindsey, Q., Mellinger, D., and Kumar, V., "Construction with quadrotor teams," *Autonomous Robots*, vol. 33, Oct. 2012, pp. 323–336.

[6] Mirjan, A., Augugliaro, F., D?Andrea, R., Gramazio, F., and Kohler, M., "Building a Bridge with Flying Robots," *Robotic Fabrication in Architecture, Art and Design 2016*, Cham: Springer International Publishing, 2016, pp. 34–47.

[7] Bristeau, pierre-jean, Martin, P., Salaun, E., and Petit, N., "the role of propeller aerodynamics in the model of a quadcopter UAV," *European control conference* , vol. Vol.2009, 2009.

[8] Yoon, S., Lee, H. C. H., and Pulliam, T. H., "Computational Analysis of Multi-Rotor Flows," *54th AIAA Aerospace Sciences Meeting*, 2016.

[9] Hwang, J. Y., Jung, M. K., and Kwon, O. J., "Numerical Study of Aerodynamic Performance of a Multirotor Unmanned-Aerial-Vehicle Configuration," *Journal of Aircraft*, vol. 52, May 2015, pp. 839–846.

[10] Ditmer, M., Vincent, J., Werden, L., Tanner, J., Laske, T., Iaizzo, P., Garshelis, D., and Fieberg, J., "Bears Show a Physiological but Limited Behavioral Response to Unmanned Aerial Vehicles," *Current Biology*, vol. 25, Aug. 2015, pp. 2278–2283.

[11] Leslie, A., Wong, K. C., and Auld, D., "Broadband noise reduction on a mini-UAV Propeller," *29th AIAA Aeroacoustics Conference*, 2008, pp. 5–7.

[12] Sinibaldi, G., and Marino, L., "Experimental analysis on the noise of propellers for small UAV," *Applied Acoustics*, vol. 74, Jan. 2013, pp. 79–88.

[13] Eppler, R., *Airfoil design and data*, Springer Berlin Heidelberg, 1990.

[14] Leishman, J. G., *Principles of helicopter aerodynamics*, Cambridge University Press, 2006.

[15] Brandt, J. B., and Selig, M. S., "Propeller Performance Data at Low Reynolds Numbers," *49th AIAA Aerospace Sciences Meeting*, 2011, pp. 1–18.

[16] Merchant, M., and Miller, L. S., "Propeller Performance Measurement for Low Reynolds Number UAV Applications," *44th AIAA Aerospace Sciences Meeting and Exhibit*, 2006.

[17] Russell, C., Jung, J., Willink, G., and Glasner, B., "Wind tunnel and hover performance test results for multicopter UAS vehicles," *Annual Forum Proceedings - AHS International*, 2016.

[18] Lopez, O. D., Escobar, J. A., and Pérez, A. M., "Computational Study of the Wake of a Quadcopter Propeller in Hover," *23rd AIAA Computational Fluid Dynamics Conference*, 2017, pp. 1–9.

CHAPTER 5

ROTOR INERACTIONS ON THE AERODYNAMIC AND AEROACOUSTIC PERFORMANCE OF SMALL UAS

Zhe Ning[1], Wenwu Zhou[1, 2], Haixing Li[1], Hui Hu[1]

[1] *Department of Aerospace Engineering, Iowa State University, Ames, Iowa, 50011, USA*

[2] *Gas Turbine Research Institute, Shanghai Jiao Tong University, Shanghai, 200240, China*

Abstract

The flow interactions between laterally-aligned rotors were investigated experimentally to study the rotor-to-rotor interactions on the aerodynamic and aeroacoustic performance of small unmanned aerial vehicles (UAVs). Two identical rotors, similar to the dimensions of Phantom 3 (DJI), were mounted separately on different stages in a wide-open space. High-accuracy force and sound measurements were conducted to document the thrust and noise at various separation distances. The detailed flow structures and corresponding vortex evolutions behind the rotors were resolved clearly by using high-resolution PIV measurements. As the rotor separation distance decreased, intensified flow interactions were noted within the rotors. More specifically, the twin-rotor with separation distance of L= 0.05D exhibited a significantly enhanced thrust fluctuation (i.e., ~ 240% higher) and augmented noise level (i.e., ~ 3dB) in comparison with that of baseline case. Measured PIV results indicated that a strong recirculation region existed near the top-right of the twin-rotor

case, which is believed to be the reason for the increased thrust fluctuations and aerodynamic noise level.

5.1 Introduction

Advances in established control systems and inexpensive electronic devices have greatly encouraged the development of small Unmanned Aerial Vehicles (UAVs)[1–3]. Especially for UAVs with rotary-wing system, they are becoming increasingly attractive to engineers due to their unique hovering ability (e.g. vertical take-off and landing) and user-friendly flight controllability. Varieties of applications in civilian fields, such as package delivery, field site surveillance, disease control, video taking, and personal entertainment, are all driving incentives to adopt this new technique. For the sake of providing sufficient thrust, multi-rotor configurations are frequently used in small UAVs during various tasks. For example, the quadrotor, which is one of the most widely-used configurations, can achieve 6 degrees of freedom movement by simply controlling the rotational speeds of individual rotors [4].

Though UAVs with multi-rotary-wing systems are promising technology for the civilian applications, technical improvements are highly desired for the sake of extending the operating time and reducing the aeroacoustic noise. Typically, a representative operating time for small UAVs is less than half an hour, which is far from sufficient for complex tasks. Therefore, boosting the operation time of UAVs is highly desired. One effective method is to improve the aerodynamic performance of multi-rotor UAVs. Since the knowledge pertinent to helicopter rotor dynamics can’t be applied to small UAVs directly, it requires comprehensive studies to understand the aerodynamic performance of small UAVs.

Bristeau *et al.* [5], who studied the aerodynamic effects of the rotors and their interactions with the UAV body motion, found that the rotor flexibility played an important role in the UAVs' aerodynamics. To obtain first-hand aerodynamic data on commercial UAVs, Russell *et al.* [6] experimentally quantified the thrust coefficients of five multi-rotor UAVs at various wind speeds, rotor speeds, and vehicle attitudes. Similar studies were performed by Brandt and Selig [7] and Merchant and Miller [8], who quantified the performance of small propeller at low Reynolds numbers. Aside from the aerodynamic performance, the broadband noise associated with rotor rotating is another issue that needs to be addressed for small UAVs [9]. Aeroacoustic noise not only can be an annoyance to human life, but to the well-being of animals as well[10]. Leslie *et al.* [11] applied a straight transition strip at the leading edge of blade, and found that the broadband noise of the UAV was greatly reduced. Sinibaldi and Marino [12] experimentally measured the aeroacoustic signatures of two UAV propellers, and reported that while the optimized propeller was much lower than that of the conventional one at lower thrust, the noise of the two would reach a similar magnitude as the thrust increased to a higher value.

Multi-rotor UAVs commonly feature an even number of rotors that are designed into two sets with either clockwise or counter-clockwise rotations. Very few studies can be found in literature that examined the rotor-to-rotor interactions on the aerodynamic and aeroacoustic performances of UAVs. This is with the exception of Yoon *et al.*[13], who computationally analyzed the aerodynamics performance of multi-rotor flows in a quadcopter, and found that the rotor interaction had significant effects on the vertical forces in hover motion. Intaratep *et al.*[14] measured the acoustic levels of a Phantom II at static thrust conditions and reported a dramatic increase in broadband noise as the rotor number increased

from 2 to 4. Though those studies documented the significant impacts of rotor interactions on the performances of small UAVs, extensive work is still needed to understand the underlying fluid mechanics pertinent to multi-rotor interactions, and to uncover how rotor-to-rotor interactions affect the aerodynamic and aeroacoustic performances in small UAVs.

In the present study, an experimental investigation was performed to evaluate the rotor interactions on the aerodynamic and aeroacoustic performances of small UAVs. Two identical rotors with counter-rotating configuration were mounted separately on two stages and arranged laterally in a wide-open space. The separation distance between rotors was adjusted from $L = 0.05D$ to $L = 1.0D$, which is $0.04D$ for the DJI Phantom 3. While high-accuracy measurements were conducted to quantify the thrust and noise at various separation distances, a high-resolution PIV system was used to capture the detailed flow structures and the corresponding vortex evolutions behind the rotor. The effects of rotors separation distance (i.e., $L = 0.05D$, $0.1D$, $0.2D$, and $1.0D$) on the aerodynamic and aeroacoustic performances of the UAVs were examined comprehensively based on the measured results. Finally, the resolved flow fields were correlated with the measured results to elucidate the underlying physics to explore/optimize design for next generation multi-rotor drones.

5.2 Test model and experimental setups

In the present study, the rotor models were made of hard plastic material and manufactured by a rapid prototyping machine (i.e., 3-D printing) that built the rotor models layer-by-layer with a resolution of about 25 microns. As shown schematically in Fig. 1, the rotor has a diameter of 240 mm (D =240 mm), which is close to the size of Phantom 3 rotor.

An E63 airfoil profile was selected to generate the rotor blade due to its high lift to drag ratio at low Reynolds numbers. The printed rotor was able to provide 3.0 Newton thrust at a rotation speed of 4860 RPM. While the chord length of the rotor blade was set to 11 mm at the tip, as for other locations (i.e., from tip to 30% of the blade), they were determined by the optimal chord length equation $C_r = \frac{C_{tip}}{r}$, where C_{tip} is the chord length at the tip, and r is a non-dimensional radius (i.e., 0.3 at 30% of the blade and one at the tip). The root section (i.e., from 30% to 5% of the blade) is considered as support part, which transits smoothly from the 30% chord section to the 5% chord section. It should also be noted that the twist angle of the blade from the tip to 30% of the blade was adjusted from 11.6° to 26.3°, and the solidity of the rotor blade was 0.12 in the present study. The rotor models, oriented horizontally, were installed ~300 mm above the test stage. The experiment stage was ~400 mm above the ground, therefore it is reasonable to neglect any rotor induced secondary flow effect on the test measurements.

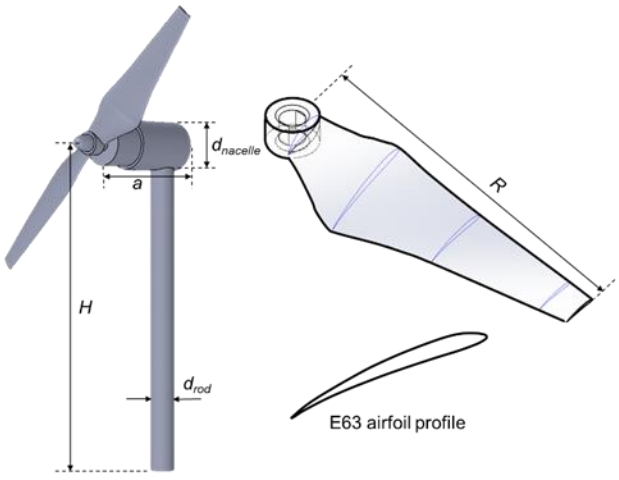

Parameter	R	H	a	d_{rod}	$d_{nacelle}$
Dimension (mm)	120	250	72	16	34

Figure 1. Schematic of rotor model used in the present study.

The experimental study was performed in the Advanced Flow Diagnostic and Experimental Aerodynamic Laboratory located at Iowa State University. Figure 2 (a) shows the experimental setup used for the dynamic thrust and Particle Image Velocimetry (PIV) measurements in the present study, where the main test rig is a custom-built 8020 alumina stage. Equipped with two identical rotors, the propellers in twin-rotor case were rotated in opposite directions (i.e., counter-rotating). Their rotational speeds were controlled separately by Electronic Speed Control. The baseline case was simply achieved by removing an identical rotor from the twin-rotor configuration. Comparisons were made between the twin-rotor and baseline cases to quantify the effect of flow interactions on the thrust performance of the UAV rotor. As shown schematically in Fig. 2 (a), a 16 mm aluminum rod was connected to a high-sensitivity force-moment sensor (JR3 load cell, model 30E12A-I40) to measure the dynamic thrusts of a single rotor. The JR3 load cell, which is composed of foil strain gage bridges, can measure the forces and moments on all three orthogonal axes. The precision for force measurements is within ±0.25% for the full range (40 N). Note that the twin rotors were mounted on two separate stages in order to eliminate the induced mechanical vibration from the nearby rotor. During the experiment, the separation distance (L) between rotor tips was varied from 0.05D to 1.0D to study the rotor interactions on the aerodynamic and aeroacoustic performances of UAV rotors. The JR3 was used to quantify the dynamic load acting on the rotors, which was acquired at a sampling rate of 3000 Hz for 120s. The rotor rotational speed was monitored by a Monarch Instrument Tachometer.

As shown schematically in Fig. 2 (b), an aeroacoustic noise measurement was performed in an anechoic chamber. This chamber has a physical dimension of 12×12×9 feet and its background noise level is lower than 20dB with respect to the reference pressure of 20

μPa. During the experiment, the microphone was installed 6*D* away from the center point *O* of the twin-rotor system. The noise measurement was performed at 5 different angular positions with every 30° interval, starting from the front position of twin-rotor to 30° behind the rotors. All noise measurements were performed at the height of rotor hubs in the same plane with laser sheet. Each sound measurement was recorded for 120s.

In addition, planar PIV measurements were made to quantify the flow interactions between the adjacent rotors, shown in Fig. 2 (a). The air flow was seeded with ~ 2μm water based droplets generated by fog machine (i.e., ROSCO 1900). Illumination was provided by a double-pulsed Nd:YAG laser (NewWave Gemini 200), adjusted on the second harmonic and emitting two pulses of 200 mJ with the wavelength of 532 nm at a repetition rate of 2 Hz. Using a set of high-energy mirrors and optical lenses, the laser beam was shaped into a thin light sheet with a thickness of about 1.0 mm in the measurement interest. The illuminating laser sheet was firstly aligned horizontally along the induced flow direction, bisecting the hub in the middle of the rotor, to perform planar PIV measurements in the *X*-*Z* plane. In the present study, the planer PIV includes both free-run and phase-locked cases. While the free-run PIV were conducted to determine the ensemble-averaged flow statistics behind the rotor, the phase-locked PIV were used to elucidate the dependence of unsteady wake vortices with respect to the position of rotor blades. For the phase-locked PIV measurements, a digital tachometer was used to detect the position of a pre-marked blade. A pulse signal would be generated by the tachometer as the pre-marked blade passed through the vertical PIV plane. The generated signal was then used as the input signal to Digital Delay Generator (DDG) to trigger the PIV system. Through adjusting the time delays between the input signal from tachometer and the transistor-transistor logic signal from the DDG to trigger the PIV system,

different phase angles can be achieved. For each pre-selected phase angle, 300 frames of instantaneous PIV were used to calculate the phase-averaged flow velocity behind the rotor models.

Finally, a stereoscopic PIV (SPIV) experiment was performed to reveal the evolution of vortex structures at different downstream locations behind the rotors (i.e., in *X*-*Y* planes). During the experiment, the laser sheet was rotated 90° from its original position to the vertical direction. Image acquisitions were performed by two 14-bit high-resolution CCD cameras (PCO2000, Cooke Corp.), which were arranged with an angular displacement configuration of about 45 degrees to get a largely overlapped view. With the installation of tilt-axis mounts and the laser illumination plane, the lenses and camera bodies were adjusted to satisfy the Scheimpflug condition. The CCD cameras and double-pulsed Nd:YAG laser were both connected to a Digital Delay Generator (Berkeley Nucleonics, Model 565) to control the timing of the lasers and image acquisitions. A general in-situ calibration procedure was conducted to obtain the mapping functions between the images and object planes for the SPIV measurements. A target plate (~350 × 350 mm^2) with 2 mm diameter dots spaced at intervals of 8 mm was used for the in-situ calibration. The mapping function used in the present study was a multi-dimensional polynomial function, which is third order for the directions parallel to the laser illumination plane (i.e., *X* and *Y* directions), and second order for the direction normal to the laser sheet plane (i.e., *Z* direction).

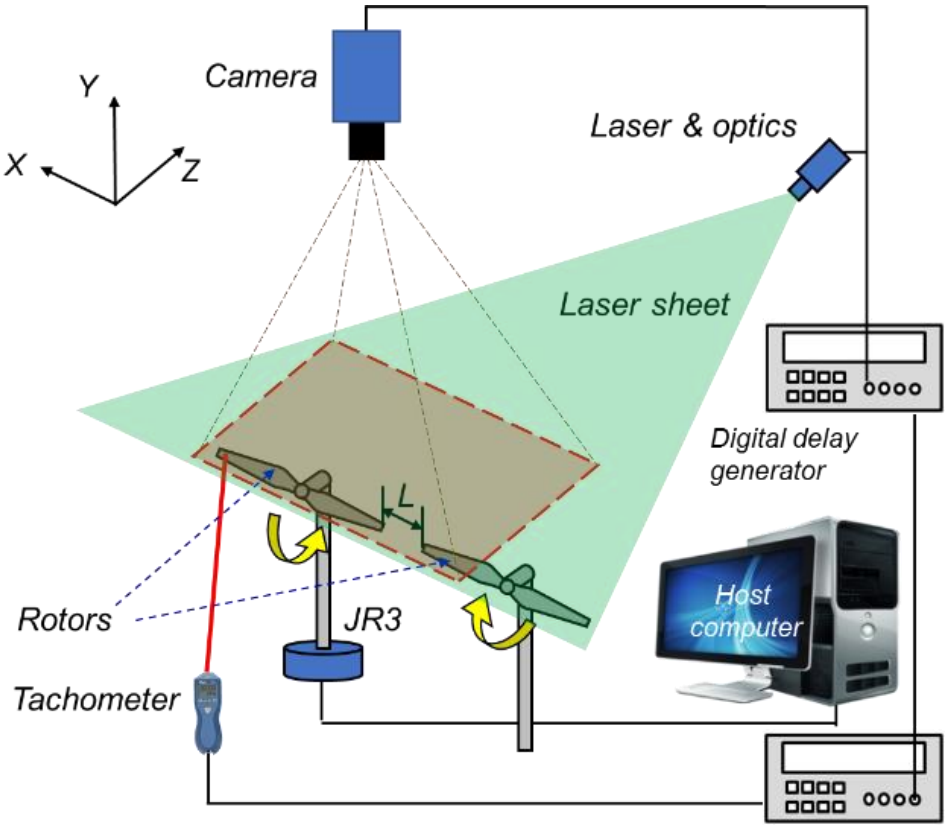

(a) Setup for dynamic loads and planer PIV measurement

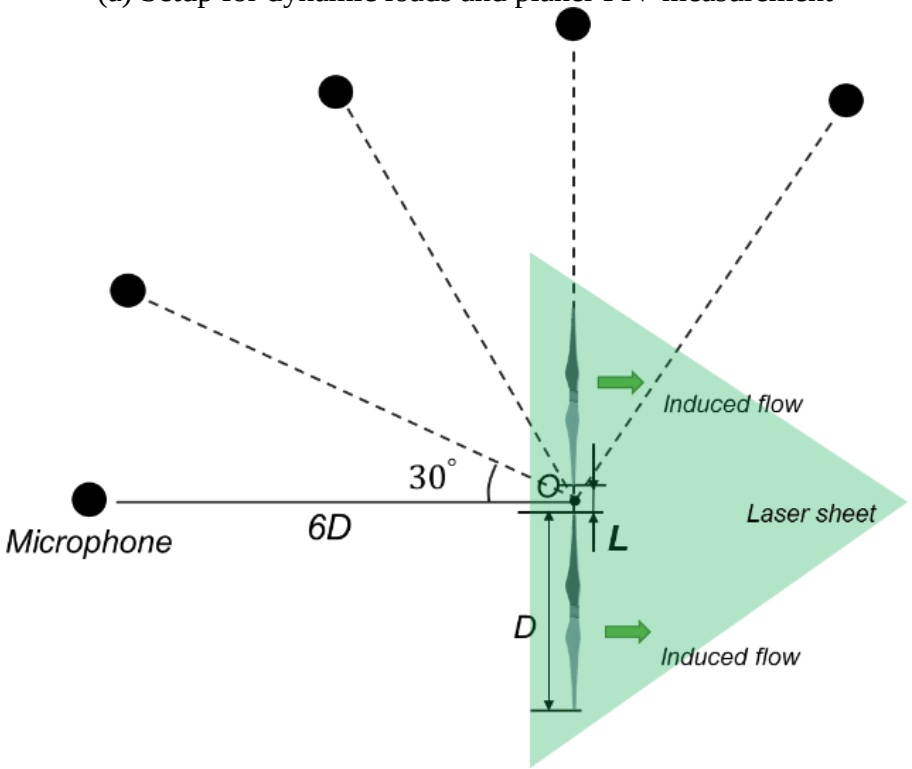

(b) Setup for aeroacoustic measurement

Figure 2. Experimental setups used in the present study.

In the present study, the instantaneous flow velocity vectors were obtained by using a frame-to-frame cross-correlation technique to process the acquired PIV images with an interrogation window size of 32 pixels × 32 pixels. An effective overlap of 50% of the interrogation windows was employed in planar PIV image processing, which resulted in a spatial resolution of 2.4 mm (i.e., 0.01*D*) for the measurement results. Similar processing methodology was also used for the SPIV image processing. The instantaneous 2D velocity vectors were then used to reconstruct all three components of the flow velocity vectors in the laser illuminating plane by using the mapping functions obtained through the calibration procedure. After the instantaneous flow velocity vectors (u_i, v_i, w_i) were determined, the distributions of the ensemble-averaged flow quantities such as mean velocity (*U*, *V*, *W*), normalized turbulence kinetic energy ($0.5\left(\overline{u'^2}+\overline{v'^2}+\overline{w'^2}\right)\Big/U_\infty^2$), spanwise vorticity ($\omega_y=\frac{\partial u_i}{\partial z}-\frac{\partial w_i}{\partial x}$) for the planar PIV measurements, and streamwise vorticity ($\omega_z=\frac{\partial v_i}{\partial x}-\frac{\partial u_i}{\partial y}$) for the SPIV measurements were obtained from a sequence of 1,000 instantaneous PIV results (i.e., 300 for phase-locked PIV). The uncertainty level for the PIV measurements is estimated to be within 3% for the instantaneous velocity vectors, and within 5% for the measured ensemble-averaged quantities such as vorticity distributions.

5.3 Measurements results and discussion

5.3.1 Dynamic load measurement results

Figure 3 presents the normalized thrust coefficient and standard deviation profiles for the twin-rotor and baseline cases at various separation distances, where the thrust coefficient

(i.e., $C_T = \frac{4T}{\rho n^2 D^4 \pi^3}$) and standard deviation are normalized by the corresponding quantities of the single rotor, which are 0.013 and 0.21 Newton respectively. During the experiment, the rotational speed of each rotor (i.e., *n*) was kept constant at 81Hz, but the separation distance between rotor tips was adjusted from *L/D* = 0.05 to 1.0. As shown clearly in Fig. 3, though the separation distance was shortened by a factor of 20, the measured thrust coefficient for the rotor in twin-rotor case was found to drop less than 2%. This suggests that the generated mean thrust is independent of the separation distance. Similar results were also reported by Yoon *et al.*[13], who computationally studied the aerodynamic interactions of multi-rotor flows. It is worth mentioning that the separation distance also has a negligible effect on the power consumption of rotors. For a fixed rotating frequency, consumed power for the twin-rotor case was approximately same (i.e., difference within 1%) for all test cases.

While the separation distance had a limited effect on the thrust coefficient of the rotor, the force fluctuations (i.e., thrust standard deviation) for the monitored rotor in twin-rotor system were found to increase dramatically as the separation distance reduces. More specifically, the measured thrust fluctuations for the $L = 0.05D$ case was found to be ~2.4 times larger than that of the $L = 1.0D$ case. As mentioned above, since the rotors were mounted on two separated stages, the significant augmentation in force fluctuation for the $L = 0.05D$ case was believed to be only caused by the intensified flow interactions rather than mechanical vibrations induced by the second rotor. It should also be noted that for $L > 0.5D$, the thrust fluctuation for the twin-rotor case mitigated greatly and eventually reached a similar level with that of the single case. In general, the rotor interaction effect becomes negligible as *L* larger than 1.0*D*.

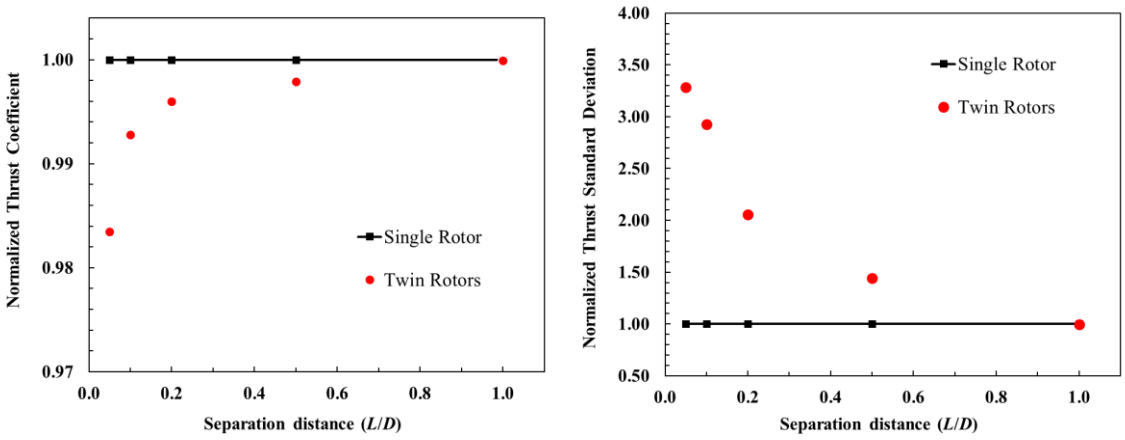

(a) (b)

Figure 3. Effects of separation distance on the thrust coefficient (a) and standard deviation (b) of monitored rotor in twin-rotor case, where the thrust coefficient and standard deviation of single rotor (i.e., baseline case) are 0.013 N and 0.21 N, respectively.

5.3.2 Sound measurement results

The twin-rotor configuration was then investigated to identify the rotor interaction effect on the aeroacoustic performance of small UAVs. The experiment was performed in an anechoic chamber located at Iowa State University. Figure 4 represents the measured sound pressure level (i.e., SPL) distributions at various separation distances (i.e., L = 0.05D, 0.2D, 1.0D). The microphone was installed at five different azimuthal positions (i.e., β = 60°, 90°, 120°, 150°, 180°), which were 6D away from the center and can be approximately treated as far-field locations. Note that, the SPL results displayed in Fig. 4 were the result of the integration of the energy spectrum starting from 20 Hz to 20,000 Hz. As shown clearly in Fig. 4, the measured SPLs were found to increase monotonously as the azimuthal angles increased from 90° to 180°, reached highest levels at position right ahead of the rotors, while exhibited smallest values by the side of rotor. It is well known that the noise map around a

single rotor features a dipole distribution (i.e., symmetric along the rotor plane) [15]. It would reach a maximum noise level at the positions right ahead or behind the rotor (i.e., β = 0°, 180°) but minimum noise at the side positions (i.e., β = 90°, 270°). As for the twin-rotor configuration, it can be treated as quasi-dipole distribution due to the relatively small gaps within the rotors compared to the microphone locations. It should also be noted that as the separation distance becomes smaller, the measured SPLs would gradually increase. A maximum enhancement of about 3 dB can be observed for the L = 0.05D case in comparison to the L = 1.0D case at β = 180°, which is believed to be caused by the enhanced rotor-to-rotor interactions.

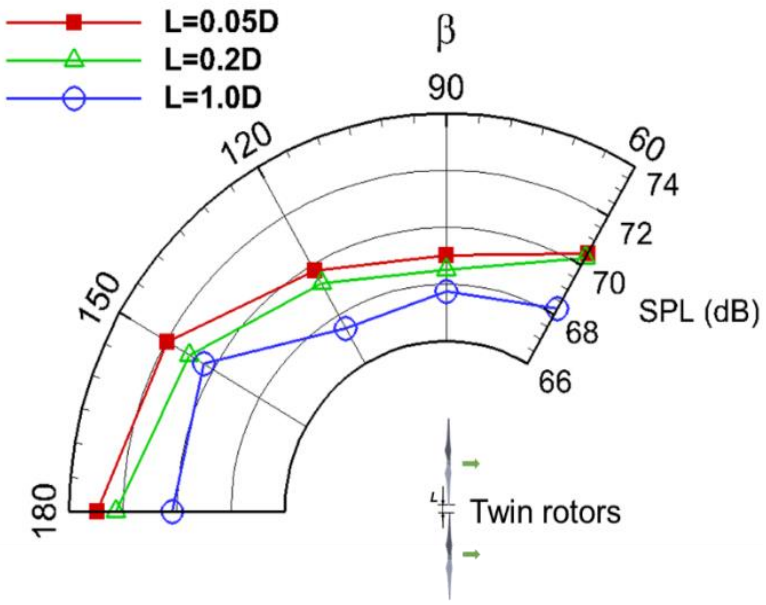

Figure 4. SPL distributions measured at 6*D* away from the center of the twin-rotor configuration.

A spectrum analysis was performed to uncover the noise enhancement in terms of tonal noise and broadband noise. Figure 5 shows the measured sound spectrums as a function of blade passing frequency harmonics at azimuthal angles of β =120° and 180°. Clearly, the

measured SPLs for the L = 0.05D case were found to be much higher than that of the L = 1.0D case at the integral multiple of the BPF (i.e., BPF, BPF2…), indicating an enhanced tonal noise component around the UAV rotors. For incompressible flow condition, tonal noise is dominated by the loading noise [15], which is directly associated with the dynamic loading of the rotor blade. Therefore, the augmented tonal noise for the L = 0.05D case is believed to be caused by the intensified thrust fluctuations as mentioned in Fig. 3. It is worth mentioned that the high sparks at BPF ≈ 20 were confirmed to be the signal from the electronic motors that used to drive the rotors during the experiment.

Compared to the L = 1.0D case, the broadband noises for the L = 0.05D were found to increase mildly at the azimuthal angles of β =120°, 180°. Recalling the Lighthill's stress tensor [15], the broadband noise is largely determined by the complex turbulent flow structures and shear layers, such as secondary flow distortions, blade trailing edge vortices, and tip vortices. As reported by Carolus *et al.* [16], turbulent kinetic energy (TKE) is important parameters that can be used to evaluate the broadband noise level. Enhanced TKE level will lead to augmented broadband noise. Therefore, the broadband noise measurements in the present study suggest an augmented TKE level for the twin-rotor configuration as the separation distance decrease, which was confirmed by the measured PIV results shown below.

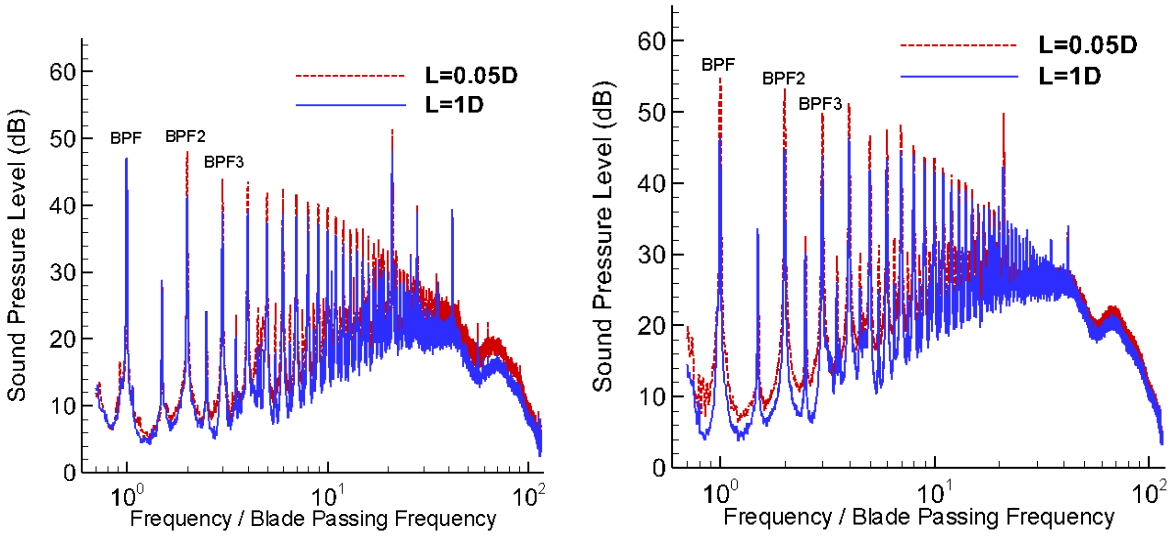

(a) β = 120° (b) β = 180°

Figure 5. Comparison of the measured sound spectrums between the *L* = 0.05*D* and the *L* = 1.0*D* cases at azimuthal angles of 120° and 180°.

5.3.3 Free-run PIV measurement results

As mentioned above, free-run PIV measurements were conducted in the present study to understand how the rotor-to-rotor interactions affect the aerodynamic and aeroacoustic performances of small UAVs. Figure 6 shows the measured free-run PIV results in terms of ensemble-averaged flow velocity and normalized in-plane turbulence kinetic energy (TKE, $0.5\left(\overline{u'^2}+\overline{w'^2}\right)\Big/U_{tip}^2$) for the single and twin-rotor cases, where the rotor tip speed (i.e., $U_{tip}=\omega D/2$) is 61 m/s. As shown quantitatively in Fig. 6 (a), the twin-rotor case presents a similar velocity distribution with that of the single rotor case. This explains the negligible effect of separation distance on measured mean thrusts as indicated in Fig. 3(a). Interestingly,

as the induced flow convected downstream, the high-velocity region was found to converge from around the blade tip location (i.e., ~0.4*D*) to near the root position (i.e., ~0.2*D*), leading to the significant radial contraction behind the rotors. Though the global features of the velocity distribution behind the rotors were similar for both cases, some differences can still be identified from the velocity contours. Compared to the single rotor case, the measured velocity field in the twin-rotor case was slightly 'dragged' toward the adjacent rotor, which is believed to be caused by the Coanda effect (i.e., a phenomenon in which a flow tends to attract to a nearby object). As a result, the *W* velocity component behind the twin-rotor was slightly lower than that of the single rotor in the corresponding down-part region ($-0.5 < X/D < -0.2$).

Fig. 6 (b) shows the comparisons of the normalized in-plane TKE distributions between the single and twin-rotor cases. Clearly, for the single rotor case, regions near the rotor tips were characterized with elevated in-plain TKE, which was caused by the periodic vortex shedding from the blade tip. A similar phenomenon can be observed for the twin-rotor case, except the region with enhanced in-plain TKE was found to be approximately doubled in the lateral direction, but reduced by half in the streamwise direction compared to the single rotor. Since the two rotors were only 0.05*D* apart, the tip vortexes from rotors would interact severely with the nearby vortices, rendering enhanced in-plane TKE distributions in contrast to the single rotor case in the near rotor region. However, because of the intensive interaction within rotors, the associated coherent structures behind the twin-rotor would also dissipate much faster than that of the single rotor, therefore the region with the augmented in-plain TKE level would reduce rapidly as flow convected downstream. The elevated TKE level is believed to be not only related to the significant enhancement of thrust fluctuations discussed

in the twin-rotor case (i.e., shown in Fig. 3), but also leaded to the augmentation of broadband noise (i.e., shown in Fig. 5), which will discuss further in the following Stereoscopic PIV results.

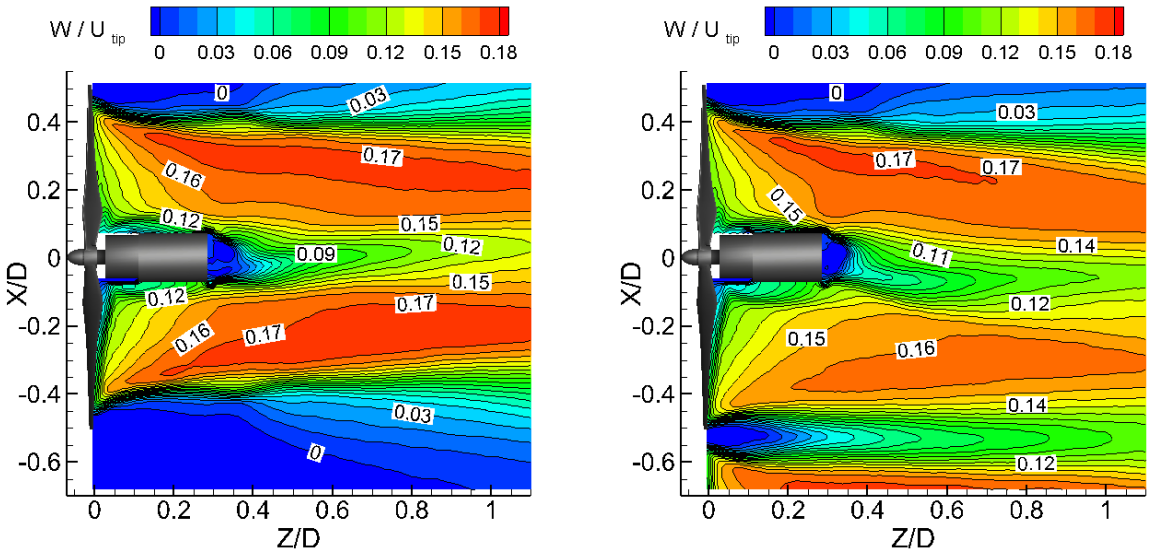

(a)

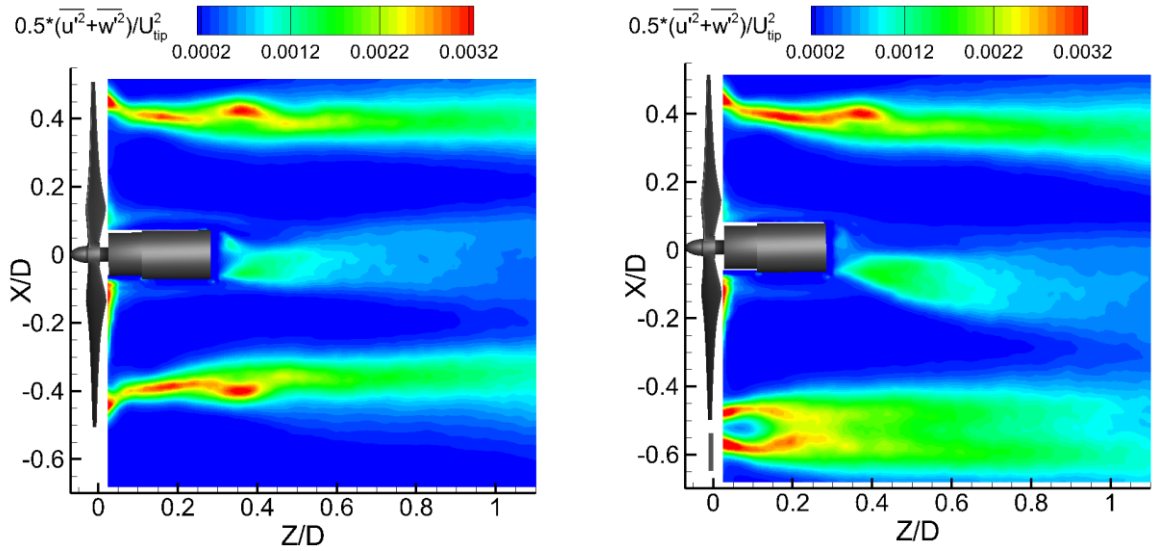

(b)

Figure 6. Measured PIV results for the single rotor (left) and twin-rotor (right, *L*=0.05*D*) cases: (a) Ensemble-averaged velocity field, (b) Normalized in-plane TKE distribution.

5.3.4 Phase-locked PIV measurement results

In the present study, phase-locked PIV measurements were also employed to produce "frozen" images of the unsteady vortex structures behind the rotor at different phase angles. Note that only the phase of left-hand rotor (i.e., shown in Fig. 2(a)) in the twin-rotor system was monitored during the phase-locked PIV test, whereas the other rotor can be treated as a free-run condition. Figure 7 shows the comparison of phase-averaged velocity distributions between the single and twin-rotor cases at two different phase angles (i.e., θ = 0º, 120º). During the experiment, the phase angle is defined as the angle between the vertical *Y-Z* plane and the position of a pre-marked rotor blade. The pre-marked blade was in the most upward position (i.e., within the vertical *Y-Z* plane) for the phase angle of θ = 0º. As shown in Figure 7, the existence of wave-shaped flow structures can be observed clearly at the tip-top height for the single rotor case, which is closely related to the periodical shedding of tip vortices behind the rotor. These wave-shaped flow structures would propagate downstream as the phase angle increased. However, due to the rotor interactions within the twin-rotor case, the wave-shaped structures were found to dissipate much faster and become less pronounced within the gap region in comparison with that of the single rotor case. In addition, these flow structures behind rotors were found to shift radially downward to the adjacent rotor, which is consistent with the measured results shown in Fig. 6.

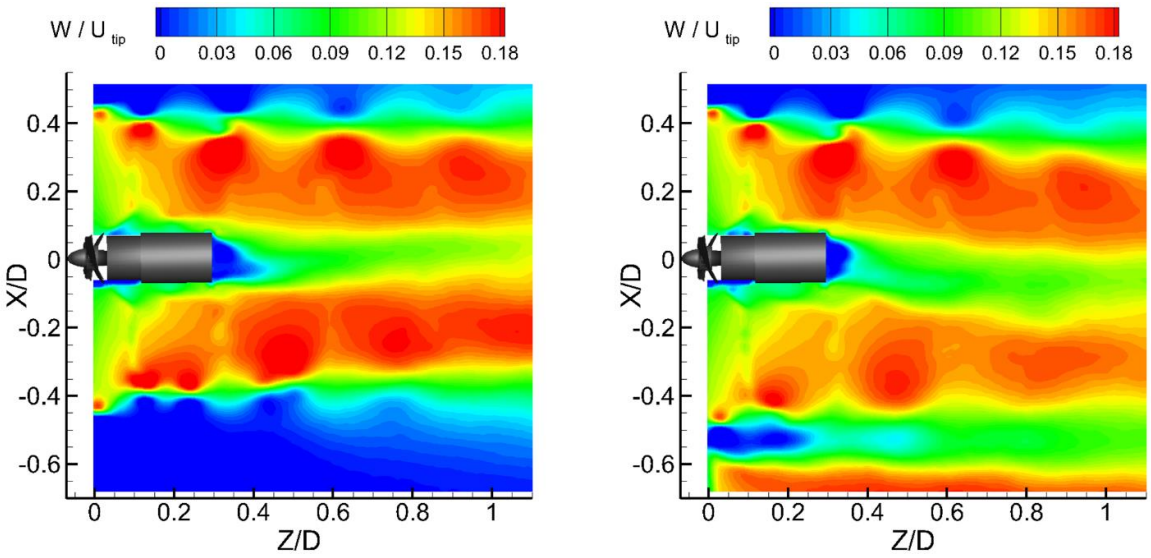

(a)

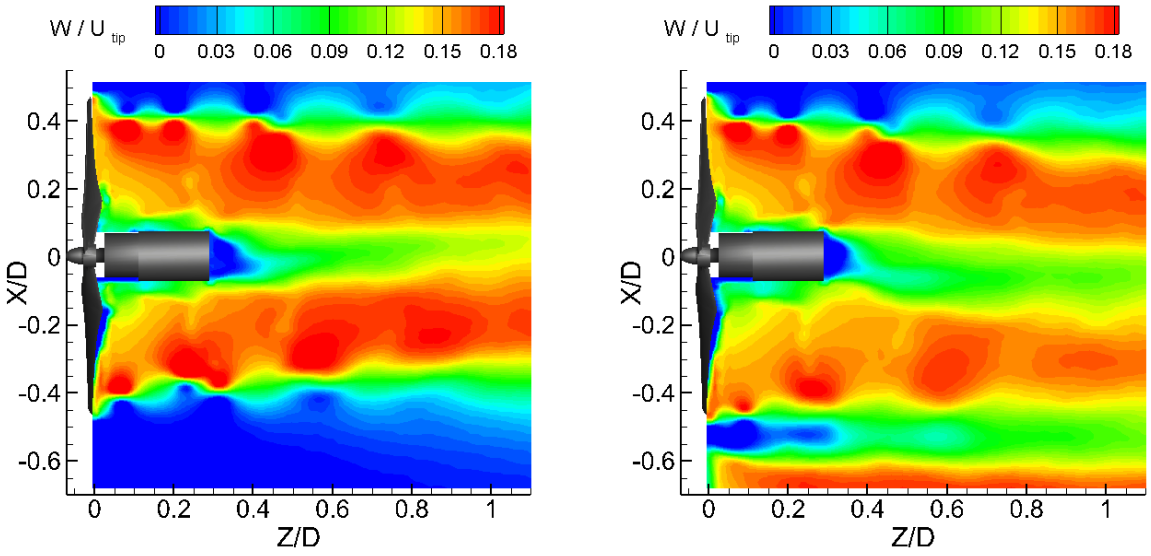

(b)

Figure 7. Phase-locked flow velocity distributions for the single rotor (left) and twin-rotor (right, L=0.05D) configurations: (a) Phase angle θ = 0º, (b) Phase angle θ =120º.

Figure 8 shows the comparison of the phase-locked vorticity distributions between the single rotor and twin-rotor cases, which can be used to reveal the effect of rotor interactions on the unsteady vortices more clearly. Here, the separation distance is 0.05*D*. As expected, the general features of the vorticity distributions were found to be quite similar for both cases, especially for the upper-part region (i.e., as indicated using red dash line). Flows behind the rotors were distinguished by pairs of tip vortices (i.e., # **1 - 5**) and shear layers (i.e., # **a - d**) that trailed after the blades. Note that, the tip vortices were formed because of the pressure differences within the two sides of blade, while the shear layers were generated due to the merging of boundary layers from the upper and lower surfaces of the blade.

For the single rotor case, when the pre-marked blade rotated over the PIV measurement plane, a tip vortex would shed from the tip and propagate axially downstream, shown in Fig. 8 (a). During this process, pairs of vortex structures (i.e., such as vortex # **4** with # **3**, and vortex # **2** with # **1**) would slowly merge into an integral one at ~ 0.7*D*. As the flow convected further downstream, they would completely vanish beyond 1.0*D* due to the aperiodic and highly turbulent flow in the rotor wake. As for the twin-rotor case (i.e., L = 0.05*D*), though similar distributions can be observed for the shear layer (i.e., # **a – d**), tip vortices were found to merge and dissipate much faster in comparison with that of the single rotor case. Representative examples are the isolated vortices (i.e., # **1,** # **2,** # **3,** # **4**), shown in the case of single rotor, that become much harder to discern as Z/D >0.2 in twin-rotor case.

As the phase angle increased to θ = 120°, the associated turbulent structures, such as the shear layers and tip vortices, were found to propagate downstream in contrast to that of θ = 0°. Focusing on the evolution of the vortex sheet # **d** (i.e., shear layer # **d**), it was initially adjacent to tip vortex # **4**. As vortices convected axially downstream, however the outboard

edge of the shear layer # **d** in Fig. 8 (b) was found to interact with the tip vortex # **3** rather than vortex # **4**. This is because the convecting speed (i.e., *W* velocity shown in Fig. 7) of the shear layer was much higher than that of the tip vortex, thus the outboard edge of the shear layer would surpass the corresponding vortex, leading to complex vortex interactions. Very similar phenomena were also reported by Leishman [17], who described the wake characteristics behind a helicopter rotor.

5.3.5 Stereoscopic PIV measurement results

To further explore the underlying physics pertinent to rotor-to-rotor interactions of small UAVs, a stereoscopic PIV (SPIV) system was also utilized to quantify the complex flow field behind the rotors at multiple locations along the induced flow direction. Note that the vectors shown in Figure 9 and 10 are the resultant vectors of in-plane radial and tangential velocities behind the rotor.

Fig. 9 and Fig. 10 show the comparisons of the ensemble-averaged turbulent quantities between the single rotor and twin-rotor cases at the downstream locations of X/D = 0.1 and 1.0 respectively. As revealed clearly in Fig. 9 (a), the mean velocity contour (i.e., *W* component) behind the single rotor was found to be circular and symmetric as expected. Interestingly, the rotating direction of the wake flow was found to be in the same direction with that of the rotor blade (i.e., both in counter-clockwise), which is contrary to the wind turbine scenario [18,19], where the swirling direction of the wake is opposite to the wind turbine rotation. This phenomenon is caused by an inherent working mechanism difference where the rotor drives the flow in the UAV case, but the it is the flow that drives the rotor in the

wind turbine case. It should also be noted that while the velocity distribution behind the single rotor was in a circular shape, a droplet-shaped velocity field was observed for the twin-rotor case due to the flow disturbance from the nearby rotor. Carefully inspecting the flow features behind the twin rotors, a region with flow separation was identified at the top-right corner, which is believed to be the resultant effect of upwash flow and radial flow. Within the interaction region, the two rotors would generate a steady upwash flow that interacts severely with the radial flow, resulting in the flow separation shown in Fig. 9 (a).

As the airflow traveled further downstream to the *X/D* = 1.0 plane, illustrated in Fig. 10 (a), the previous circular-shaped velocity field behind the single rotor was transformed into a 'horseshoe' shape. Not only that but also the orientation of the velocity contour was found to rotate by ~35° from its original position (i.e., in *X/D* = 0.1 plane). Due to the flow inertia, the air stream would continue rotating after being accelerated by the blade as it traveled further downstream. Though a similar deviation angle was observed for the twin-rotor case, the velocity contour was found to bend slightly toward the adjacent rotor in comparison with that of the baseline, especially for the region close to the flow separation region (i.e., region in black dash line). This phenomenon is believed to be closely related to the aforementioned Coanda effect (i.e., Fig. 6) where the induced airflow behind the twin rotors would be attracted and bent toward the nearby rotor.

Fig. 9 (b) shows the measured normalized TKE distributions ($0.5\left(\overline{u'^2}+\overline{v'^2}+\overline{w'^2}\right)/U_{tip}^2$) for the single rotor case in comparison with that of the twin-rotor case in the *X/D* = 0.1 plane. Clearly, an O-ring shaped TKE distribution was found to be the dominant feature for the

single rotor case, which is because of the periodic vortex shedding from the rotor tip. The measured results are in accordance with the measured planar PIV results shown in Fig. 6.

Though the general pattern was found to be similar for both cases, except a region with significantly high TKE levels was observed at the top-right corner for the twin-rotor case. As expected, flow separation would lead to greatly enhanced turbulence fluctuations (i.e., TKE), which consequently resulted in dramatically intensified thrust fluctuations for the twin-rotor case as mentioned in Fig. 3 (b). This also confirmed the conjecture that the enhanced broadband noise shown in Fig. 5 was caused by the augmented TKE level. Imagine that as the blade struck through the separation region, it would certainly suffer strong fluctuations, leading to augmented TKE and broadband noise. Due to the viscous dissipation within the shear layer, the measured TKE levels for both cases were found to decrease rapidly and reach a similar level at the location of X/D = 1.0 (i.e., shown in Fig. 10 (b)). Therefore, high TKE zone could only exist in the near-blade region since it dissipates rapidly as induced flow propagated downstream. Figure 11 shows the evolution of the ensemble-averaged streamwise velocity and the normalized TKE distributions for the single and twin-rotor cases at three typical streamwise locations (i.e., X/D = 0.1, 0.5, and 1.0). As shown clearly in the figure, the mean velocity fields for both cases were found to become more uniform as induced flow convected downstream. In addition, the orientation of the induced flows was found to rotate by approximately 35° (i.e., in the plane of X/D = 0.1) in comparison with its original vertical position (i.e., in the plane of X/D = 1.0). As for the normalized TKE distributions given in Fig. 11 (b), a significantly higher TKE level was initially observed at the top-right region of twin-rotor case in X/D = 0.1 plane, but it then

decreased rapidly and reached a similar level with that of the single rotor due to the viscous dissipation within the shear layer.

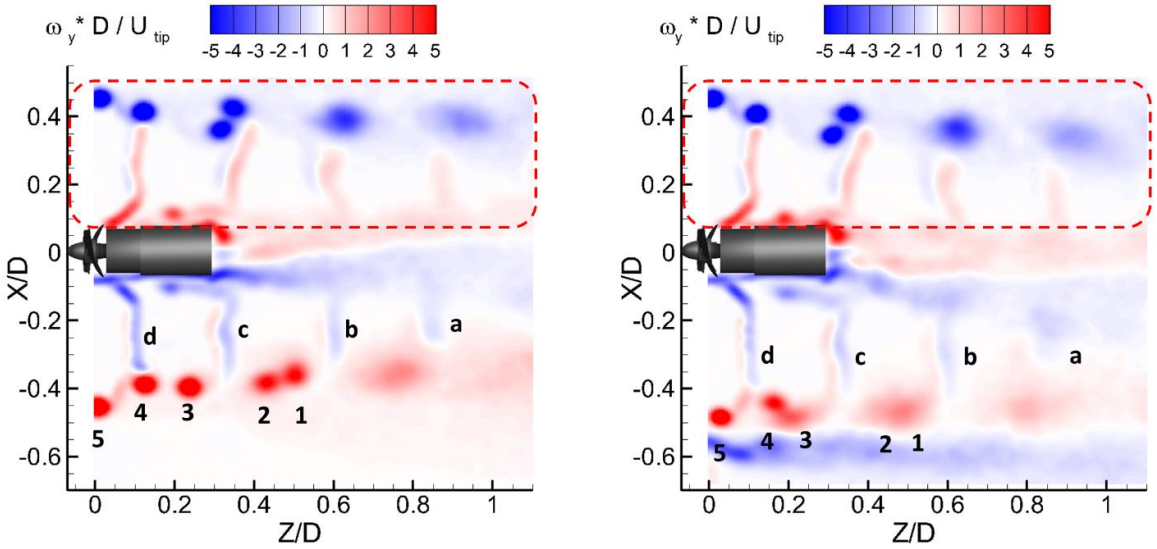

(a)

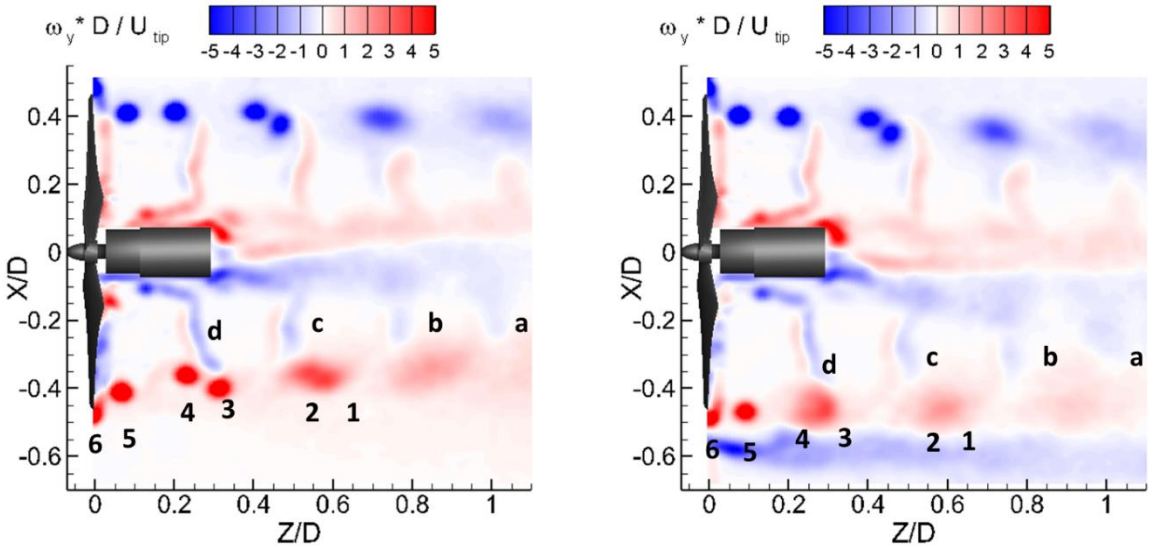

(b)

Figure 8. Phase-locked vorticity distributions for the single rotor (left) and twin rotors (right, L=0.05D) configurations: (a) Phase angle θ = 0º, (b) Phase angle θ =120º.

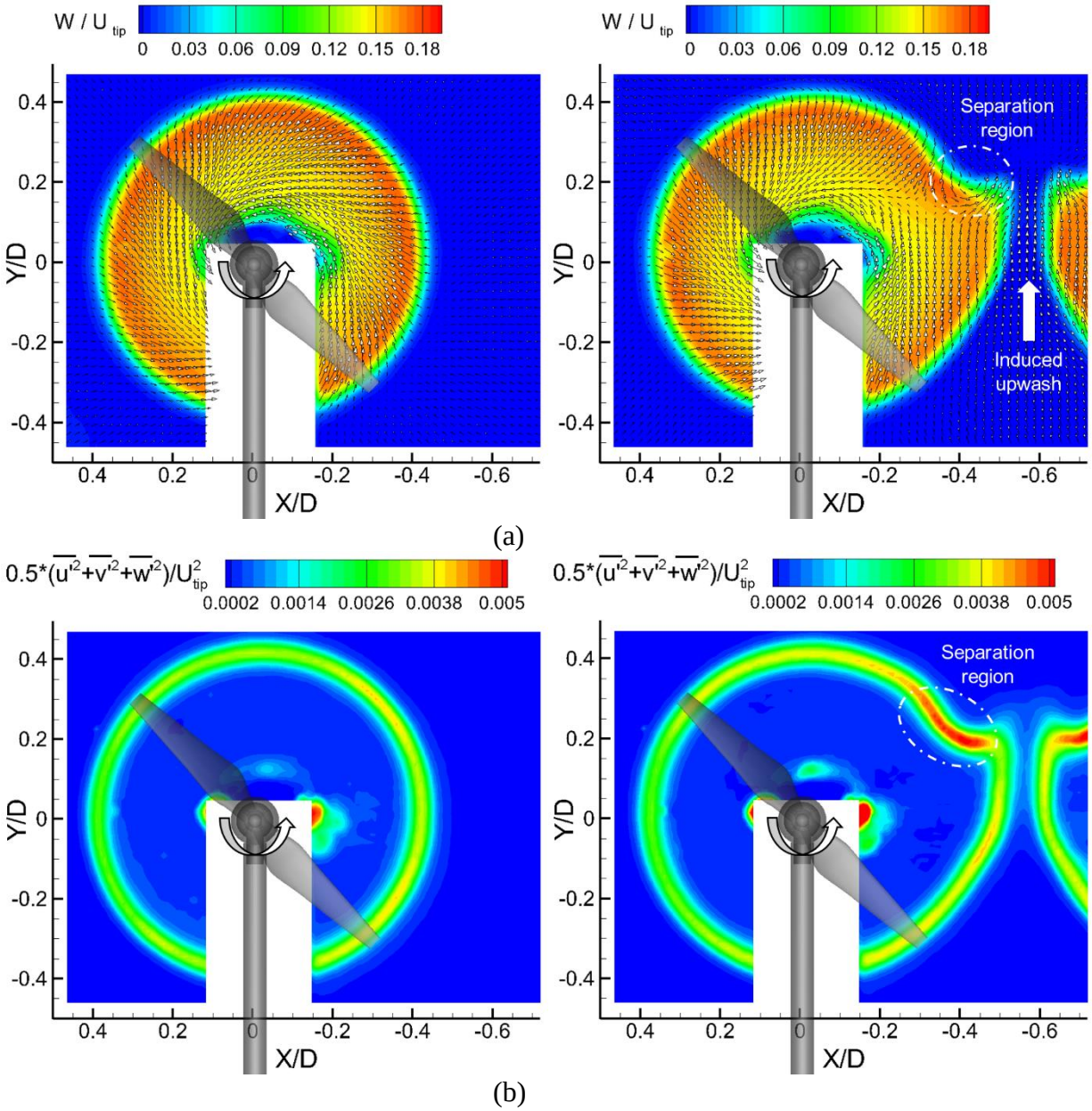

Figure 9. Measured SPIV results for the single rotor (left) and twin-rotor (right, *L*=0.05*D*) configurations in the *X/D* = 0.1 cross plane: (a) Ensemble-averaged velocity field, (b) Normalized TKE distribution.

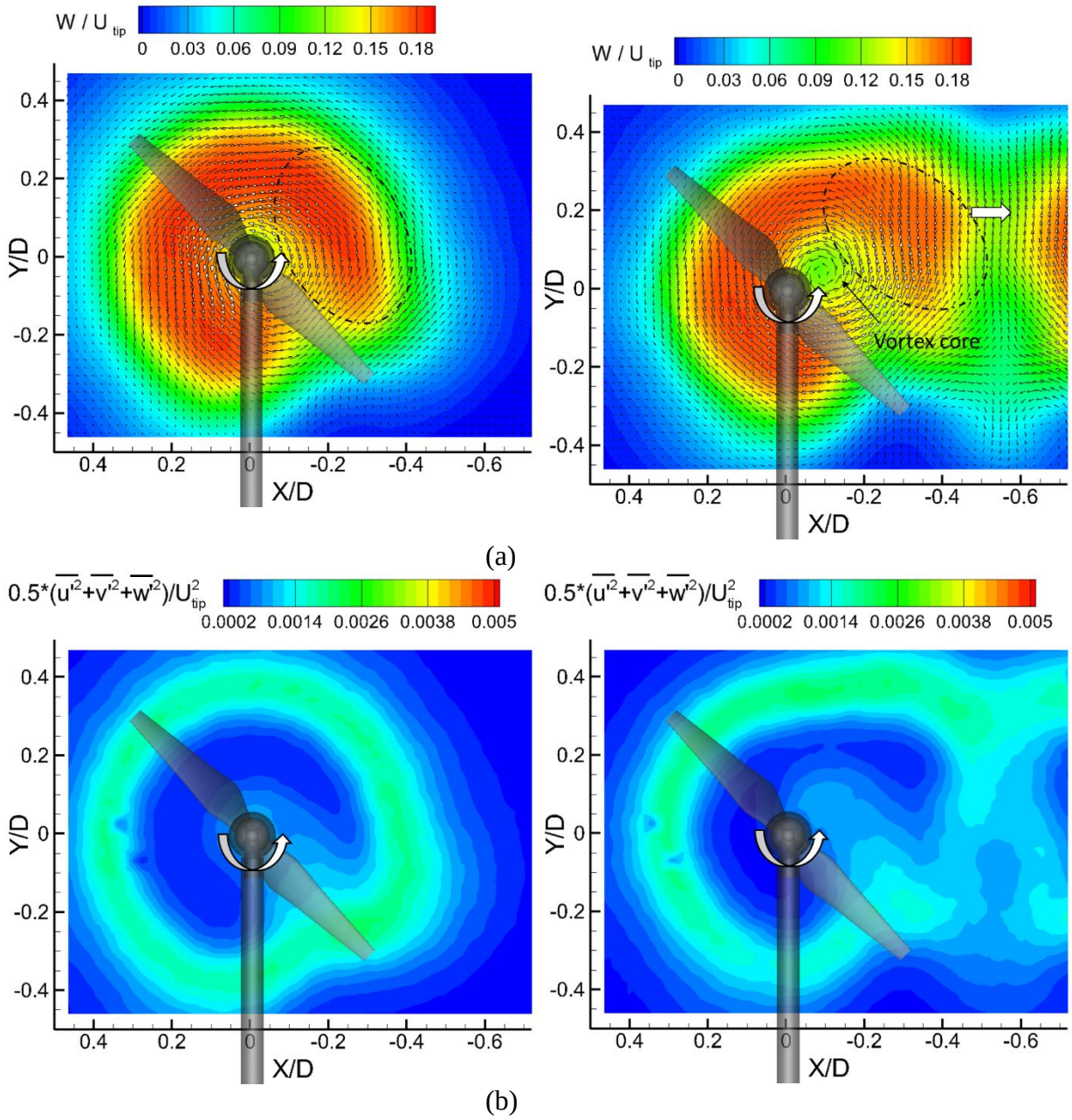

Figure 10. Stereoscopic PIV results for the single rotor (left) and twin-rotor (right, *L*=0.05*D*) configurations in the *X/D* = 1.0 cross plane: (a) Ensemble-averaged velocity field, (b) Normalized TKE distribution.

Based on above measured results, the twin-rotor case with *L/D* = 0.05 experienced the strongest flow interactions within the rotors. Adding a wingtip, rather than enlarging the separation distance, might be a practical method to alleviate the flow interaction effects if UAV designers aren't willing to sacrifice the compactness of the drones.

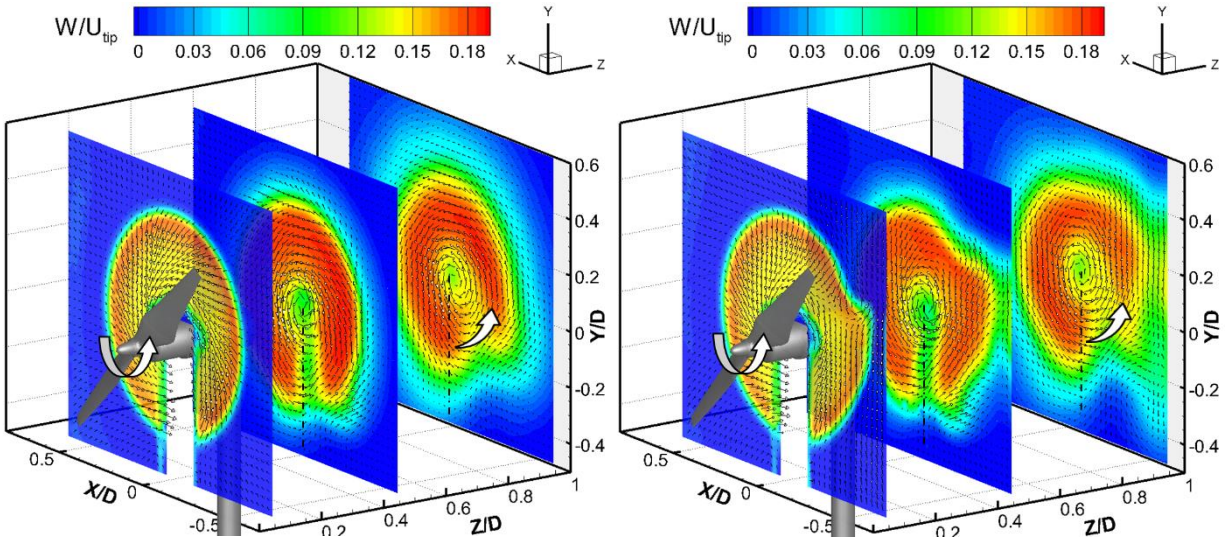

(a)

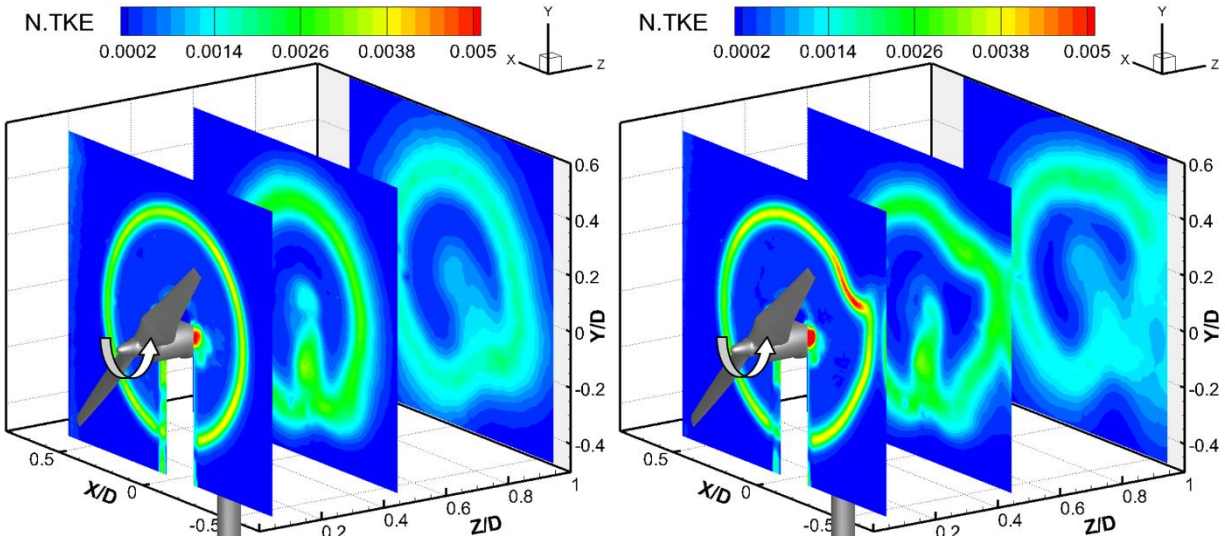

(b)

Figure 11. Stereoscopic PIV results for the single rotor (left) and twin rotors (right, *L*=0.05*D*) configurations at *X/D* = 0.1, 0.5, and 1.0 locations: (a) Ensemble-averaged velocity field, (b) Normalized *TKE* distribution.

5.4 Conclusions

An experimental investigation was performed to study rotor-to-rotor interactions on the aerodynamic and aeroacoustic performances of small UAVs. While the JR3 force transducer and microphone were used to quantify the thrust and noise levels of the rotors, a high-resolution Particle Image Velocimetry (PIV) system was used to conduct detailed flow field measurements to reveal the dynamic interactions between the rotors. The effects of separation distance (L = 0.05D, 0.1D, 0.2D, and 1.0D) on the aerodynamic and aeroacoustic performance of UAVs were evaluated in detail based on the quantitative force, noise, and PIV measurements.

It was found that, while the separation distance had a negligible effect on the thrust coefficient of the rotor (i.e., variation within 2% for all test cases), the thrust fluctuations (i.e., thrust standard deviation) were found to increase dramatically as the separation distance became smaller. More specifically, the measured thrust fluctuations for the twin-rotor case (i.e., L= 0.05D) were found to be ~2.4 times larger than that of the baseline case. This is believed to be caused by the complex flow interactions within rotors as revealed by the detailed PIV measurements. It was also found that the noise distribution for the twin-rotor case is a function of both azimuthal angle and separation distance, where the measured noise was found to increase as the azimuthal angle increased from 90° (i.e., side position) to 180° (i.e., right ahead the rotors), and to increase as the separation distance reduced from L = 1.0D to L = 0.05D. A maximum noise enhancement of ~3 dB was recorded for the L = 0.05D case in comparison to that of the L = 1.0D case, which is the result of both tonal and broadband noise augmentations as indicated in the sound spectrum analysis.

As shown quantitatively from the planar PIV and Stereoscopic PIV measurement results, the induced flow behind the rotors was found to contract radially toward the axis of the rotor as the flow convected downstream. For the single rotor case, while most of the regions in the wake were devoid of flow structures, only the region near the blade tips was characterized by elevated in-plain TKE (i.e., in *X*-*Z* plane) due to periodic tip vortex shedding. A similar phenomenon was observed for the twin-rotor case, except that the TKE region was significantly higher at the top-right area than that of single rotor case. Due to the resultant effect of upwash and radial flows in the near wake of the twin-rotor case, a region with a flow separation was identified in the *X*-*Y* cross plane, which led to significantly higher TKE distributions and thrust fluctuations behind the twin rotors. It should also be noted that the velocity field for the twin-rotor case was found to be attracted and bent toward the nearby rotor due to the Coanda effect.

In general, the measured quantitative results given in the present study are believed to be very beneficial in understanding how rotor-rotor interactions affect the aerodynamic and aeroacoustic performances of small UAVs. It depicted a vivid picture regarding the complex flow features behind the rotors, which further explained their correlations with the enhanced force fluctuations and noise levels. Such quantitative information is highly desirable to elucidate the underlying physics pertinent to rotor interactions, and to explore/optimize design paradigms for better commercial UAV designs.

References

[1] Bouabdallah, S., Becker, M., and Siegwart, R., "Autonomous miniature flying robots: coming soon! - Research, Development, and Results," *IEEE Robotics & Automation Magazine*, vol. 14, Sep. 2007, pp. 88–98.

[2] Lucieer, A., Turner, D., King, D. H., and Robinson, S. A., "Using an Unmanned Aerial Vehicle (UAV) to capture micro-topography of Antarctic moss beds," *International Journal of Applied Earth Observation and Geoinformation*, vol. 27, 2014, pp. 53–62.

[3] Goebel, M. E., Perryman, W. L., Hinke, J. T., Krause, D. J., Hann, N. A., Gardner, S., and LeRoi, D. J., "A small unmanned aerial system for estimating abundance and size of Antarctic predators," *Polar Biology*, vol. 38, May 2015, pp. 619–630.

[4] Otsuka, H., and Nagatani, K., "Thrust loss saving design of overlapping rotor arrangement on small multirotor unmanned aerial vehicles," *2016 IEEE International Conference on Robotics and Automation (ICRA)*, IEEE, 2016, pp. 3242–3248.

[5] Bristeau, P., Martin, P., and Salaün, E., "The role of propeller aerodynamics in the model of a quadrotor UAV," *Control Conference (ECC*, 2009.

[6] Russell, C., Jung, J., Willink, G., and Glasner, B., "Wind Tunnel and Hover Performance Test Results for Multicopter UAS Vehicles," *AHS 72nd Annual Forum*, FL: 2016.

[7] Brandt, J., and Selig, M., "Propeller Performance Data at Low Reynolds Numbers," *49th AIAA Aerospace Sciences Meeting including the New Horizons Forum and Aerospace Exposition*, Reston, Virigina: American Institute of Aeronautics and Astronautics, 2011.

[8] Merchant, M., and Miller, L. S., "Propeller Performance Measurement for Low Reynolds Number UAV Applications," *44th AIAA Aerospace Sciences Meeting and Exhibit*, 2006.

[9] Gur, O., and Rosen, A., "Design of Quiet Propeller for an Electric Mini Unmanned Air Vehicle," *Journal of Propulsion and Power*, vol. 25, May 2009, pp. 717–728.

[10] Ditmer, M. A., Vincent, J. B., Werden, L. K., Tanner, J. C., Laske, T. G., Iaizzo, P. A., Garshelis, D. L., and Fieberg, J. R., "Bears Show a Physiological but Limited Behavioral Response to Unmanned Aerial Vehicles," *Current Biology*, vol. 25, Aug. 2015, pp. 2278–2283.

[11] Leslie, A., Wong, K. C., and Auld, D., "Broadband Noise Reduction on a mini-UAV Propeller," *14th AIAA/CEAS Aeroacoustics Conference (29th AIAA Aeroacoustics Conference)*, Reston, Virigina: American Institute of Aeronautics and Astronautics, 2008.

[12] Sinibaldi, G., and Marino, L., "Experimental analysis on the noise of propellers for small UAV," *Applied Acoustics*, vol. 74, Jan. 2013, pp. 79–88.

[13] Yoon, S., Lee, H. C. H., and Pulliam, T. H., "Computational Analysis of Multi-Rotor Flows," *54th AIAA Aerospace Sciences Meeting*, 2016.

[14] Intaratep, N., Alexander, W. N., Devenport, W. J., Grace, S. M., and Dropkin, A., "Experimental Study of Quadcopter Acoustics and Performance at Static Thrust Conditions," *22nd AIAA/CEAS Aeroacoustics Conference*, 2016, pp. 1–14.

[15] Blackstock, D. T., *Fundamentals of physical acoustics*, A WILEY-INTERSCIENCE, 2000.

[16] Carolus, T., Schneider, M., and Reese, H., "Axial flow fan broad-band noise and prediction," *Journal of Sound and Vibration*, vol. 300, 2007, pp. 50–70.

[17] Leishman, G., *Principles of helicopter aerodynamics*, Cambridge University Press, 2006.

[18] Hu, H., Wei, T., and Wang, Z., "An Experimental Study on the Wake Characteristics of Dual-Rotor Wind Turbines by Using a Stereoscopic PIV Technique," *34th AIAA Applied Aerodynamics Conference*, 2016.

[19] Wang, Z., Tian, W., Ozbay, A., Sharma, A., and Hu, H., "An experimental study on the aeromechanics and wake characteristics of a novel twin-rotor wind turbine in a turbulent boundary layer flow," *Experiments in Fluids*, vol. 57, Sep. 2016, p. 150.

.

CHAPTER 6

EXPERIMENTAL STUDY ON ICING PHYSICS OF SMALL UAS PROPELLER UNDER DIFFERENT ENVIRONMENTAL CONDITIONS

Zhe Ning, Yang Liu, Hui Hu (✉)

Department of Aerospace Engineering, Iowa State University, Ames, Iowa, 50011

Abstract

In this research, the dynamic ice accumulation process and the degradation of aerodynamic performance due to the icing event has been investigated through a series of experiments. The Icing Research Tunnel with a temperature control system and a spray system was used to conducted all of the experiments. It has the potential to adjust the temperature and liquid water content to simulate different icing conditions: rime ice, glaze ice, and mixed ice. The detailed ice structures and dynamic icing process were captured by a high speed imaging system through "phase-locked" technique. Meanwhile, the aerodynamics force and power consumption were measured simultaneously with the high speed image acquisition. The sufficient information of the ice structure, aerodynamic force variation, change in power consumption during the dynamic ice accumulation process helped us to explore the underlying icing physics and better understand the icing influence on the aerodynamic performance under varies icing conditions.

6.1 Introduction

Benefited from the well-developed control theories and low-cost electronic devices, the small Unmanned Aerial System (UAS) experienced rapid development during the past twenty years[1]. Normally, the small UAS consists three categories: the rotary-wing aerial system, fixed wing aircraft, and flapping wing aerial vehicle. Due to the vertical take-off and landing (VTOL) motion and excellent hovering ability, the rotary-wing system attracted more attention in both industry and academia. It has been recognized as a popular planform and explored to many civilian and military applications, such as, video and image taking, package delivery, field monitoring, disease control, rescue operation, and inspection.

With the broadened application range, the small UAS would operate in a cold climate environment. Such as, accomplishing rescue operation in high mountain field for seeking avalanche survivors, and conducting power line inspection during the winter time. Therefore, during the operation, the small UAS would face to the icing problems. The inflight icing is an essential unsolved problem influence the flight safety for all of the aircraft, such as, fixed wing airplane, rotorcraft, large size UAS, and small UAS. From 1978 to 2010, there are total 1202 icing related accidents reported by National Transportation Safety Board (NTSB) and NASA Aviation Safety Reporting System (ASRS)[2].

Recent years, many research work has been performed to study the inflight icing physics, the icing impact on the flight performance, and icing mitigation and protection of the large size aircrafts. The ice structure accumulated on the aircraft wing or rotor blade, and the icing parameters affected the ice accumulation process has been explored by many researchers[3–11]. It was found that the liquid water content (LWC), ambient temperature, median volumetric diameter (MVD), and incoming air speed would affect the ice types and accumulated ice

structures. Normally, the ice accumulated on the airfoil consists rime ice, glaze ice and mixed ice based on the difference in the surrounding environment. The rime ice was formed under relative low temperature (i.e., <-10°C) and small liquid water content (LWC). Under this condition, due to the released latent heat was quickly removed by the heat transfer process (i.e., heat conduction and heat convection) during the ice accumulation, the inflight water droplet directly frozen upon the wing surface after its impinging. Therefore, the rime ice accumulation process can be viewed as the ice particle build upon the surface layer by layer. As a result, the ice structure follows the geometry of the impinging surface of the objective and the color of rime ice was white. The glaze ice was formed under the temperature just below the frozen point and large LWC. Since the heat conduction and convection cannot remove all of the released latent heat during icing process, part of the flying water droplet will freeze to ice after the impinging, meanwhile, remaining water droplet will keep the liquid phase. Under the influence of the wind induced shear force, the unfrozen water will flow on the wing surface. For rotorcraft, the centrifugal force would also transport the unfrozen water along the blade from root towards tip. Therefore, the ice structure under glaze ice condition is irregular and complex. Although several researchers focused their emphasis on the heat transfer and water transportations, only simplified mass and energy transfer models was addressed to understand the glaze ice accumulation on the aircraft surfaces due to the complex of the heat and mass transfer and wind driven water transportation[12–16]. The mixed ice is formed under the environment between typical rime ice condition and typical glaze ice condition.

The ice formed on the aircraft wing or rotor blade modified the airfoil shape even the entire planform. The effect on the aerodynamic performance due to the ice accumulation has

also been studied by many researchers[3,10,11,17–19]. In general, the ice accumulated on the wing would degrade the lift generation, dramatically increase the profile drag, cause the airplane stall at a smaller angle of attack, and increase the power required to accomplish flight tasks. For rotorcraft, the accumulated ice would also increase the blade flapping due to the mass increase, and decrease the maximum forward flight speed due to the stall angle change. In serious situation, the inflight icing could cause the aircraft out of control, and lead to personal safety problems and property damage. Compared with the rime ice, the irregular geometry of the glaze ice had more significant effect on the aerodynamic performance.

In addition to the ice structure and aerodynamic performance degradation studies, several anti-icing and de-icing researches were also found in literature[11,20–24]. The anti-icing and de-icing can be classified into passive and active methods. The passive method is to modify the wing surface to achieve ice-phobic or hydrophobic. With this method less ice would accumulate on the surface. The active method means preventing or removing ice with extra energy input. The traditional active methods contain: pneumatic boots and thermal melting. Currently, ultrasonic shear wave and plasma were also used to prevent ice formation.

Although, many icing research has been conducted, less work can be found in literature to study the icing physics of the small UAS. Liu conducted experimental studies to investigate the dynamic icing process over a rotating propeller model and the wettability effect on the ice accretion[25–27]. Compared to the traditional large size aircraft, a significant difference is that the small UAS has a smaller size. According to Green, the influence of the icing phenomenon on the small size aircraft is more significant than the large one[28]. Szilder performed a CFD simulation to explore the Reynolds number effect on the ice accretion process[29]. He found that, the relative size of the ice accumulation increase as the decreasing

Reynolds number. As a result, the degradation of the aerodynamic performance would be greater. The small UAS, especially the rotary wing systems, always operates at a lower altitude where the LWC is higher and the temperature is warmer than high altitude. As a result, the glaze ice is easy to formed on the propeller. Meanwhile, the flight speed of the small UAS is low, which lead to a longer exposure time in the icing conditions. In addition, the airfoil and the blade planform used in small UAS design is quite different than large aircraft. These difference in the configuration would definitely influence the ice accumulation process and the icing impact on the aerodynamics performance.

So far, there was no study has been performed to investigate the dynamics icing process and icing impact on the aerodynamics performance of the small rotary wing system propeller. A sound knowledge of the underlying icing physics of the small rotary wing system propeller icing would greatly help researchers and engineers to understand the icing impact and develop effective anti-/de-icing techniques to allow the small UAS fly safely and efficiently. With this clearly objective, a series experiments were performed to study the dynamic icing process and the icing impact of the aerodynamic performance of the small UAS propeller. The Icing Research Tunnel located in the aerospace engineering department at Iowa State University were used to conducted experiments. It allows us to simulate different inflight icing conditions ranged from rime ice, mixed ice, to glaze ice by changing the temperatures (i.e., -4°C, -8°C, and -15°C) and liquid water content (0.5 g/m^3,1.0 g/m^3,1.5 g/m^3, and 2.0 g/m^3) inside of the wind tunnel. A high speed imaging system with “phase-locked” technique was used to obtain the dynamic ice accumulation process. In addition to the high speed image results, a high sensitive force transducer was used to measure the aerodynamic force generated from the rotating propeller. At the same time, the power

required to drive the dynamic system was recorded simultaneously with the image capture and the force recording during the ice accumulation process. The experimental results contained detailed ice structure information, and the variations of the aerodynamic force and power consumption during the ice accumulation, which helped us to understand the icing impact on small UAS propeller under different icing conditions.

6.2 Experimental setup for the measurements

The experiment was conducted in the ISU Icing Research Tunnel (ISU-IRT) operated by the Advanced Flow Diagnostic and Experimental Aerodynamic Laboratory at Iowa State University. The ISU-IRT is a closed loop wind tunnel with a cooling system and a spray system, which was used to conduct experimental studies on the icing related topics to explore the fundamental understanding of the icing physics of aircraft, wind turbine, power cable, small UAS propeller, as well as anti-/de-icing strategies. The cooling system provides the capabilities to low down the temperature inside of the wind tunnel as low as -25°C. And, the spray system has the potential to generate water droplets in different diameters range from 10 to 100μm. Thus, different icing phenomena could be simulated using this facility, such as, rime icing, mixed icing, and glaze icing. The wind tunnel has the potential to raise the wind speed as high as 60m/s. During the measurement, the propeller was driven by a brushless motor (i.e., dji 2212) with the power from a direct current power supply. The voltage of the DC power supply was kept at 11.1 V for all the measurements. The rotational speed of the propellers was controlled by the signal from a function generator via an electronic speed controller. During the measurement, a tachometer was used to detect the pre-marked blade to quantify the rotational speed of the propeller. Meanwhile, a pulse signal was generated and

was used to achieve “phase-locked” measurement. In order to make an accuracy adjustment of the rotational speed, a proportional-integral-derivative (PID) control was used. The experimental setup used in this propeller icing study was shown in Fig.2. The aerodynamic thrust was measured by a high-sensitivity force-moment sensor (JR3 load cell), which had a precision of ±0.1N (± 0.25% of the full range). In addition to the measurements of aerodynamic force, a high-speed camera (PCO Tech, pco.dimax S4) was used to obtain the images during the ice accretion period to identify the ice shape under different icing conditions and to explore the dynamic process of the ice formation. A digital delay generator was used in measurement to modify the pulse signal generated from the tachometer and sent the modified signal to the camera to achieve “phase-locked” imaging. The test conditions were listed in table 1. In order to simulate the forward flight condition, the pitch angle of the propeller was set at 10 degrees, and the rotational speed was adjusted to 4200RPM. The air speed inside of the wind tunnel was kept at 10m/s, which is a typical forward flight speed for small UAS. Three different temperatures (i.e., -4°C, -8°C, and -15°C) and four different liquid water contents (LWC) (i.e., 0.5 g/m^3,1.0 g/m^3,1.5 g/m^3, and 2.0 g/m^3) were used in the current study to investigate the different icing conditions.

Table 1 Icing test conditions

Incoming Flow Velocity (m/s)	**Propeller Pitch Angle (°)**	**Propeller Rotational Speed (RPM)**	**Temperature Inside of The Wind Tunnel (°C)**	**Liquid Water Content (g/m^3)**
10	**10**	**4200**	**-4**	**0.5, 1.0, 1.5, 2.0**
			-8	**0.5, 1.0, 1.5, 2.0**
			-15	**0.5, 1.0, 1.5, 2.0**

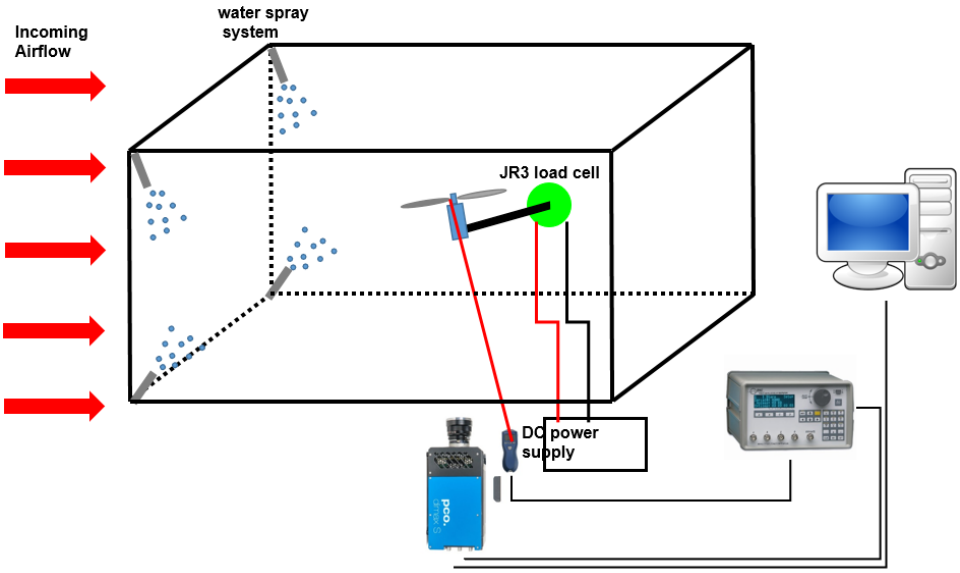

Fig. 2 Experimental setup for the icing study

6.3 Measurement results and discussions

6.3.1 General features of the rime ice and glaze ice formed on propeller

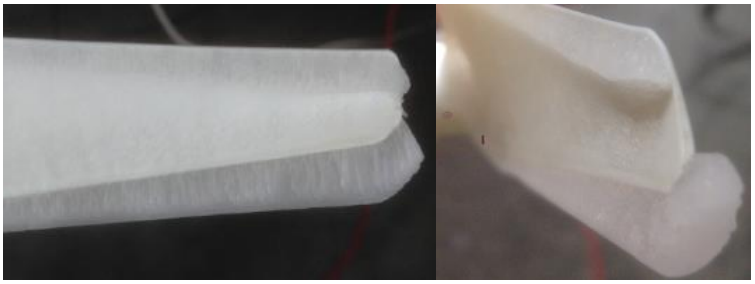

(a)rime ice

(b)glaze ice

Fig. 3 rime and glaze ice features

The general features of rime ice and glaze ice was shown in Fig.3. The ice at the leading edge can be easily identified from the figure no matter glaze ice or rime ice. Due to the large camber ratio, a typical feature of low Reynolds number airfoil, the flying water droplet direct impinged on the trailing edge at pressure side, which formed the trailing edge ice under both glaze and rime icing conditions. The rime ice formed on the propeller when the flying water droplets impinging on the blade with direct frozen process. As a result, the shape of the ice formed on propeller followed the geometry of the propeller, which can be found in Fig. 3 (a). The leading edge ice grew on the blade leading edge followed a linear relationship with the blade radius. The trailing edge ice grew toward the leading edge as the time developed. One thing should be mentioned is that the ice formed on the leading edge shows a sector distribution with respect to the leading edge. As mentioned before, after the flying water droplets impinged on the propeller, due to the released latent heat, part of the droplets will keep the water phase at warmer temperature. As a result, the glaze ice was formed, as shown in Fig. 3 (b). The glaze ice showed an irregular shape compared with the rime ice. Due to the centrifugal force and wind driven force, the ice grew toward the tip. Several “pin-shape” ice structures could be easily viewed at the tip and the trailing edge of the propeller. Although the trailing edge ice grew towards the leading edge, the “pin-shape” ice structures at the trailing edge grew back towards the leading edge under the wind driven force and bend to the tip due to the centrifugal force. Another feature could be identified from the figures was that the surface of the glaze ice was more rough than the rime ice.

6.3.2 Ice structure under different environmental conditions

Fig. 4 shows the final ice structure formed on the propeller under different temperatures and LWCs. The total icing time was 85 seconds for all the cases, which was decide by the case at ambient temperature equal to -4°C and LWC = 2.0 g/m³. In which case, the large amount of ice built upon the propeller surface dramatically increased the drag force. Thus, the 4200 RPM rotational speed cannot be maintained after 85 seconds. The final ice shape formed under warmer ambient temperature condition at -5°C was plotted in Fig. 4 (a). From top to the bottom, the LWC increased from 0 to 2.0 g/m³ with a 0.5 g/m³ increment. The LWC = 0 g/m³ means no ice condition. At LWC = 0.5 g g/m³, after 85 seconds, a thin ice layer was built on leading edge of the propeller. Due to the low value of the LWC, the ice layer was thin. The white color of the ice indicated that the ice accretion exhibited typical rime characteristics, which means the flying droplets directly froze on the propeller leading edge after impinging because the released latent heat cannot overcome the heat conduction and convection of the cooling process. Therefore, the geometry of the rime ice followed the leading edge of the propeller. As the LWC increased to 1.0 g/m³, under constant accumulation time, the ice layer was thickened and the ice color started to become transparent. The partial transparent ice color indicated that the ice type changed from rime to mixed. Since there was no rivulet formed, the ice shape still followed the propeller blade geometry. At this condition, part of the impinging droplets was kept at water phase due to the released latent heat. Under the centrifugal force and wind driven force, small amount of ice grew outside of the blade tip while major ice structure still followed the propeller geometry. As the LWC increased to 1.5 g/m³, there were more water droplet kept liquid phase than at LWC = 1.0 g/m³. Thus, more water was driven to the tip and formed ice there due to the

centrifugal force and wind driven force. The typical glaze ice was found at LWC = 2.0 g/m³. With this large LWC, more and more latent heat was released during icing process. The unfrozen water droplets formed rivulet and moved along the leading edge due to the influence of centrifugal force and wind driven force. At the blade tip, the “pin-shape” ice structure was formed, which grew outside of the tip and bent to the trailing edge direction. In addition to the leading edge, the “pin-shape” ice also formed at the trailing edge. One thing should be mentioned is that the trailing edge ice also formed at other LWC. The ice accumulated under -8°C ambient temperature was shown in Fig. 4 (b). At LWC equal to 0.5 and 1.0 g/m³, the structures of the accumulated ice on the leading edge were similar to the one formed at -4°C ambient temperature. The difference was the transparency of the ice accumulated at leading edge under LWC = 1.0 g/m³ were lower than those at -4°C. This is because of the effect of the heat conduction and convection could overcome more latent heat at -8°C than at -4°C ambient temperature. Due to the lower temperature of -8°C, at LWC = 1.0 g/m³, there was no ice grew towards the tip of the propeller blade compared to the case at same LWC and -4°C ambient temperature. At LWC = 1.5 g/m³, although the leading edge ice shape mainly followed the geometry of the leading edge, there was still a small amount of water run to the tip. As the LWC kept increasing to 2.0 g/m³, the “pin-shape” glaze ice also formed at the tip. However, due to the strong heat conduction and convection, the “pin-shape” ice structure did not grow as much as the one at -4°C ambient temperature. Fig. 4 (c) shows the ice structure results at ambient temperature of -15°C. As the temperature kept decreasing to -15°C, because of the released latent heat was moved quickly by the strong heat conduction and convection, the type of the ice formed on the propeller was rime ice at all different LWC conditions, which could be easily identified from the white ice color and

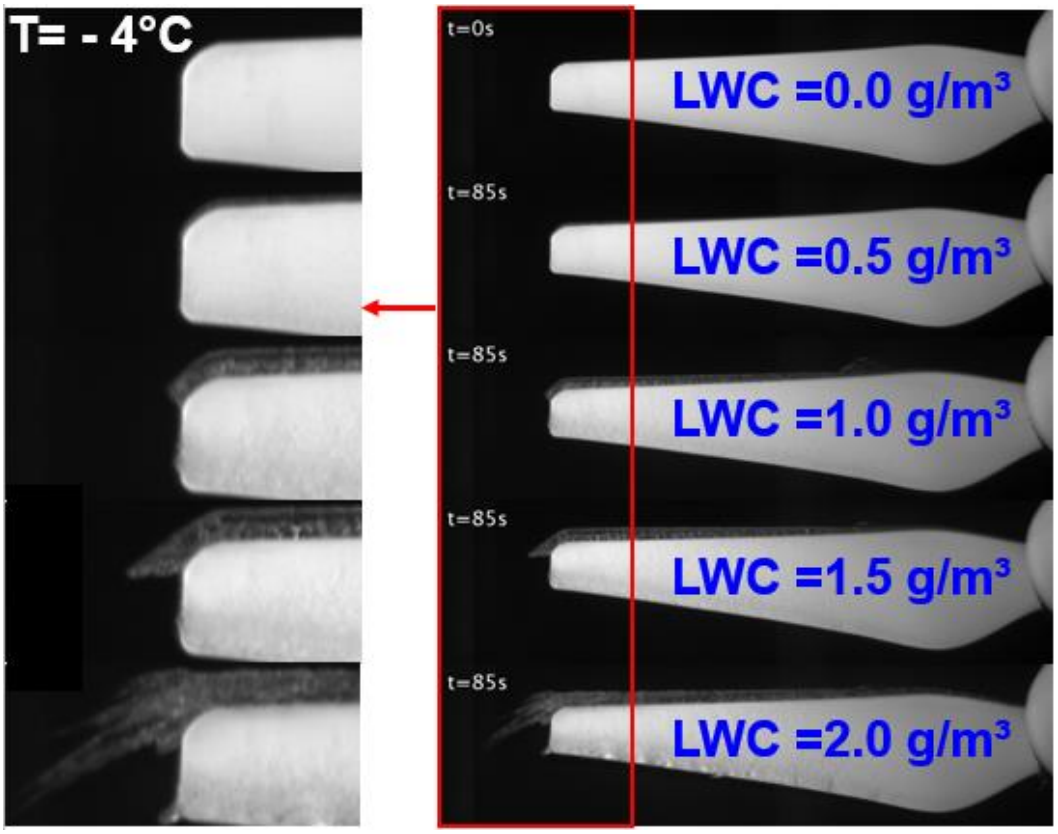
T= - 4°C
t=0s
LWC =0.0 g/m³
t=85s
LWC =0.5 g/m³
t=85s
LWC =1.0 g/m³
t=85s
LWC =1.5 g/m³
t=85s
LWC =2.0 g/m³

(a)

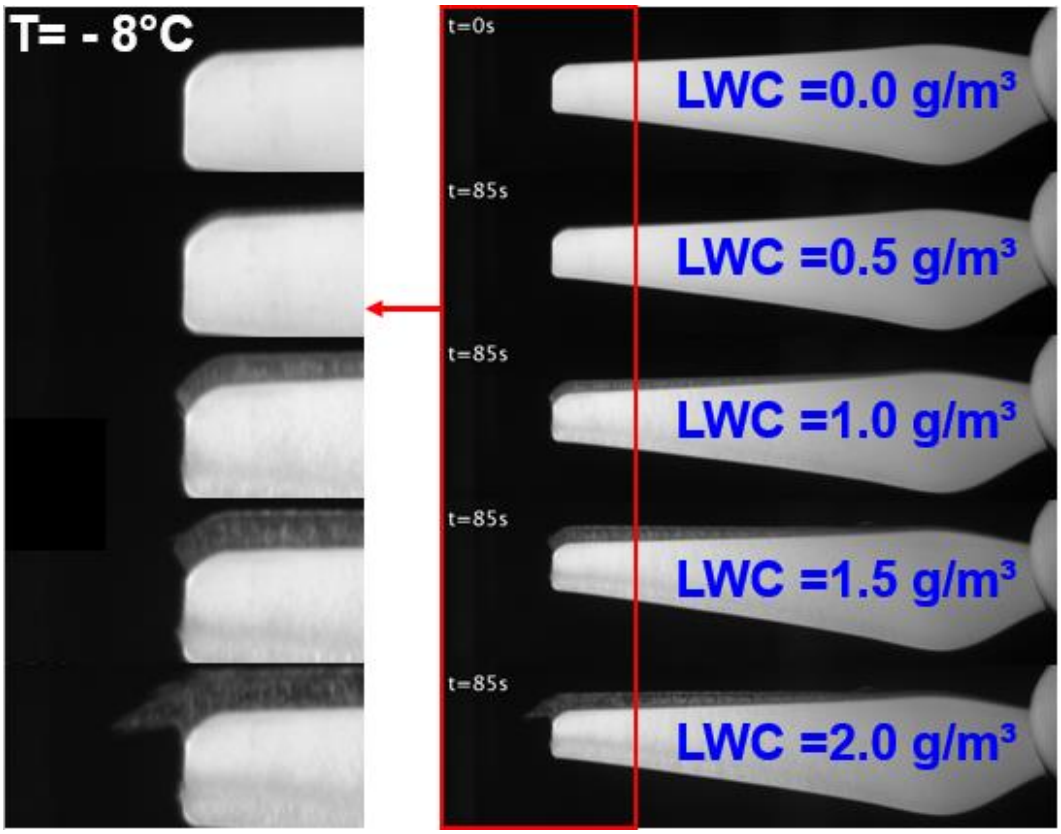
T= - 8°C
t=0s
LWC =0.0 g/m³
t=85s
LWC =0.5 g/m³
t=85s
LWC =1.0 g/m³
t=85s
LWC =1.5 g/m³
t=85s
LWC =2.0 g/m³

(b)

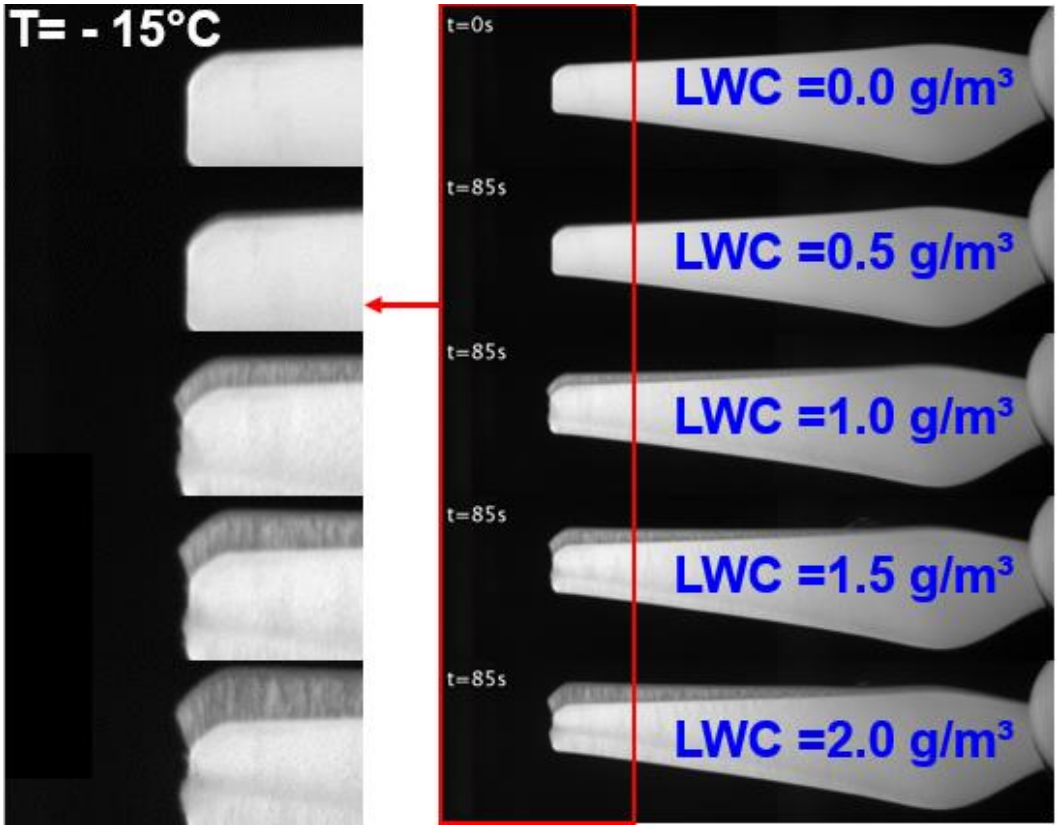

(c)

Fig. 4 The final ice structures

Table 2 ice type under different environmental conditions

		Liquid Water Content			
		0.5 g/m³	**1.0 g/m³**	**1.5 g/m³**	**2.0 g/m³**
Temperature	**-4°C**	**rime**	**mixed**	**glaze**	**glaze**
	-8°C	**rime**	**mixed**	**glaze**	**glaze**
	-15°C	**rime**	**rime**	**rime**	**rime**

the ice shape followed the geometry of the leading edge of the propeller blade. As the gain of the LWC the, more and more ice was built on the propeller. Table 2 shows the ice types under different conditions.

By detect the edge of the ice and the leading edge of the propeller the ice thickness can be determined. Fig. 5 shows the ice thickness along the propeller from 15% radius to

95% under different ambient temperature, different LWC, and 85 seconds accumulation. The non-dimensional leading edge ice thickness, Δ, is defined by

$$\frac{\Delta}{d} = A_c \cdot n \cdot \beta_0 \tag{1}$$

where d is the twice of the leading edge radius of the airfoil; n is the freezing fraction, which is 1 for immediately freeze after impinging, and 0 for no freezing; A_c is the accumulation parameter; β_0 is the collection efficiency of water droplets at the stagnation line[30].

The accumulation coefficient is defined as

$$A_c = \frac{LWC \cdot V_\infty \cdot \tau}{d \cdot \rho_{ice}} \tag{2}$$

where V_∞ is the freestream velocity, τ is the duration of the ice accumulation process, d is the doubled leading-edge radius of airfoil, and ρ_{ice} is the density of ice. When other parameters were kept constant, the ice accumulation parameter was linear varies with the LWC.

The freezing fraction is defined by

$$n = \frac{C_{p,water}}{\Lambda_f}\left(\Phi + \frac{\theta}{b}\right) \tag{3}$$

where $C_{p,water}$ is the specific heat of water at the surface temperature, Λ_f is the latent heat of freezing of water. The terms $\Phi, \theta,$ and b are water energy transfer parameter, air energy transfer parameter, and relative heat factor, respectively. These parameters were defined to be

$$\Phi = t_f - t_{st} - \frac{V_\infty{}^2}{2C_{p,water}} \tag{4}$$

$$\theta = \left(t_f - t_{st} - \frac{r {V_\infty}^2}{2C_{p,water}} \right) + \frac{h_G}{h_c} \left(\frac{\frac{p_{ws}}{T_{st}} - \frac{p_{tot}}{T_{tot}} \frac{p_{wa}}{p_{st}}}{\frac{1}{0.622} \frac{p_{tot}}{T_{tot}} - \frac{p_{ws}}{T_{st}}} \right) \Lambda_v \tag{5}$$

$$b = \frac{LWC \cdot \beta_0 \cdot C_{p,water}}{h_c} \tag{6}$$

the term r, h_G, and h_c are the recovery factor, gas-phase mass transfer coefficient and convective heat transfer coefficient, respectively, those are defined as

$$r = \sqrt{P_r} \tag{7}$$

$$h_G = \frac{h_c}{C_p} \left(\frac{P_r}{S_c} \right)^{0.67} \tag{8}$$

$$h_c = \frac{k_a}{d} N_u \tag{9}$$

The Prandtl number, Schmidt number, and Nusselt number were addressed as

$$P_r = \frac{C_p \cdot \mu}{k_a} \tag{10}$$

$$S_c = \frac{\mu}{\rho D_v} \tag{11}$$

$$N_u = 0.992 R_e^{0.5} \tag{12}$$

The collection efficiency of water droplets at the stagnation line is defined as

$$\beta_0 = \frac{1.4(K_0 - 0.125)^{0.84}}{1 + 1.4(K_0 - 0.125)^{0.84}} \tag{13}$$

where the modified inertia parameter, K_0, is defined as

$$K_0 = 0.125 + \frac{\lambda}{\lambda_{stokes}}(K - 0.125) \tag{14}$$

The λ/λ_{stokes} is a function of droplet Reynolds number, and is defined as

$$\frac{\lambda}{\lambda_{stoles}} = \left(0.8388 + 0.001482Re_\delta + 0.1847\sqrt{Re_\delta}\right)^{-1} \tag{15}$$

The inertia parameter, K, is defined as

$$K = \frac{MVD^2 \cdot V_\infty \cdot \rho_w}{18d\mu} \tag{16}$$

At rime ice and mixed ice conditions, the water directly freeze after impinging. Therefore, the freezing fraction was one. The combination of the accumulation parameter and collection efficiency of water droplets at the stagnation line increased linearly as the gain of velocity. For a rotating propeller, the relative velocity increased linearly from root to the tip. Therefore, at LWC equaled to 0.5 and 1.0 g/m³ environmental conditions, since the flight water droplet directly freeze on the surface after the impinging. The ice thickness increased linearly from root to tip, which can be easily viewed from the Fig 5 (a) and (b). Although the ambient temperatures were different, there were no difference of the ice thickness since the temperature difference did not affect the freezing fraction due to the directly frozen after impinging. Fig. 5 (c) represents the ice thickness at LWC = 1.5 g/m³. Under this LWC condition, when the ambient temperature equal to -15°C, the ice thickness represented a linear increase along the leading edge of the propeller since the ice formed under this condition was time ice. However, when the ambient temperature equal to -8°C, the released latent heat cannot be removed by the heat conduction and convection process. Thus, the ice thickness closed to the tip started to show a low value due to the change of the freezing

friction. When ambient temperature kept increased to -4°C, more water was kept liquid form, with the decreasing freezing friction, the ice thickness kept decreasing.

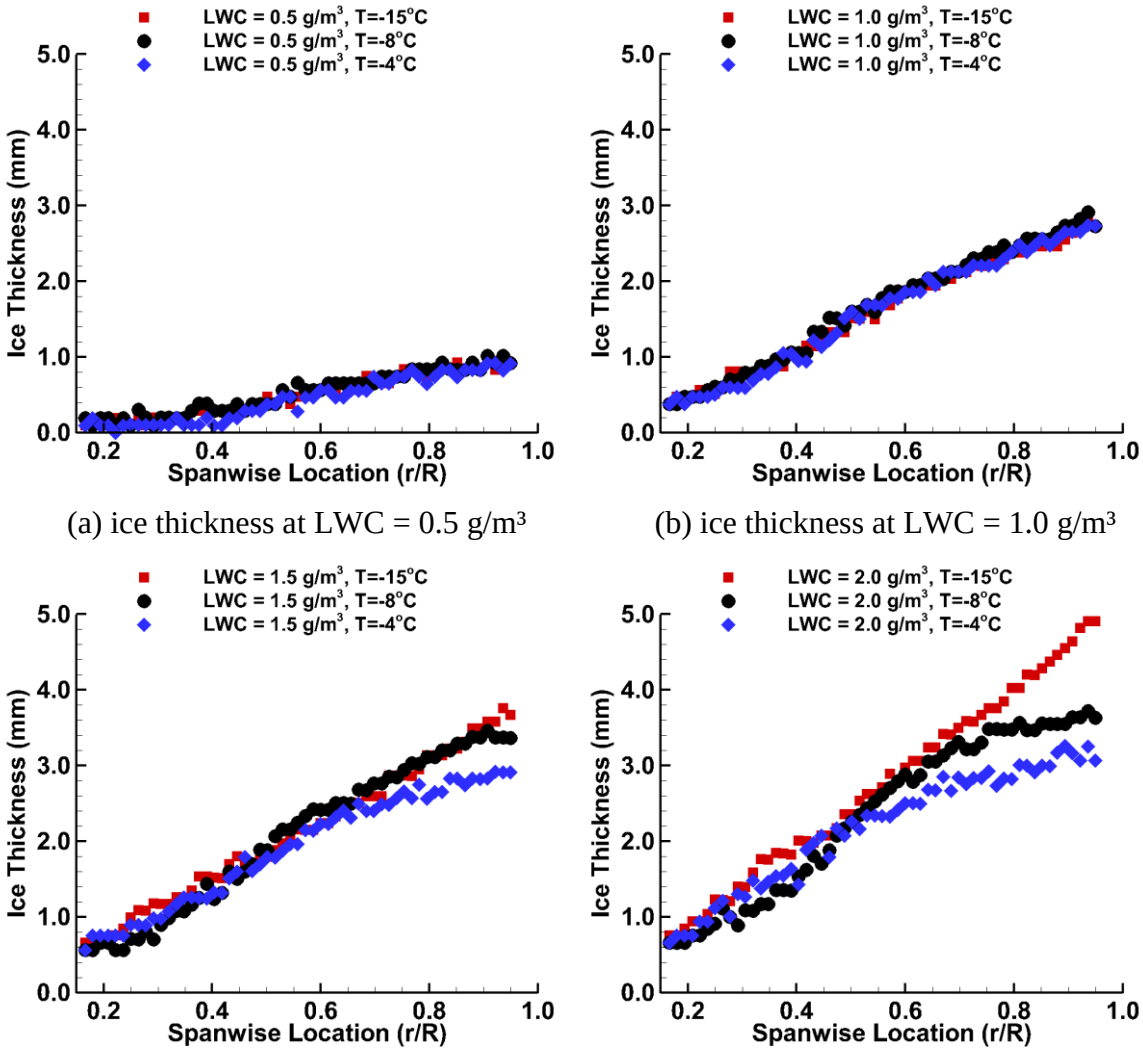

(a) ice thickness at LWC = 0.5 g/m³ (b) ice thickness at LWC = 1.0 g/m³

(c) ice thickness at LWC = 1.5 g/m³ (d) ice thickness at LWC = 2.0 g/m³

Fig. 5 Ice thickness along the propeller leading edge

6.3.3 Dynamic process of the icing accretion

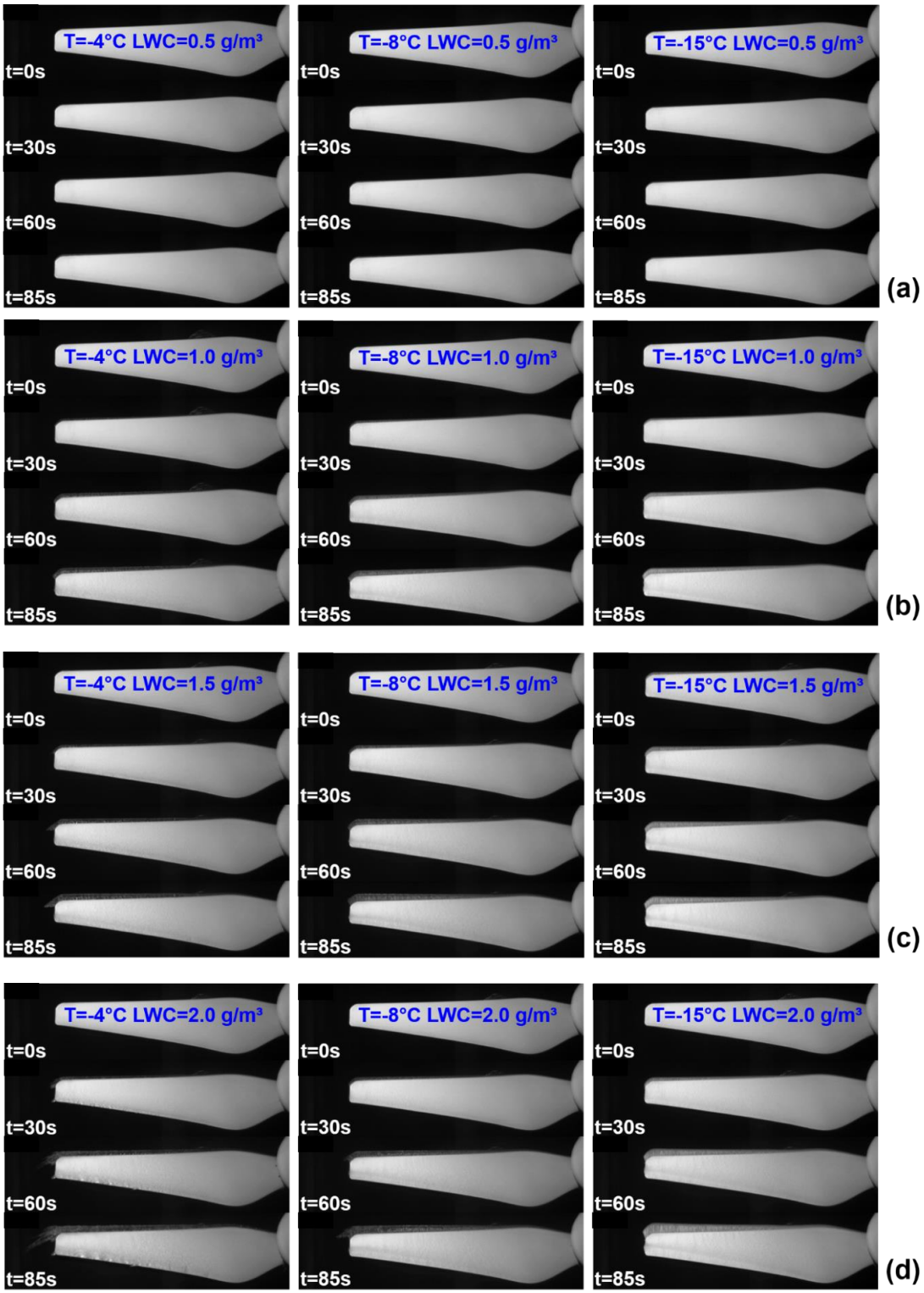

Fig. 6 Dynamic process of icing accretion

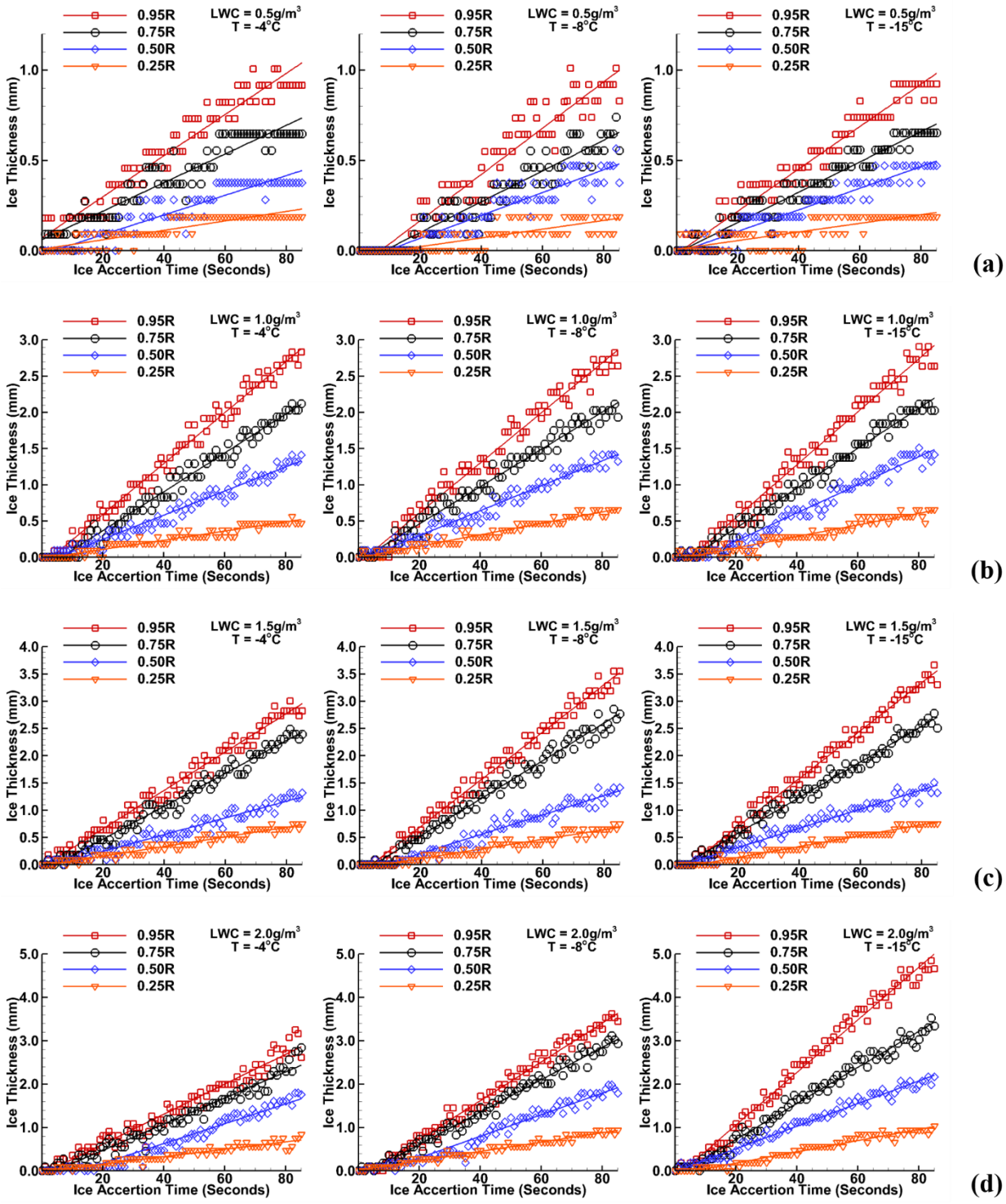

Fig. 7 Ice thickness vs accumulation time at different chord sections

The dynamic process of the icing accretion on the small UAS propeller under different icing conditions was explored by high speed imaging technique. As mentioned previously, the “phase-locked” technique helped us to obtain the time series images of the ice features on the propeller at a “frozen” location. Fig. 6 shows the high speed image results of the time evolution of the ice accretion over the propeller under different environmental conditions. At LWC equal to 0.5 g/m^3, a very thin ice layer was formed and the thickness increased with the gain of the ice accumulation time. However, the ice shape was not easily to observed by human eye from the image. Later, through image processing, a clearly growth rate will be given. Fig 6 (b) represents the dynamic process of the ice accumulation under 1.0 g/m^3 LWC, the ice thickness increased as the development of the time. However, the transparency of the ice did not change with the time. This indicate the time has no significant effect on the ice type. At same LWC and same accumulation time, the ice type was determined by the ambient temperature. The difference in the transparency of the ice color under different temperature could strongly support this conclusion. As the LWC increase to 1.5 g/m^3, beside the ice color change, a tip ice structure extension also can be viewed in Fig. 6 (c) at ambient temperature of -4°C. The tip ice structure appeared at very early stage, and grew larger as the time increasing. As the LWC kept increasing to 2.0 g/m^3, this phenomenon became more obvious. Through tracking the ice thickness at different chord section during the ice accretion process, the growth curve can be identified. In Fig 7 (a), at 0.5 g/m^3 LWC and -4°C ambient temperature, the ice thickness increased linearly as a function of time at all four different chord sections. The final ice thicknesses at 0.25R, 0.5R, 0.75 R and 0.95R were about 0.25mm, 0.5mm, 0.75mm, and 1.0mm, respectively. As the temperature decreased to -8°C and -15°C, the ice thickness at different section did not have significant change

compared with them at -4°C. This is mainly because that all of the flying water droplet directly frozen after the impinging at three different ambient temperatures, where the non-dimensional leading edge ice thickness parameter was only a function of time while other parameters were constant. When the LWC increased to 1.0 g/m^3, the ice thickness was larger compared to the lower LWC at four different chord sections, and still performed a linearly gain with respect to time. When compared the ice thickness under different temperature conditions, they were almost same. As the LWC kept increasing to 1.5 g/m^3, the increase of the ice thickness with respect to time was still linear at -15°C ambient temperature. Since there was no water transport, the ice thickness at four cross sections were almost same. At -4°C and -8°C, the water transport appeared, due to the small amount, the ice thickness was almost same at 0.25R, 0.5R, and 0.75R chord sections compared with -15°C temperature cases. However, the thickness of the ice decreased at 0.95R chord location because the centrifugal force and wind driven force drove the water rivulet to the tip and formed ice outward of the blade tip. Under constant LWC and duration time, the total amount of the water droplets impinging on the propeller blade were the same. At lower temperature, the impinging water directly frozen to ice, where the freezing friction was one. At warmer temperature, part of the water still kept the liquid phase and move toward the tip along the leading edge, where the freezing friction became smaller. Therefore, the smaller ice thickness at warmer temperature should be expected. At LWC = 2.0 g/m^3 and -15°C ambient temperature, the ice accumulated on the leading was rime ice, the linear relationship between ice thickness and accumulation time can be found in the plot. As temperature increased to -8°C and -4°C, the ice type changed from rime to glaze, the ice thickness decreased as the

temperature raise up at 0.75R and 0.95R chord location. This is mainly because of the temperature difference affect freezing fraction.

6.3.4 Influence of the ice accretion on aerodynamic performance and power consumption

In addition to the dynamic icing accretion process achieved by high speed imaging technique, the aerodynamic forces and power consumption has also been measured at a constant rotational speed and different environmental conditions. Fig. 8 shows the influence of the ice accretion on aerodynamic performance and power consumption. The power required to drive the propeller rotate at 4200RPM during under different LWC were normalized by the power under no ice condition at corresponding temperature. Same as the power results, the lift generated from the propeller under different LWC conditions has also been normalized by the lift value at no ice condition and certain temperature. One general feature of the power curve is that, under same temperature and LWC, more and more power was needed to maintain the rotational speed with the time developed due to the ice accumulated on the propeller was a function of time. At the same time, the lift ratio decreased as the development of the time under same temperature and LWC. Fig 8 (a) represents the power ratio versus ice accumulation time at ambient temperature of -4°C and different LWC range from 0.5 to 2.0 g/m³ with an increment of 0.5 g/m³. The power curve shows a quadratic form. As the gain of the LWC, the power consumption was increased at the same ice accretion time. For example, at 85 seconds, LWC = 2.0 g/m³, the power required to maintain the rotation increased to almost 5 times of power consumption at no ice condition. The lift ratio at ambient temperature of -4°C and different LWC range from 0.5 to 2.0 g/m³

was shown in Fig. 8 (b). As indicated by the red line, the lift generated from the propeller decreased to 94% of the no ice condition after 85 seconds ice accumulation. One interesting phenomenon is that the lift ratio curve of the LWC of 1.0, 1.5, and 2.0 g/m³ show a similar decay rate, which was not same as what we expect. The detailed explanation for the possible reason will perform later. The power ratio and lift ratio results at -8°C ambient temperature were plotted in Fig. 8 (c) and (d). The power ratio results at LWC of 0.5, 1.0, and 1.5 g/m³ shows a very similar results as they were at -4°C ambient temperature. The power ratio results at 2.0 g/m³ LWC shows a very similar trend with a maximum value reduction compared with that at -4°C. The lift ratio at LWC of 0.5, 1.0 g/m³ were almost the same as lift ratio at -4°C ambient temperature. When the LWC equal to 1.5 g/m³, the lift ratio decreased to 84% of the no ice condition at -8°C. As the LWC kept increased to 2.0 g/m³, the lift ratio curve grew back with a minimum value of 88%. Fig. 8 (e) and (f) represents the power and lift ratio at -15°C ambient temperature, respectively. As the increasing of the LWC, the power consumption increased up to 190% and the lift generated from the propeller reduced to 81%.

One interesting phenomena was that the power consumption increase linearly at rime ice and mixed ice conditions, and the gain of the power consumption revealed a quadratic trend under glaze ice condition. It is well known the power equals to the torque times angular velocity. Under constant rotational speed, the linear increase of the power means the torque increase linearly with the time. For glaze ice the spanwise length also increase as a function of time. Therefore, the power consumption of glaze ice condition increased as a function of the square of time, which results in a quadratic trend. Another interesting phenomena was the lift ratio kept the same under glaze ice conditions with different LWCs and temperatures.

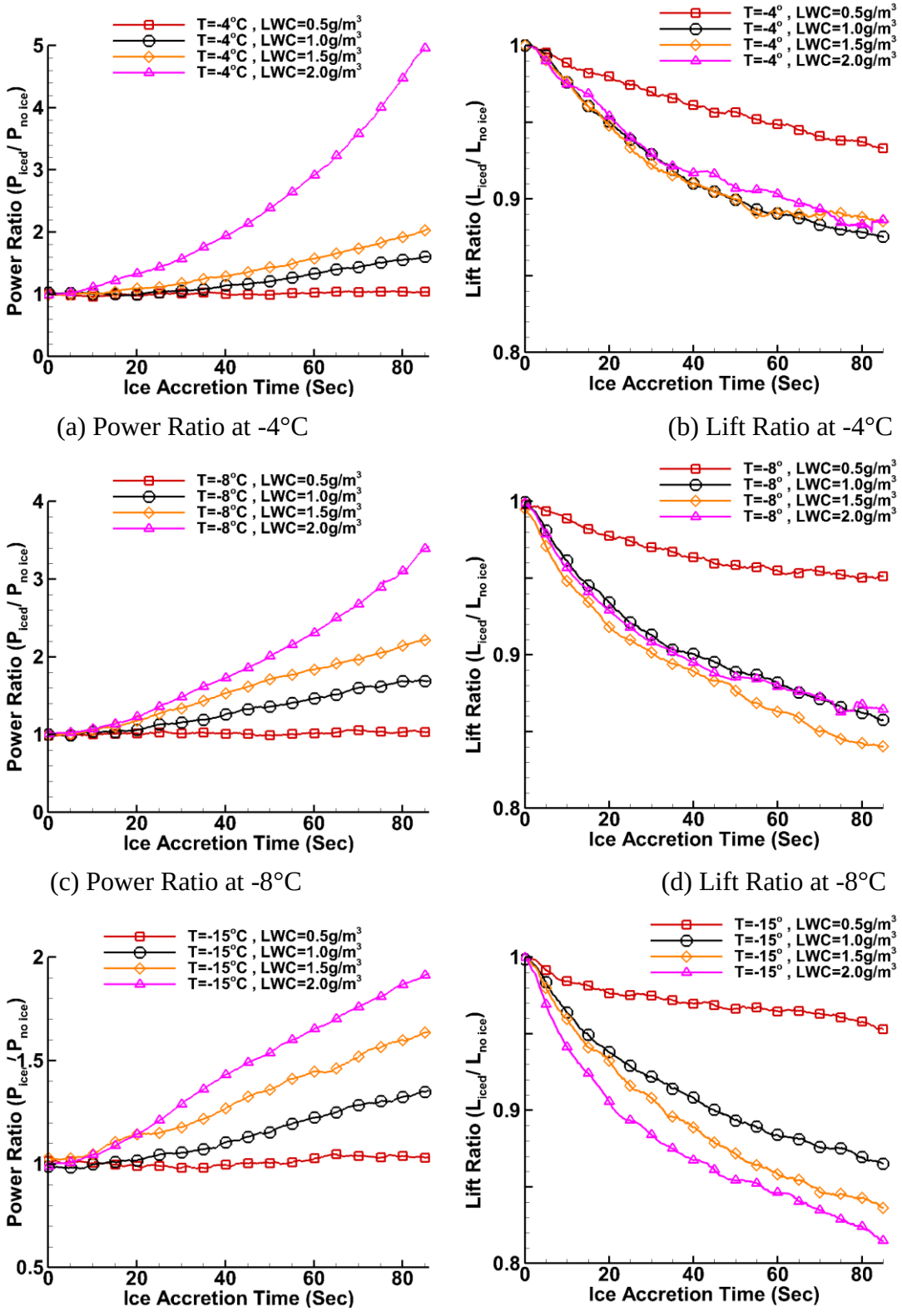

(a) Power Ratio at -4°C (b) Lift Ratio at -4°C

(c) Power Ratio at -8°C (d) Lift Ratio at -8°C

(e) Power Ratio at -15°C (f) Lift Ratio at -15°C

Fig. 8 Influence of the Ice Accretion on Aerodynamic Performance and Power Consumption

There are two possible reason lead to this unchanged lift ratio. First of all, the extend “pin-shape” leading edge ice change the planform and increase the radius of the propeller. After the ice formed the tip shape was similar to the “Ogee Tip”[31], as shown in Fig. 9. This extend tip change the tip vortex formation process and extend the location where the tip vortex formed. At the original propeller tip region, there was a tip loss due to the tip vortex formation. After the “pin-shape” leading edge ice formed, there was more lift generated at the propeller tip region. Secondly, the “pin-shape” has an ellipse shape in cross section. Due to the positive angle of attack between chord length of the cross section and the incoming flow direction, there was lift has been generated.

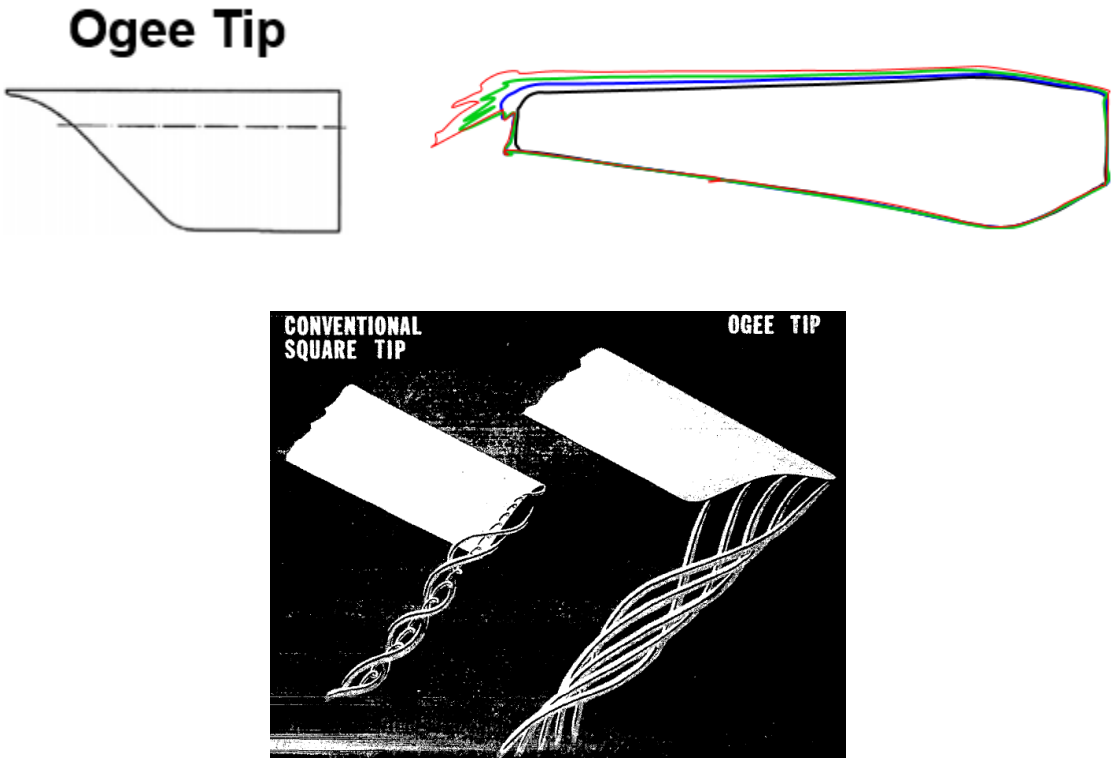

Fig. 9 New propeller planform after ice arrection and ogee tip

6.4 Conclusion

In the current study, a series experiments were conducted to investigate the ice accumulation on a small UAS propeller, and the icing impact of the aerodynamic performance. All of the experiments were conducted in the Icing Research Tunnel located in the aerospace engineering department at Iowa State University. With this functional wind tunnel, different icing conditions can be simulated ranged from rime ice, mixed ice, to glaze ice by varying the temperatures (i.e., -4°C, -8°C, and -15°C) and liquid water content (0.5 g/m^3,1.0 g/m^3,1.5 g/m^3, and 2.0 g/m^3). The detailed dynamic ice accumulation process was obtained through high speed imaging system with "phase-locked" technique. In addition, the aerodynamic force generated from the rotating propeller was measured by a high sensitive force transducer, JR3 load cell. Meanwhile, the power consumption was recorded simultaneously with the force measurement and the image capture during the ice accumulation process. Those measurement results provided us sufficient detailed information on the ice structure changes, and force and power variations during the ice accumulation process, and helped us to get a better understand about the icing impact on small UAS propeller under different icing conditions.

The high speed imaging results revealed the ice structures and ice accumulation processes under different icing conditions. When the small UAS propeller operated under rime ice or mixed ice conditions, the ice accumulated on the propeller leading edge followed the leading edge geometry very well. When the small UAS propeller operated under glaze ice conditions, due to the water runback caused by the centrifugal force and wind driven force, a "pin-shape" ice structure formed and grew outside of the tip of the propeller and bent to the trailing edge direction. At the same time, due to the large camber ratio, the flying water

droplets impinged on the trailing edge and formed trailing edge ice. It was also found that the ice thickness increased linearly along the leading edge under rime ice and mixed ice conditions and did not affected by the temperature. At the glaze ice condition, the thickness of the ice was smaller compared to the other two ice conditions because the total amount of the impinging water was the same under constant LWC condition and part of the unfrozen water was drove towards the tip due to centrifugal force and wind driven force. From time perspective, the ice thickness grew linearly under all icing conditions and all chord sections.

The power measurement results illustrated that the ice formed on the propeller would increase the power consumptions in order to maintain the constant rotational speed. Under the rime ice and mixed ice conditions, the power consumptions increased linearly as a function of time, as well as a function of LWC. At LWC = 2.0 g/m³ and ambient temperature of -15°C, the power needed to drive the motor increased to 200%. When the glaze ice formed on the propeller, the increasing of the power consumptions showed a quadratic trend as a function of time. At LWC = 2.0 g/m³ and ambient temperature of -4°C, the power consumption was 5 times of the one at no ice condition.

The lift ratio comparison results demonstrated that the aerodynamics performance of the propeller would be affected by the ice accumulation. At the rime ice and mixed ice conditions, the lift ratio decreased as a function of LWC and time. The maximum lift degradation was 19% compared with the one at no ice condition. However, the lift ratio was not affected by the LWC under glaze ice condition because the extended ice structure increased the aerodynamic areas and modified the tip vortex formation.

References

[1] Floreano, D., and Wood, R., "Science,technology and the future of small autonomous drones," *Nature*, vol. 521(7553), 2015, pp. 460–466.

[2] Appiah-Kubi, P., Martos, B., Atuahene, I., and William, S., "U.S. inflight icing accidents and incidents, 2006 to 2010," *IIE Annual Conference and Expo 2013*, 2013.

[3] BRAGG, M. B., GREGOREK, G. M., and LEE, J. D., "Airfoil aerodynamics in icing conditions," *Journal of Aircraft*, vol. 23, 1986, pp. 76–81.

[4] Narducci, R., and Kreeger, R., "Analysis of a Hovering Rotor in Icing Conditions," *66th Annual Forum and Technology Display (AHS Forum 66)*, 2010, pp. 1–16.

[5] BRITTON, R., and BOND, T., "A review of ice accretion data from a model rotor icing test and comparison with theory," *29th Aerospace Sciences Meeting*, 1991.

[6] Cao, Y., "Helicopter flight characteristics in icing conditons," *The aeronautical journal*, vol. 116, 2012, pp. 963–979.

[7] Palacios, J. L., Han, Y., Brouwers, E. W., and Smith, E. C., "Icing Environment Rotor Test Stand Liquid Water Content Measurement Procedures and Ice Shape Correlation," *Journal of the American Helicopter Society*, 2012.

[8] Fortin, G., and Perron, J., "Spinning Rotor Blade Tests in Icing Wind Tunnel," *1st AIAA Atmospheric and Space Environments Conference*, 2009, pp. 1–16.

[9] Papadakis, M., Rachman, A., Wong, S., Yeong, H., and Bidwell, C. S., "Water Droplet Impingement on Simulated Glaze , Mixed , and Rime Ice Accretions," *Nasa/Tm-2007-213961*, 2007.

[10] Cao, Y., and Chen, K., "Helicopter icing," *Aeronautical Journal*, vol. 114, 2010, pp. 83–90.

[11] R.W.Gent; N.P.Dart; and J.T. Cansdale, "Aircraft Icing," *The royal society*, 2000, pp. 1–108.

[12] Ueno, K., and Farzaneh, M., "Linear stability analysis of ice growth under supercooled water film driven by a laminar airflow," *Physics of Fluids*, vol. 23, 2011, pp. 1–40.

[13] Fortin, G., Laforte, J. L., and Ilinca, A., "Heat and mass transfer during ice accretion on aircraft wings with an improved roughness model," *International Journal of Thermal Sciences*, vol. 45, 2006, pp. 595–606.

[14] Liu, Y., and Hu, H., "An Experimental Investigation on the Convective Heat Transfer Process over an Ice Roughened Airfoil," *54th AIAA Aerospace Sciences Meeting*, vol. 2, 2016, pp. 1–31.

[15] Liu, Y., Chen, W. L., Bond, L. J., and Hu, H., "An experimental study on the characteristics of wind-driven surface water film flows by using a multi-transducer ultrasonic pulse-echo technique," *Physics of Fluids*, vol. 29, 2017.

[16] Han, Y., and Palacios, J., "Transient Heat Transfer Measurements of Surface Roughness due to Ice Accretion," *6th AIAA Atmospheric and Space Environments Conference*, 2014, pp. 1–22.

[17] Korkan, K. D., Dadone, L., and Shaw, R. J., "Performance Degradation of Helicopter Rotor in Forward Flight due to Ice," *J. AIrcraft*, vol. 22, 1985, pp. 713–718.

[18] Korkan, K. D., Dadone, L., and Shaw, R. J., "Helicopter Rotor Performance Degradation in Natural Icing Encounter," *Jorunall of Aircraft*, vol. 21, 1984, pp. 84–85.

[19] Han, Y., and Palacios, J., "Analytical and Experimental Determination of Airfoil Performance Degradation Due to Ice Accretion," *4th AIAA Atmospheric and Space Environments Conference*, 2012, pp. 1–25.

[20] COFFMAN, JR., H., "Review of helicopter icing protection systems," *Aircraft Design, Systems and Technology Meeting*, 1983.

[21] Palacios, J. L., Assistant, R., Engineering, A., Smith, E. C., Gao, H., and Rose, J. L., "Ultrasonic Shear Wave Anti-Icing System for Helicopter Rotor Blades," *Stress: The International Journal on the Biology of Stress*, 2006.

[22] Schutzius, T. M., Jung, S., Maitra, T., Eberle, P., Antonini, C., Stamatopoulos, C., and Poulikakos, D., "Physics of icing and rational design of surfaces with extraordinary icephobicity," *Langmuir*, vol. 31, 2015, pp. 4807–4821.

[23] Zhou, W., Liu, Y., Hu, H., Hu, H., and Meng, X., "Utilization of Thermal Effect Induced by Plasma Generation for Aircraft Icing Mitigation," *AIAA Journal*, vol. 56, 2018, pp. 1–8.

[24] Thomas, S. K., Cassoni, R. P., and MacArthur, C. D., "Aircraft anti-icing and de-icing techniques and modeling," *Journal of Aircraft*, vol. 33, 1996, pp. 841–854.

[25] Liu, Y., Li, L., Li, H., and Hu, H., "An experimental study of surface wettability effects on dynamic ice accretion process over an UAS propeller model," *Aerospace Science and Technology*, vol. 73, 2018, pp. 164–172.

[26] Li, Li., Ning, Z., and Hu, H., "An Experimental Study on the Transient Ice Accretion Process over a Rotating UAV Propeller," *55th AIAA Aerospace Sciences Meeting*, 2017, pp. 1–18.

[27] Liu, Y., Li, L., Ning, Z., Tian, W., and Hu, H., "Experimental Investigation on the Dynamic Icing Process over a Rotating Propeller Model," *AIAA Journal of Power and Propulsion*, 2018, pp. 1–15.

[28] Green, S. D., "A Study of U.S.Inflight Icing Accidents and Incidents,1978 to 2002," *44th AIAA Aerospace Sciences Meeting and Exhibit*, 2006.

[29] Szilder, K., and McIlwain, S., "In-flight icing of UAVs - The influence of flight speed coupled with chord size," *Canadian Aeronautics and Space Journal*, vol. 58, 2012, pp. 83–94.

[30] Anderson, D., and Tsao, J., "Evaluation and validation of the messinger freezing fraction," *Working Paper*, 2005, p. 18.

[31] Mantay, W. R., Campbell, R. L., and Shidler, P. A., "Full-scale testing of an OGEE tip rotor," 1978.

CHAPTER 7

SUMMARY AND CONCLUSIONS

The major accomplishments of this dissertation were summarized in this section. Over all, the aerodynamic and aeroacoustic characteristics of the small UAS has been studied experimentally. During the measurements, the high accuracy force and momentum transducer was used to characterize the aerodynamics thrust generated from the propeller. The sound measurement was conducted in the anechoic chamber to explore the sound pressure level at human ear hearing range. In addition, PIV techniques was used to obtained the detailed flow structure in the wake to quantify the velocity, vorticity, and turbulent kinetic energy. There are five topics covered in this dissertation.

First of all, the aerodynamics thrust and wake characteristics of small UAS propeller has been studied experimentally. The aerodynamic thrust measurement results clearly illustrated that the mean thrust generated from the propeller increased as a function of rotational speed with a quadratic trend. At the same time, the thrust perturbation increased with the gain of the rotational speed. The FFT analysis results explained that the increase of the thrust perturbation is mainly caused by the two blade configuration since the fluctuation of thrust at first and second harmonics of the blade passing frequency raised as the rotational speed increase. The ensemble-average flow quantities (e.g., mean velocity and mean vorticity) of the propeller wake were obtained through “free-run” PIV measurements. Three typical flow regions: quiescent flow region, inflow region, and induced flow region, were explored. The development of the induced velocity was also obtained through this measurement. The periodic velocity drop at the slipstream boundary was captured by “phase-locked” PIV

measurements, which due to the tip vortex formation. The core structure of the tip vortices was observed in the vorticity measurement results. In addition to the tip vortices, the positive and negative vortices due to the flow passing the trailing edge also has been viewed, which was associated with the “strip shape” low speed region due to the blade cut-in. By tracking the location of the tip vortices and vortex sheet, the travelling speeds and the slipstream boundary were achieved. Another important finding was the evolution of the tip vortices interaction. Due to the diffusion and the interaction between tip vortex and vortex sheet, the clearly roll-up motion of the tip vortices interaction started at the downstream about 0.7R. The dynamic process of the interaction from phase angle 0° to 300° was detailed explained. Finally, the previous tip vortex merge with the incoming vortex and dissipated.

Secondly, the Saw-tooth serrated trailing edge has been applied to small UAS propeller to investigate the noise reduction effect on the turbulent boundary layer trailing edge noise. The sound pressure level spectrum measurement results indicated that the saw-tooth serrated trailing edge restrict the total noise emission by decreasing the noise level at high frequencies and maintaining the noise level at low frequencies. It was found that larger serrations resulted in better noise attenuation effects compared to the smaller serration. The comparison results of the force measurements between baseline and serrated trailing edge propellers proved that the saw-tooth serration had no significant effect on the thrust generation. The flow-filed measurement results revealed that the serrated trailing propellers generated almost identical mean flows at hover-flight conditions when compared to the baseline propeller. However, the serrations did significantly influence the flow passing over the trailing edge.

In addition, the bio-inspire propeller was investigated to improve the aerodynamic performance and reduce noise. The force measurement results revealed that the bio-inspired propeller could generated same thrust as the baseline propeller under same power input. However, the rotational speed of bio-inspired propeller was slower than baseline at hover flight condition. The sound measurement results indicated that the bio-inspired propeller could reduce noise up to 4dB compared to baseline propeller at hover motion. Through PIV measurements, the velocity and vorticity distribution in the downstream are obtained. Compared with baseline, the bio-inspired propeller generated a smaller wake region and demonstrated a faster decay rate of the tip vortex strength.

Beyond the isolated propeller studies, the rotor to rotor interaction has been studied to illustrate how does the separation distance affect the thrust generation and noise emission. It was found that, while the separation distance had a negligible effect on the thrust coefficient of the rotor (i.e., variation within 2% for all test cases), the thrust fluctuations (i.e., thrust standard deviation) were found to increase dramatically as the separation distance became smaller. More specifically, the measured thrust fluctuations for the twin-rotor case (i.e., L= 0.05D) were found to be ~2.4 times larger than that of the baseline case. This is believed to be caused by the complex flow interactions within rotors as revealed by the detailed PIV measurements. It was also found that the noise distribution for the twin-rotor case is a function of both azimuthal angle and separation distance, where the measured noise was found to increase as the azimuthal angle increased from 90° (i.e., side position) to 180° (i.e., right ahead the rotors), and to increase as the separation distance reduced from L = 1.0D to L = 0.05D. A maximum noise enhancement of ~3 dB was recorded for the L = 0.05D case in

comparison to that of the $L = 1.0D$ case, which is the result of both tonal and broadband noise augmentations as indicated in the sound spectrum analysis.

As shown quantitatively from the planar PIV and Stereoscopic PIV measurement results, the induced flow behind the rotors was found to contract radially toward the axis of the rotor as the flow convected downstream. For the single rotor case, while most of the regions in the wake were devoid of flow structures, only the region near the blade tips was characterized by elevated in-plain TKE (i.e., in *X*-*Z* plane) due to periodic tip vortex shedding. A similar phenomenon was observed for the twin-rotor case, except that the TKE region was significantly higher at the top-right area than that of single rotor case. Due to the resultant effect of upwash and radial flows in the near wake of the twin-rotor case, a region with a flow separation was identified in the *X*-*Y* cross plane, which led to significantly higher TKE distributions and thrust fluctuations behind the twin rotors. It should also be noted that the velocity field for the twin-rotor case was found to be attracted and bent toward the nearby rotor due to the Coanda effect.

In general, the measured quantitative results given in the present study are believed to be very beneficial in understanding how rotor-rotor interactions affect the aerodynamic and aeroacoustic performances of small UAVs. It depicted a vivid picture regarding the complex flow features behind the rotors, which further explained their correlations with the enhanced force fluctuations and noise levels. Such quantitative information is highly desirable to elucidate the underlying physics pertinent to rotor interactions, and to explore/optimize design paradigms for better commercial UAV designs.

Last of the all, the small UAS propeller icing physics and the icing impact on the aerodynamic performance has been detailed studied. The high speed imaging results revealed

the ice structures and ice accumulation processes under different icing conditions. When the small UAS propeller operated under rime ice or mixed ice conditions, the ice accumulated on the propeller leading edge followed the leading edge geometry very well. When the small UAS propeller operated under glaze ice conditions, due to the water runback caused by the centrifugal force and wind driven force, a “pin-shape” ice structure formed and grew outside of the tip of the propeller and bent to the trailing edge direction. At the same time, due to the large camber ratio, the flying water droplets impinged on the trailing edge and formed trailing edge ice. It was also found that the ice thickness increased linearly along the leading edge under rime ice and mixed ice conditions and did not affected by the temperature. At the glaze ice condition, the thickness of the ice was smaller compared to the other two ice conditions because the total amount of the impinging water was the same under constant LWC condition and part of the unfrozen water was drove towards the tip due to centrifugal force and wind driven force. From time perspective, the ice thickness grew linearly under all icing conditions and all chord sections.

The power measurement results illustrated that the ice formed on the propeller would increase the power consumptions in order to maintain the constant rotational speed. Under the rime ice and mixed ice conditions, the power consumptions increased linearly as a function of time, as well as a function of LWC. At LWC = 2.0 g/m³ and ambient temperature of -15°C, the power needed to drive the motor increased to 200%. When the glaze ice formed on the propeller, the increasing of the power consumptions showed a quadratic trend as a function of time. At LWC = 2.0 g/m³ and ambient temperature of -4°C, the power consumption was 5 times of the one at no ice condition.

The lift ratio comparison results demonstrated that the aerodynamics performance of the propeller would be affected by the ice accumulation. At the rime ice and mixed ice conditions, the lift ratio decreased as a function of LWC and time. The maximum lift degradation was 19% compared with the one at no ice condition. However, the lift ratio was not affected by the LWC under glaze ice condition because the extended ice structure increased the aerodynamic areas and modified the tip vortex formation.

REFERENCES

[1] Floreano, D., and Wood, R. J., "Science, technology and the future of small autonomous drones," *Nature*, vol. 521, 2015, pp. 460–466.

[2] BI INTELLIGENCE, "The Drones Report: Research, Use Cases, Regulations, and Issues - Business Insider" Available: http://www.businessinsider.com/the-drones-report-research-use-cases-regulations-and-issues-2016-4-28.

[3] Freeman, P. K., and Freeland, R. S., "Agricultural UAVs in the U.S.: Potential, policy, and hype," *Remote Sensing Applications: Society and Environment*, vol. 2, 2015, pp. 35–43.

[4] Malveaux, C., Hall, S., and Price, R. R., "Using drones in agriculture: Unmanned aerial systems for agricultural remote sensing applications," *American Society of Agricultural and Biological Engineers Annual International Meeting 2014*, vol. 6, 2014, pp. 4075–4079.

[5] Lindsey, Q., Mellinger, D., and Kumar, V., "Construction with quadrotor teams," *Autonomous Robots*, vol. 33, 2012, pp. 323–336.

[6] Mirjan, A., Augugliaro, F., D'Andrea, R., Gramazio, F., and Kohler, M., "Building a Bridge with Flying Robots," *Robotic Fabrication in Architecture, Art and Design 2016*, 2016, pp. 34–47.

[7] Leishman, J. G., *Principles of helicopter aerodynamics*, Cambridge University Press, 2006.

[8] Bouabdallah, S., Noth, A., and Siegwart, R., "PID vs LQ control techniques applied to an indoor micro quadrotor," *2004 IEEE/RSJ International Conference on Intelligent Robots and Systems (IROS) (IEEE Cat. No.04CH37566)*, vol. 3, 2004, pp. 2451–2456.

[9] Madani, T., and Benallegue, A., "Backstepping Control for a Quadrotor Helicopter," *Intelligent Robots and Systems, 2006 IEEE/RSJ International Conference on*, 2006, pp. 3255–3260.

[10] Castillo, P., Lozano, R., and Dzul, A., "Stabilization of a Mini Rotorcraft with Four Rotors," *IEEE Control Systems*, vol. 25, 2005, pp. 45–55.

[11] Raffo, G. V., Ortega, M. G., and Rubio, F. R., "An integral predictive/nonlinear H∞ control structure for a quadrotor helicopter," *Automatica*, vol. 46, 2010, pp. 29–39.

[12] Huang, H., Hoffmann, G. M., Waslander, S. L., and Tomlin, C. J., "Aerodynamics and control of autonomous quadrotor helicopters in aggressive maneuvering," *Proceedings - IEEE International Conference on Robotics and Automation*, 2009, pp. 3277–3282.

[13] Achtelik, M., Tianguang Zhang, Kuhnlenz, K., and Buss, M., "Visual tracking and control of a quadcopter using a stereo camera system and inertial sensors," *2009 International Conference on Mechatronics and Automation*, IEEE, 2009, pp. 2863–2869.

[14] Ditmer, M., Vincent, J., Werden, L., Tanner, J., Laske, T., Iaizzo, P., Garshelis, D., and Fieberg, J., "Bears Show a Physiological but Limited Behavioral Response to Unmanned Aerial Vehicles," *Current Biology*, vol. 25, Aug. 2015, pp. 2278–2283.

[15] Hoffmann, G., Huang, H., and Waslander, S., "Quadrotor helicopter flight dynamics and control: Theory and experiment," *American Institute of Aeronautics and Astronautics*, 2007, pp. 1–20.

[16] Lopez, O. D., Escobar, J. A., and Pérez, A. M., "Computational Study of the Wake of a Quadcopter Propeller in Hover," *23rd AIAA Computational Fluid Dynamics Conference*, 2017, pp. 1–9.

[17] Liu, J., and Luo, S., "Navier-Stokes Equations based Flow Simulations of Low Reynolds Number Propeller for Unmanned Aerial Vehicle," *55th AIAA Aerospace Sciences Meeting*, 2017, pp. 1–13.

[18] Khan, W., Caverly, R., and Nahon, M., "Propeller slipstream model for small unmanned aerial vehicles," *AIAA Modeling and Simulation Technologies (MST) Conference*, 2013.

[19] Yoon, S., Lee, H. C., and Pulliam, T. H., "Computational Analysis of Multi-Rotor Flows."

[20] Intaratep, N., Alexander, W. N., Devenport, W. J., Grace, S. M., and Dropkin, A., "Experimental Study of Quadcopter Acoustics and Performance at Static Thrust Conditions," *22nd AIAA/CEAS Aeroacoustics Conference*, 2016.

[21] Marte, J. E., and Kurtz, D. W., "A Review of Aerodynamic Noise from Propellers, Rotors and Lift Fans," *Nasa Cr-107568*, vol. Technical, 1970.

[22] Gruber, M., Joseph, P. F., and Chong, T. P., "Experimental investigation of airfoil self noise and turbulent wake reduction by the use of trailing edge serrations," 2010.

[23] Gruber, M., Joseph, P., and Chong, T., "On the mechanisms of serrated airfoil trailing edge noise reduction," *17th AIAA/CEAS Aeroacoustics Conference (32nd AIAA Aeroacoustics Conference)*, 2011.

[24] Herr, M., and Dobrzynski, W., "Experimental Investigations in Low-Noise Trailing-Edge Design," *AIAA JOURNAL*, vol. 43, 2005.

[25] Howe, M. S., "AERODYNAMIC NOISE OF A SERRATED TRAILING EDGE," *Journal of Fluids and Structures*, vol. 5, 1991, pp. 33–45.

[26] Howe, M. S., “A review of the theory of trailing edge noise,” *Journal of Sound and Vibration*, vol. 61, Dec. 1978, pp. 437–465.

[27] Leslie, A., Wong, K. C., and Auld, D., “Broadband noise reduction on a mini-UAV Propeller,” *29th AIAA Aeroacoustics Conference*, 2008, pp. 5–7.